Department of Earth Sciences
University College London (UCL)

Hydrogen and Helium at Conditions of Giant Planet Interiors

Adam Martins

Submitted in fulfilment of the requirements
for the degree of Doctor of Philosophy
at University College London

February 24, 2015

Declaration

I, Adam Martins confirm that the work presented in this thesis is my own. Where information has been derived from other sources, I confirm that this has been indicated in the thesis.

Abstract

NVT ensemble simulations have been conducted for pure hydrogen and H-He mixtures at primordial concentrations (0.09 helium number fraction) by using the vdW-DF2 exchange-correlation functional for comparison to PBE results. These results show helium to diminish the first-order behaviour of the phase transition observed in pure hydrogen at 1000 K. Phase transitions are shifted to higher densities and pressures with the inclusion of helium and further by the use of the vdW-DF2 functional. Thermodynamic and transport properties reported of hydrogen give the super-critical extension of the liquid-liquid phase transition known as the Widom and Frenkel lines. Excellent agreement is shown with experimental data for pressure, conductivity and reflectivity along the principal Hugoniot as calculated with vdW-DF2. NPT ensemble simulations are conducted on the solubility of helium in hydrogen having significant implications for the interiors of gas giant planets. VdW-DF2 results show helium to be soluble in hydrogen to much lower temperatures than predicted by PBE due to the favouring of molecular hydrogen which allows for helium to be soluble in hydrogen. This implies that helium falling under gravity and producing latent heat will likely not occur within the interiors of Jupiter and Saturn.

Contents

Chapter 1

Introduction

1.1 Giant Planet Interiors

Understanding high pressure hydrogen has significant importance for astrophysics as it makes up most of the matter in the universe, and is also the main constituent of the interiors of gas giants such as Jupiter. To better understand the interior and exterior properties of such planets, study of the atomic properties and dynamic behaviour of hydrogen and other major elements, in particular helium, is required. Accurately determining the equation of state is important for correctly modelling the structure origin, and evolution of planets [1].

From early theoretical work there have been many questions raised regarding hydrogen. A possible insulator-to-metal transition is expected and, in the solid phase, is yet to be observed [2]. The relationship between the insulator-to-metallic and the molecular-to-atomic transition is an important problem for Jovian interiors and for the understanding of elemental hydrogen.

Observational constraints such as the total mass, radius, rotational rate, and gravitational moments must be combined with the equation of state to determine planetary interior

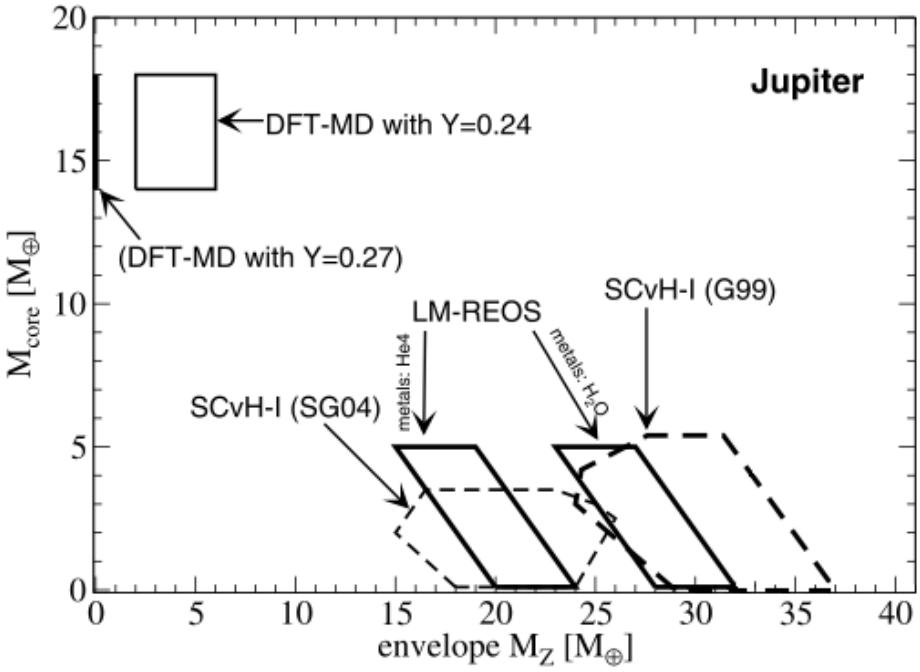

Figure 1.1: Results of various equations of state used for Jupiter yielding a range of possible core sizes. Cores predicted are from using SCvH-i (SG04) and Sesame-p assume Z_1=Z_2 (index 1 refers to the outer envelope and 2 refers to the inner envelope) [6], SCvH-i (G99) for $Z_1 \neq Z_2$ [7], and Sesame-K04 model using $Z_1 < Z_2$ [8] as well as the LM-REOS models (altered in [9]). DFT models for a two layer model [10]. Modified from [11].

structure. Hydrogen and helium are both significant: the estimated protosolar helium mass fraction is $Y \sim 0.27$ [3]. Jupiter has $Y \sim 0.234 \pm 0.005$ [4], and Saturn $Y \sim 0.18 - 0.25$ [5].

Precise knowledge of the equation of state is important, small differences can lead to greatly altered results such as the size and even existence of a heavy element core fig. 1.1. Understanding the existence and mass of a core is critical to understanding how the Jovian planets formed.

Planetary magnetic fields are created by convective motion of a large body of rotating conductive liquid [12]. It is therefore necessary to have knowledge of the mass and electronic transport properties such as diffusion rates and electrical conductivity.

It is well known that as giant planets evolve they contract and cool, releasing more heat

then what they receive from the Sun [12]. From simple thermodynamic arguments the cooling rate, luminosity and temperature, at a given age, can be estimated for Saturn. This shows Saturn to have a higher luminosity for its current age. A proposed explanation of this excess in luminosity can be from the helium separation in the interior. If helium exsolves on cooling, helium sinks towards the core; the gravitational energy released contributes to the known excess in luminosity of Saturn [13–16]. Helium rain has been predicted to slow the cooling of Jovian planets by several hundreds of millions of years [7, 17].

Another important feature affecting the thermal evolution of the planet is core erosion. Depending on the rates of erosion of the rock-metal core with the surrounding H-He envelope substantial amounts of heavy elements have been added to the envelope over time [18].

1.2 Experimental Methods

Dynamic shock compression experiments produce pressure-temperature paths closest to those of planetary interiors fig. 1.2. The principal Hugoniot rapidly becomes too hot on compression, motivating techniques such as ramp compression, second shocks and reverberation to produce pressure-temperature paths more similar to planetary interiors [19–26]. The primary limitations of shock wave experiments is the difficulty in measuring state- and material-specific properties. For example, many experiments measure only the pressure, and not the density or temperature (these are calculated from an assumed EOS) while others measure the shock velocity giving the pressure and density from an EOS. Detecting atomic structure is very challenging which means that liquid-liquid phase transitions or helium exsolution are difficult to detect. The standard method to measure density used in Hugoniot experiments is impedance matching [27] based on the equation of state of a standard (Al or silica). Work by Hicks *et al.* [26] show typical errors in these analyses fig. 1.3. Reflectivity can be measured in laser-driven shock wave experiments [28] using a velocity interferometer system. Other properties that can be measured include the

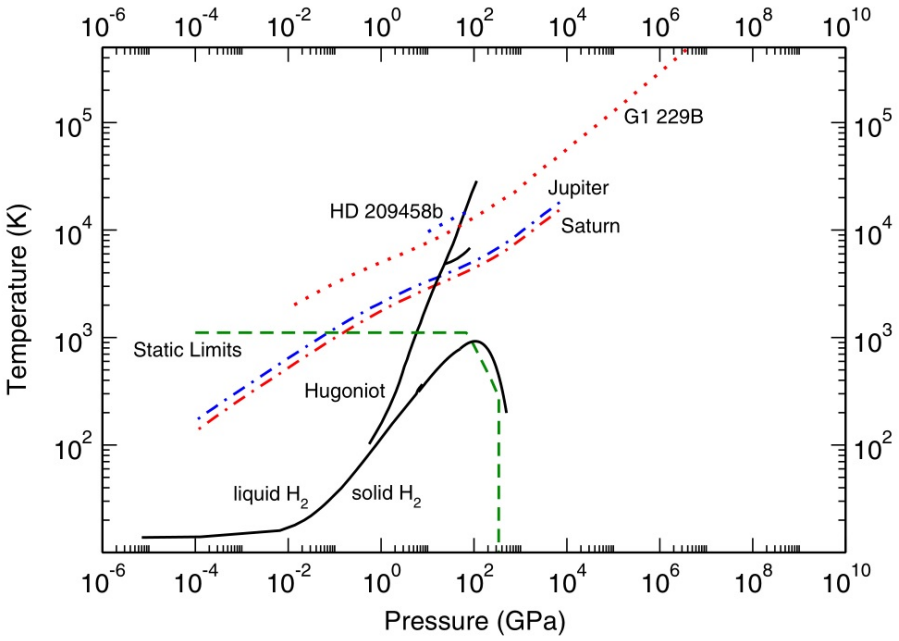

Figure 1.2: Phase diagram of hydrogen. Static experiments limit shown by green bounds [2, 30]. Solid black line shows principal Hugoniot (shock experiments) [25] and double shock experiments are shown branching from it [31]. The melting line of hydrogen shown as a solid black line within the static limit region. Jupiter, Saturn [6] and HD 209458b [32] isentropes are blue, red dash-dotted and blue dotted respectively and the model of brown dwarf (G1 229B) are red dotted [33]. From [34].

electrical conductivity [29] by measuring the voltage across the sample.

These experiments produce a shock wave propagating into the sample material. Techniques are then used to measure the shock wave velocity and the particle velocity behind the shock front. Many methods to produce these shocks exist such as gas gun experiments [31, 35], laser driven compression [26, 36–39], magnetically driven flyers [23, 40, 41] and hemispherically converging explosions [42].

These experiments are capable of achieving higher temperatures and pressures than static compression experiments - up to ∼500 GPa and 50 kK. Early shock wave experiments of hydrogen and deuterium [43, 44] (where a gas-gun compression method was used) achieved up to 20 GPa in the first shock, followed by the reflected shock at 90 GPa. Laser-driven single shock experiments have achieved pressures of up to ∼ 200 GPa [45].

Reverberating shock experiments on hydrogen by Weir *et al.* [19] have shown a rapid change in conductivity at ∼140 GPa. Experimental reverberating shocks [19, 46] compressed hydrogen showing the resistivity decreases by ∼4 orders of magnitude [47] between 93-140 GPa reaching a plateau of 500 $\mu\Omega$ after 140 GPa. They obtain the temperature by fitting to a model at 140 GPa, which gives an approximation of ∼ 3000 K where the system is still found to be largely molecular (only ∼ 5 % dissociated). More recent experiments by high-explosive driven generators [24], found a density increase at the same location as the conductivity increase.

Higher pressure, lower temperature conditions can be reached by performing shock experiments on precompressed samples or with double shock experiments. These experiments open up a wider range and are more applicable to Jovian interiors, as shown in fig. 1.2, with experiments reaching 55 GPa [31, 35, 39, 48]. Conductivity can also be measured in these experiments [49] giving insight into the onset of conductivity in the fluid phase.

Static compression experiments [55, 56] allow for more complete characterisation of the sample but are limited in the pressures and temperatures they can reach. Here measurements are made using e.g. X-ray scattering, and IR and Raman spectroscopy. Improvements on diamond anvil cells use gold liners to prevent reaction of the sample with the gasket used to hold the sample in place. These experiments can reach ∼1500 K [57].

Further experiments using diamond anvil cell pre-compression and laser driven shock on helium [58] show the insulator-to-metallic transition. Helium is shown to become metallic at ∼1900 kg m^{-3} at ∼20 kK with higher temperatures giving rise to an earlier onset of conductivity than expected, but still well within the conditions of Jupiter's interior and past the onset of metallisation of pure hydrogen. The experimental results agree with theoretical predictions [59].

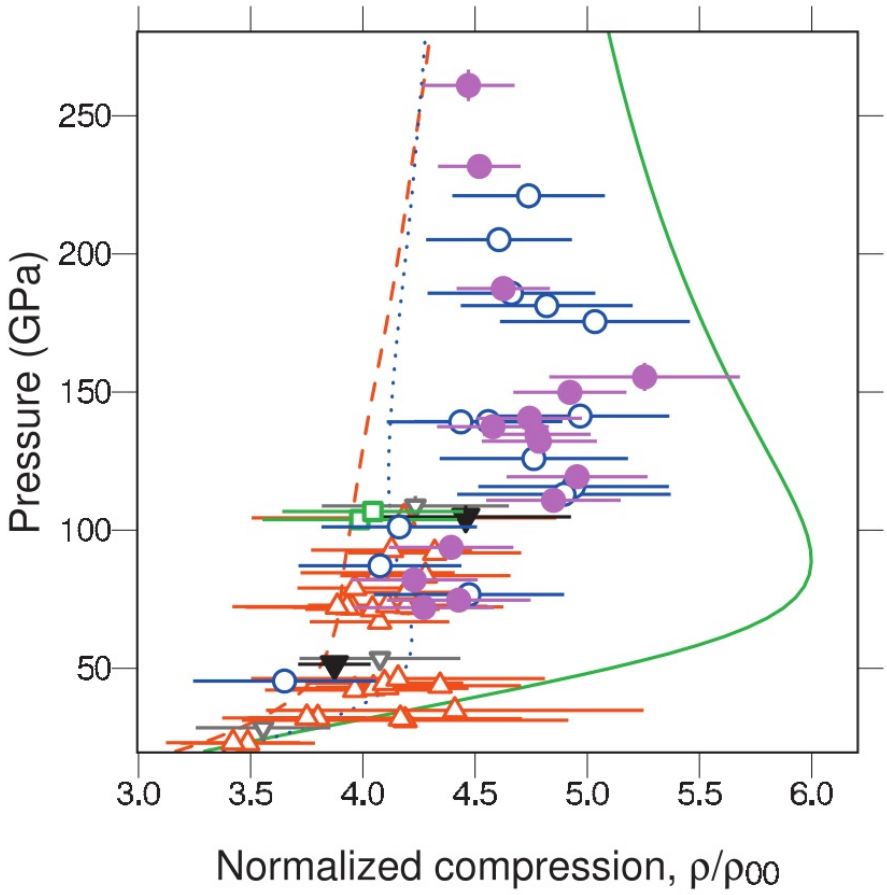

Figure 1.3: Hugoniot measurements, Pressure vs normalised compression ($\rho_{00} = 0.174$ g/cm^3) for single shock measurements of deuterium Hugoniot [26]. Knudson *et al.* [23, 40]are red triangles. Belov *et al.*, Boriskov *et al.* [21, 50] inverted black solid triangles. Boriskov *et al.* [42] inverted black open triangles and Grishechkin *et al.* [51] open green squares. Hicks *et al.* [26] open blue circles. Model curves are from Sesame72 [52] dashed red line, Kerley03 [53] dotted blue line, and Ross equation of state [54] solid green line. With Hicks *et al.* blue open circles [26]. From [26].

1.3 Theoretical Methods

Various semi-empirical thermodynamic and chemical models (aka plasma models) have been applied to the interiors of gas giants, mainly Jupiter and Saturn [9]. These treat nuclei and electrons as classical particles, or treat the electronic structure as that of a perturbed uniform electron gas [15, 60, 61]. The model proposed by Saumon, Chabrier and van Horn [62] (SCVH) has been widely used in modelling applications for gas giant interiors. Though this model reproduces many experimental results (at low temperature and high pressure, and at high temperature and high pressure), there are still large uncertainties particularly in the vicinity of the liquid-liquid phase transition.

Chemical models predicted that hydrogen will become atomic after a first-order phase transition with increasing pressure [48, 63–71]. It is now understood that these chemical models predict a pronounced phase transition as an artificial property of the underlying physical approximations [72]. Therefore, the transition is now smoothed out of the equation of state [73] when using these chemical models in planetary applications.

Due to the success of density functional theory (DFT) in accurately describing atoms and complex materials it is used for many scientific applications, including in geophysics for understanding iron at Earth's core conditions [74] and many others [72, 75, 76]. Progress has been made in using DFT to understand the interior of gaseous planets [11] with results often quite different from earlier semi-classical approximations.

A number of important features of pure hydrogen have been discovered through the use of DFT. DFT based molecular dynamics was used in predicting a negative slope for the melting line in temperature-pressure space brought on by the liquid-liquid phase transition [77]. Further work showed, using solid and liquid phases [78], a maximum of the melting line at 1000 K with a negative slope extrapolating to 0 K and 400 GPa. The Gibbs energy of the liquid and solid phases, from DFT simulations, was also used to analyse the melting line [79]. Results of diamond anvil cell experiments [80] agree with the theoretical

melting line, and are in further agreement with the experimental determinations of [81] and [57]. Additional diamond anvil cell experiments [80] have also shown a negative slope. These results are shown in fig. 1.4 alongside other experimental determinations of Datchi *et al.* [82] and Gregoryanz *et al.* [83] showing the melting line. Below the melting line in fig. 1.4 the solid structures at low temperatures, determined experimentally, are shown. Solid structures are labelled as phases I, II, III and IV.

Likely candidates for the low pressure solid structures are as follows. For phase I the parahydrogen (p-H_2) at low temperature crystallises in a close-packed hcp structure [84]. Phase II suggested from PIMC calculations is Pa3-type ordering on hcp lattice (molecules along the body diagonals) [85]. The phase III structure predicted by [86] consists of molecules packed in ring like structures with rings being made up of three molecules. Finally, phase IV structure is suggested by [87] consisting of alternating atomic graphene-like and molecular layers.

An early DFT molecular dynamics study found a large density fluctuation signalling a first-order phase transition at 1500 K and P = 125 GPa [77]. They also observed a molecular dissociation and at this location the system became metallic as the closure of the gap was seen. These results require a critical temperature between 1500 and 3000 K to agree with the above experimental work. Further DFT work by Bonev *et al.* [78, 88] found a first-order phase transition at 200 GPa and 900 - 1000 K.

A more thorough analysis of the transition region using DFT by sampling the region at a higher resolution [79] was carried out with 432 atoms and reported a first-order phase transition occurring at 1000 K. Coupled Electronic-Ionic Monte Carlo (CEIMC) was used similarly and found a first-order phase transition [89].

A previous study has been carried out on hydrogen and helium mixtures for implications to Jupiter [90], using up to 250 atoms with a proportion of helium atoms equivalent to that of Jovian planet interiors. They report properties such as the radial distribution function of the hydrogen and helium mixtures, and how the pressure changes with temperature for

various helium number fractions. These results show that the inclusion of helium 'washes out' the first-order nature of the liquid-liquid phase transition in liquid hydrogen. They show a method of counting the atomic particles in the simulation [91], compared to the molecular contribution, allowing a more thorough description of the liquid-liquid phase transition.

As well as equation of state studies from first-principles methods, extensive work on the optical properties has come from using the Kubo-Greenwood formula. Studies such as [92–94] used this method to calculate the direct current (DC) conductivity, thermal conductivity and reflectivity in the latter, the results were compared to experiments [95], showing good agreement and a dependence on the functional used in DFT.

One of the main problems with DFT is known as the band gap problem. DFT is known to underestimate the band gap [96, 97] therefore the insulator-to-metallic transition density will likely be underestimated. Improvements on the band gap have been seen by quasiparticle methods [98], using exact exchange methods [99] or many-body GW methods [100].

Extensive tests, performed by Clay *et al.* [101], using new exchange-correlation functions has shown that van der Waals density functionals vdW-DF and vdW-DF2 (non-local functionals) outperforms Perdew, Burke and Ernzerhof (PBE) [102] and in some cases Heyd, Scuseria and Ernzerhof (HSE) [103], predicting improved band gaps, bond lengths and energetics in the liquid phase close to metallisation. The authors consider vdW-DF and vdW-DF2 superior in terms of local energy differences in the potential energy surface. VdW-DF2 improvements can be expected as the exchange term used is tuned to exact exchange [104] and because it includes dispersion forces. This thesis tests vdW-DF2 and as such should provide a more accurate equation of state (relative to PBE and chemical model EOS) for hydrogen and helium and provide new insights into Jovian interiors. A study by Morales *et al.* [95], using the vdW-DF2 functional, has shown the occurrence of the liquid-liquid phase transition at a higher density and pressure than predicted with PBE. They showed liquid hydrogen remaining molecular well into the phase transition

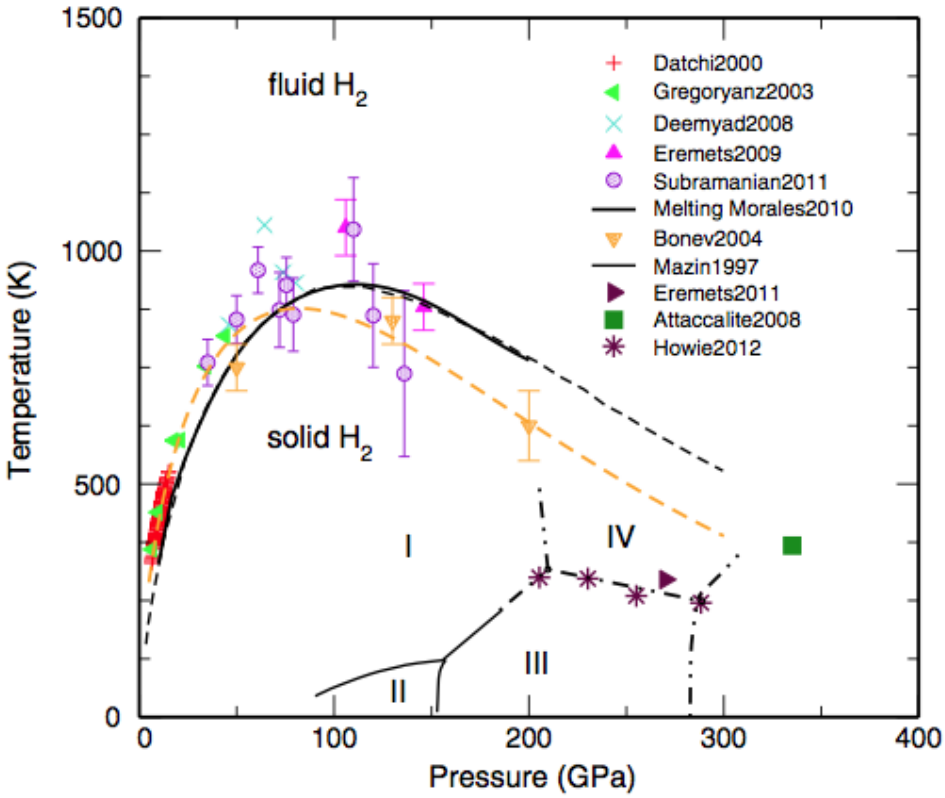

Figure 1.4: Solid to liquid melting line of hydrogen. Various DFT results and experimental data. Experimental data: red crosses [82], left triangles [83], blue crosses [80], up triangles [81] and circles [57]. Theoretical results: BOMD down triangles [78], free-energy calculations solid black line [79]. Dashed black line is a fit to a Kechin equation at low temperature using data from Datchi *et al.* and at high temperature from results of Morales *et al.*. Green square is MD using QMC forces [105]. Experimental solid phases with IM transition from [106] are shown below the melting line. From [34].

reported by DFT-PBE.

A problem in current knowledge on the properties of Joivian interiors is the immiscibility of helium with hydrogen [90]. Initial studies used perturbative treatments of the H-He mixture with assumed interactions between chemical species [107–111]. These studies generally found the critical temperature of immiscibility too low to affect the Jovian interior [112]. First principles was first used within the Local Density Approximation (LDA) [113]. They calculated the enthalpy of mixing on static structures and as such neglected the relaxation of the structure as helium is added to the system as well as the

disorder of the liquid state. A DFT molecular dynamics study [114] estimated the free energy of mixing, neglecting thermal effects of the enthalpy of mixing. They find a mixing temperature too low to allow de-mixing within Jupiter and Saturn.

Recent simulations calculating the Gibbs energy via thermodynamic integration showed that large portions of Saturn could have phase separations between hydrogen and helium with Jupiter's interior being fully mixed throughout. Morales *et al.* [115] show that increasing the helium fraction alters the preferred pairing of hydrogen in favour of being molecular. This is because the inert helium inhibits the delocalisation of the hydrogenic electrons, enhancing the formation of molecular hydrogen.

Solubility of other noble gases in helium have been studied within Jupiter and Saturn by Wilson *et al.* [116] providing a possible explanation for the observed neon depletion and the lack of argon depletion in Jupiter, provided that helium rainout occurs in the interior.

Chapter 2

Density Functional Theory

2.1 Introduction

With the founding work on Density Functional Theory (DFT) in the early 60s [117, 118], the properties of materials could, for the first time, be relatively easily calculated. With growing publications DFT has become an important theory in understanding materials from simple molecules [119, 120] to deep Earth processes [74, 121].

DFT is an electronic structure theory where the electronic ground state density $n_0(r)$ is shown to be of great importance to the system being studied and it is from this density that all other properties depend, hence the so called density functional theory. DFT can be used to calculate a number of chemical properties such as atomic structures, atomization and ionization energies, electric and magnetic properties and many more.

The initial findings by Hohenberg and Kohn [117] were fundamental but did not show how one could evaluate the functional. The next step in DFT came with Kohn and Sham [118]. In the Kohn-Sham formulation the full many body problem is replaced by a set of non interacting free electrons with the additional exchange-correlation functional which contains the many-body complexities. This approach allows for the approximation

of a ground state functional for the many electron system. Within these methods an exchange-correlation functional is introduced which contains the interacting particle terms.

After the initial interest in the 60s it became later clear that even simple approximations for the exchange-correlation Local Density Approximation (LDA) can give reasonably good results that combined with techniques to accelerate the calculations saw a rapid increase of its usage from the 80s to the 90s. Many subject fields use DFT principles for solutions to various systems across physics [122, 123], chemistry [124, 125] and biology [126, 127].

From the literature it is clear that DFT is required for an accurate analysis of hydrogen and helium simulations providing much more reliable predictions than previous classical approaches. With experimental data DFT can be assessed and can be taken beyond the regions attainable by experiment. DFT being a essentially exact quantum mechanical method can also be used to check the validity of past theoretical calculations and evaluate the precision of such calculations.

2.2 Thomas-Fermi theory

An important initial step was made toward DFT by the Sommerfeld theory of an ideal gas of fermions [128, 129]. Here we have a cubic box of particles, volume L^3, containing a uniform non-interacting electron-gas also known as jellium. The electron density is $n = N/L^3$ where N is the number of electrons. These electrons are within a uniform potential V_0. This is a first step in DFT as we now require the ground state energy of the system. Here we require the solution to the time-independent Schrödinger equation, eq. (2.1).

$$\left[-\frac{\hbar^2}{2m}\nabla^2 + V_0\right]\psi(r) = E\psi(r) \tag{2.1}$$

Using periodic boundary conditions to account for a finite cubic cell (simulation "box"),

the solution to eq. (2.1) is the set of plane waves: $\psi(x) \propto e^{ik\cdot x}$ with wavevector $k = \frac{2\pi}{L}n$. We then can relate the energy to the wavevector through applying the de Broglie relation, $p = \hbar k$, giving $E = \frac{p^2}{2m}$ for the energy of each state of the electrons. Note that throughout this chapter spin is considered with the density with $n(r) = n(r,\uparrow) + n(r,\downarrow)$, where the first term is the spin up density and the second term is spin down density.

The Schrödinger equation of a many-body system contains $3N$ degrees of freedom for N electrons and is too complex for practical use. Thomas and Fermi separately developed a simpler method [130, 131] which brings forward the notion that the ground state density determines all parameters. The nonrelativistic Hamiltonian for electrons and ions are used as in eq. (2.2) to obtain the energy functional $E_{TF}[n]$ for the electrons in an external potential $V_{ext}(r)$.

$$
\begin{aligned}
\hat{H} &= \hat{T}_n + \hat{H}_{el} = \hat{T} + \hat{V}, \\
\hat{H}_{el} &= \hat{T}_e + \hat{V}_{n-n} + \hat{V}_{int} + \hat{V}_{ext}, & \hat{T} &= \hat{T}_n + \hat{T}_e, \\
\hat{T}_n &= \sum_{I=1}^{N_n} -\lambda_I \hat{\bigtriangledown}_I^2, & \hat{T}_e &= -\lambda_e \sum_{i=1}^{N_e} \hat{\bigtriangledown}_i^2, \\
\hat{V} &= \hat{V}_{n-n} + \hat{V}_{int} + \hat{V}_{ext}, & \hat{V}_{n-n} &= \sum_{I<J} \frac{z_I z_J}{\left|\vec{R}_I - \vec{R}_J\right|}, \\
\hat{V}_{int} &= \sum_{i<j} \frac{1}{|\vec{r}_i - \vec{r}_j|}, & \hat{V}_{ext} &= -\sum_{i,I} \frac{z_I}{\left|\vec{r}_i - \vec{R}_I\right|}
\end{aligned}
\tag{2.2}
$$

In eq. (2.2) symbols H and H_{el} are the total Hamiltonian and the electron Hamiltonian, T denotes the kinetic energy, V the potential energy. We also have the number of ions N_n and electrons N_e. Also $\lambda_e = 1/2, \lambda_I = 1/(2M_I)$ and M_I and z_I are the mass and charge of the nucleus I (in units of the electron mass m_e and charge e). Subscripts 'ext' and 'int' refer to the electron-nucleus and the electron-electron interactions respectively and position vectors $\vec{r}_i$ for electrons and $\vec{R}_I$ for ions.

Due to Thomas and Fermi neglecting exchange and correlation of the electrons, the extension by Dirac [132] was made including the local approximation of the exchange giving,

$$E_{TF}[n] = A\int d^3r\; n(r)^{5/3} + \int d^3r\; \hat{V}_{ext}\; n(r) + B\int d^3r\; n(r)^{4/3} + \frac{1}{2}\int d^3r d^3R \frac{n(r)n(R)}{|r-R|}, \tag{2.3}$$

where $A = \frac{3}{10}(3\pi^2)^{2/3}$ and $B = -\frac{3}{4}(\frac{3}{\pi})^{1/3}$. The terms in eq. (2.3) are as follows, first term: local approximation of the kinetic energy, second term: interaction of potential with the electrons, third term: local exchange and the last term: classical electrostatic Hartree energy.

The ground state density and energy in a system containing N_e electrons are obtained by a minimization of the Thomas-Fermi energy functional $E_{TF}[n]$ for all possible $n(r)$ where $\int d^3r n(r) = N$. Even though the Thomas-Fermi approach has been applied to the elements [133] the approximations are too crude and do not consider some necessary physics contributing to many body systems. We thus need a more exact many-body theory. For a more thorough account of the Thomas-Fermi theory the reader is referred to [134].

2.3 Hohenberg-Kohn Theorems

Hohenberg and Kohn proved in 1964 [117] that the many body system problem can be reformulated in terms of a functional which is dependent on the ground state density. We start with the Hamiltonian, $\hat{H}$ of a system of interacting electrons in an external potential, $V_{ext}(r_i)$ produced by the nuclei,

$$\hat{H} = -\frac{\hbar^2}{2m_e}\sum_i \nabla_i^2 + \sum_i V_{ext}(r_i) + \frac{1}{2}\sum_{i\neq j}\frac{e^2}{|r_i - r_j|}$$
$$\hat{H} = \hat{T}_e + \hat{V}_{ext} + \hat{V}_{int} \tag{2.4}$$

Hohenberg and Kohn formulated the basic results which set the start of the DFT foundation, where the theorems are as follows:

- Theorem 1: The external potential $V_{ext}(r)$, encompassing a system of interacting particles, is uniquely determined by the ground state particle density $n_0(r)$ (to within an additive constant).

  Corollary 1: Thus the ground state density uniquely determines the Hamiltonian operator eq. (2.4). From this we also have that the many-body wavefunctions Ψ for all states are determined and from this all material properties can be computed.

- Theorem 2: A universally valid functional of the energy $E[n]$ in terms of the density $n(r)$ is defined, for any external potential $V_{ext}(r)$. For any $V_{ext}(r)$, the ground state energy of the system is the global minimum value of this energy functional. The density that minimizes this functional is the exact ground state density $n_0(r)$.

  Corollary 2: The functional $E[n]$ is sufficient to determine the exact ground state energy and density.

2.3.1 Proof of Theorem 1

This proof requires the use of a possible system with two different external potentials, $V_{ext}(r)$ and $V'_{ext}(r)$ leading to the same ground state $n(r)$. These potentials have different Hamiltonians $\hat{H}$ and $\hat{H}'$, having different ground state wavefunctions Ψ and Ψ' which in this fictional system have the same ground state density $n_0(r)$. We therefore have our two Hamiltonians, $\hat{H} = \hat{T}_e + \hat{V}_{int} + \hat{V}_{ext}$ and $\hat{H}' = \hat{T}_e + \hat{V}_{int} + \hat{V}'_{ext}$. Since Ψ' is not the ground

state of $\hat{H}$ it follows that:

$$E = \left\langle \Psi \left| \hat{H} \right| \Psi \right\rangle < \left\langle \Psi' \left| \hat{H} \right| \Psi' \right\rangle \tag{2.5}$$

Considering each term separately from eq. (2.5) using the relations from eq. (2.4) as $\hat{T}_e$ and $\hat{V}_{int}$ are the same for both Hamiltonians, we can rewrite the third term as:

$$\begin{aligned} \left\langle \Psi' \left| \hat{H} \right| \Psi' \right\rangle &= \left\langle \Psi' \left| \hat{H}' \right| \Psi' \right\rangle + \left\langle \Psi' \left| \hat{H} - \hat{H}' \right| \Psi' \right\rangle \\ &= E' + \left\langle \Psi' \left| \hat{V}'_{ext}(r) - \hat{V}_{ext}(r) \right| \Psi' \right\rangle \\ &= E' + \int d^3r [\hat{V}'_{ext}(r) - \hat{V}_{ext}(r)] n_0(r) \end{aligned} \tag{2.6}$$

giving from eq. (2.5):

$$E < E' + \int d^3r [\hat{V}'_{ext}(r) - \hat{V}_{ext}(r)] n_0(r) \tag{2.7}$$

and equally for the second term we get:

$$E' < E + \int d^3r [\hat{V}_{ext}(r) - \hat{V}'_{ext}(r)] n_0(r) \tag{2.8}$$

and adding eq. (2.7) and eq. (2.8) together we get the inequality:

$$E + E' < E + E' \tag{2.9}$$

Clearly showing we can't have two external potentials giving the same ground state density $n_0(r)$, therefore $n_0(r)$ must uniquely determine $V_{ext}(r)$.

2.3.2 Proof of Theorem 2

As each property is determined from the density alone then they are all functionals of the density $n(r)$ giving the Hohenberg-Kohn (HK) energy functional,

$$E_{HK}[n] = T[n] + E_{int}[n] + \int d^3r V_{ext}(r)n(r) + E_{nn} \tag{2.10}$$

where E_{nn} is the internal interaction energy of the nuclei. Here we define $F_{HK}[n] = T[n] + E_{int}[n]$ which contains details of the interacting electron system alone.

Consider now a system with ground state density $n_0(r)$ corresponding to an external potential $V_{ext}(r)$ and further, we have a second density, $n'(r)$ corresponding to a wavefunction of Ψ' and a wavefunction of Ψ for $n_0(r)$.

We know the Hohenberg-Kohn functional is equal to the expectation value of the Hamiltonian at the ground state, giving:

$$E = E_{HK}[n_0(r)] = \left\langle \Psi \left| \hat{H} \right| \Psi \right\rangle \tag{2.11}$$

and we know that E' must be greater than E, giving:

$$E = \left\langle \Psi \left| \hat{H} \right| \Psi \right\rangle < \left\langle \Psi' \left| \hat{H} \right| \Psi' \right\rangle = E' \tag{2.12}$$

Thus, it is shown that the HK functional at the ground state density $n_0(r)$ is lower than any other energy state with an alternate density $n(r)$. In order to find the exact ground state density and energy one has to minimise the energy functional with respect to variations in the density functional $n(r)$. To do this the functional $F_{HK}[n]$ must be known.

Note this only determines the ground state properties. The excited states are accounted for by Mermin's [135] work on finite temperature extensions to DFT. Here it is shown

that thermal equilibrium properties can be determined by the free-energy functional of the density. Mermin showed that for each Hohenberg and Kohn result for the ground state there is a corresponding theorem for a system in thermal equilibrium with a heat bath. For further reading on HK DFT methods the reader is referred to [134, 136, 137].

2.4 Kohn-Sham Theory

After the initial formulation by HK, Kohn and Sham proposed their *ansatz* which is to replace the interacting many-body system of Hohenberg-Kohn with an auxiliary independent-particle system. This auxiliary system is used as it can be solved more easily with an assumption that the ground state density of the interacting system is equal to the ground state density of the new non-interacting system. Here we now get independent particle equations for the non-interacting system with all the many-body terms held inside the exchange-correlation functional of the density. The solutions to these equations give the ground state density and energy of the many-body system but accuracy is determined by one's approximations in determining the exchange-correlation functional.

The Kohn-Sham theorem is developed on two assumptions:

1. The exact ground state density of the interacting system is represented by the ground state density of the non-interacting system, *"non-interacting-V-representability"*.

2. The Hamiltonian of the non-interacting system is chosen to have a kinetic operator and an effective local potential $V^{\sigma}_{eff}(r)$ acting on an electron of spin σ at point r.

Then we can write, for a system of N^{σ} particles, the energy functional in terms of the single-body orbitals of the non-interacting system, eq. (2.13), where the ground state has one electron in each N orbitals $\psi^{\sigma}_{i}(r)$ with the lowest eigenvalues ϵ^{σ}_{i} of the Hamiltonian.

$$
\begin{aligned}
T_s[n] &= -\frac{1}{2}\sum_{\sigma}\sum_{i=1}^{N}\int d^3r\,|\bigtriangledown\psi_i^{\sigma}(r)|^2\,, \\
E_H[n] &= \frac{1}{2}\int d^3r d^3r'\frac{n(r)n(r')}{|r-r'|}, \\
n(r) &= \sum_{\sigma} n(r,\sigma) = \sum_{\sigma}\sum_{i=1}^{N}|\psi_i^{\sigma}(r)|^2\,, \\
E_{KS}[n] &= T_s[n] + \int d^3r n(r)V_{ext}(r) + E_H[n] + E_{nn} + E_{xc}[n]
\end{aligned} \tag{2.13}
$$

$E_H[n]$ is the classical Coulomb interaction energy of the electron density $n(r)$ interacting with itself (or the Hartree energy) and $T_s[n]$ is the independent particle kinetic energy. Seen in eq. (2.13) is that the density of the non-interacting system, $n(r,\sigma)$ is the sum of squares of the orbitals for each spin. We end up with the Kohn-Sham (KS) approach giving the energy functional $E_{KS}[n]$, eq. (2.13). $V_{ext}(r)$ is the external potential due to the nuclei and any other external field and is independent of spin and finally E_{nn} is the interaction between nuclei. Note that all many-body effects of exchange and correlation are within the E_{xc} term.

We can compare energy functionals from Kohn-Sham and Hohenberg-Kohn to give a $E_{xc}[n]$ term, giving:

$$
\begin{aligned}
E_{xc}[n] &= F_{HK}[n] - (T_s[n] + E_H[n]) \\
E_{xc}[n] &= T[n] + E_{int}[n] - (T_s[n] + E_H[n])
\end{aligned} \tag{2.14}
$$

From eq. (2.14) we can see that $E_{xc}[n]$ must be a functional since the terms on the right hand side of the equation are functionals. We also see that $E_{xc}[n]$ is just the difference of the kinetic and internal interaction energies between the true interacting many-body system and the non-interacting particle system with electron-electron interactions replaced

by the Hartree energy.

If we place the terms $E_H[n]$, E_{nn} and $E_{xc}[n]$ from eq. (2.13), into a new term $G[n]$, we get: $E_{KS}[n] = T_s[n] + \int d^3r n(r,\sigma)V_{ext}(r) + G[n]$ and applying the variational principle we get:

$$0 = \delta E = \int d^3r [V_{ext}(r) + \frac{\delta T_s}{\delta n(r,\sigma)} + \frac{\delta G}{\delta n(r,\sigma)}]\delta n(r,\sigma) \tag{2.15}$$

As we have an unchanging particle number we set $\int d^3r \delta n(r,\sigma) = 0$, and we now write:

$$V_{ext}(r) + \frac{\delta T_s}{\delta n(r,\sigma)} + \frac{\delta G}{\delta n(r,\sigma)} = \mu \tag{2.16}$$

where μ is the chemical potential (or a Lagrange undetermined multiplier).

Using the Kohn-Sham theory we define an effective potential $V^{\sigma}_{eff}(r)$ as,

$$V^{\sigma}_{eff}(r) = V_{ext}(r) + \frac{\delta G}{\delta n(r,\sigma)} \tag{2.17}$$

we can now use for an interacting system the same equation as for the non-interacting system plus this effective potential contribution, giving:

$$\frac{\delta T_s}{\delta n(r,\sigma)} + V^{\sigma}_{eff}(r) = \mu \tag{2.18}$$

This equation now allows us to rewrite our Schrödinger equation giving the Kohn-Sham equation and it's corresponding Kohn-Sham orbitals $\Psi(r)$,

$$-\frac{\hbar^2}{2m}\nabla^2\Psi^{\sigma}_i(r) + V^{\sigma}_{eff}(r)\Psi^{\sigma}_i(r) = \varepsilon^{\sigma}_i(r)\Psi^{\sigma}_j(r) \tag{2.19}$$

where the effective Hamiltonian H_{KS} is, (with eigenvalues ϵ_i^σ);

$$H_{KS}^\sigma(r) = -\frac{\hbar^2}{2m}\nabla^2 + V_{KS}^\sigma(r) \tag{2.20}$$

and the Kohn-Sham potential associated with any interacting electron system is V_{KS};

$$V_{KS}^\sigma(r) \equiv V_{eff}^\sigma(r) \mid_{min} = V_{ext}(r) + V_{Hartree}(r) + V_{xc}^\sigma(r) \tag{2.21}$$

and the density is given by

$$n(r) = \sum_\sigma \sum_{i=1}^{N} |\psi_i^\sigma(r)|^2 \tag{2.22}$$

2.4.1 Solving the Kohn-Sham Equations

We now look at methods used to solve the KS equations and minimisations implemented within the calculations to obtain self-consistency.

Equation (2.19) is now used in an iterative manner to solve for the system in question. With an appropriate approximation to $G[n]$ we,

1. Make the initial guess at the density $n(r)$.
2. Calculate $V_{eff}(r)$ with eq. (2.17).
3. Solve the KS equation and the KS orbitals through eq. (2.19).
4. From this we can obtain a new electron density $n'(r)$ using eq. (2.22).
5. Now with the new density we go back and repeat until convergence is found. The approach by VASP in obtaining self-consistency is further explained below.

At step 4, a new electron density $n'(r)$ is obtained through a linear mixing approach to determine a more appropriate value rather than simply the outcome given from eq. (2.22).

Examples of methods for calculating $n'(r)$ include a linear mixing iterative matrix diagonalisation scheme (RMM-DIIS [138] and/or blocked Davidson [139–143]) algorithm giving the new input density (n_{i+1}^{in}) which includes the previous iteration density (n_i^{in}) and the density obtained in step 4 (n_i^{out}) in a linear mixing combination (α) giving eq. (2.23),

$$n_{i+1}^{in} = n_i^{in} + \alpha(n_i^{out} - n_i^{in}). \tag{2.23}$$

Once we have the wavefunctions (obtained from the density through eq. (2.22)) the energy is calculated, $E = \langle\Psi|H|\Psi\rangle$, this is now minimized until a user defined accuracy is reached.

2.4.2 Born-Oppenheimer Molecular Dynamics

In 1927 Born and Oppenheimer [144] recognised the fact that nuclei are much slower than electrons and electrons can be assumed to instantaneously and adiabatically relax to the nuclei positions due to their differences in mass. This approximation is used when we conduct Born-Oppenheimer molecular dynamics (BOMD) where we evaluate the forces acting on the nuclei at every MD time step [145, 146]. The forces on the ions are obtained from the Hellman-Feynman theorem by eq. (2.24) [147, 148].

$$F_n = -\frac{\partial E}{\partial R_n} = -\int dr n(r)\frac{\partial V_{ext}(r)}{\partial R_n} - \frac{\partial E_{nn}}{\partial R_n} \tag{2.24}$$

Which comes from the HK expression for the total energy eq. (2.10) since the terms of the nuclei interaction E_{nn} and the external potential $V_{ext}(r)$ are the only terms which depend on the position R of the nuclei, and eq. (2.24) is the 'electrostatic theorem' for the forces [148].

The validity of using this theorem at this point in the simulation relies on the DFT calculation being well converged so that the KS energy functional is at its variational

minimum.

2.5 Exchange and Correlation

By separating out the independent-particle kinetic energy and the long-ranged Hartree terms, the exchange-correlation functional, E_{xc} can be approximated by a local or semi-local functional of the density. In this section I will review some important aspects of the exchange-correlation energy highlighting the two versions used within this thesis.

We need to approximate the exchange-correlation functional of a many-body interacting electron system as a local or nearly local functional of the density. Kohn and Sham proposed alongside their work on the non-interacting system *ansatz* that solids can be considered approximately equal to the homogeneous electron gas limit. The exchange and correlation effects are local in nature in this limit, giving the Local Spin Density Approximation (LSDA). Here E_{xc} is an integral over all space with the exchange-correlation energy density at each point assumed to be equal to the homogeneous electron gas with that density, meaning we can write the energy as $E_{xc}[n] = \int d^3r n(r)\epsilon_{xc}^{jellium}(n, r)$, where the functional $\epsilon_{xc}(n, r)$ is the energy per electron at a point r depending only on the density $n(r, \sigma)$ in the local area of point r and can be expressed in separate terms for exchange ϵ_x and correlation ϵ_c.

The homogeneous electron gas exchange-correlation as a function of density is now needed. The exchange energy of the homogeneous gas is obtained from a simple analytical expression from Hartree-Fock methods [149], and the correlation energy has been calculated from highly accurate Monte Carlo methods, [150].

2.5.1 Generalised Gradient Approximation

To move forward from a fully local approximation the semilocal Generalised Gradient Approximation (GGA) is introduced, where we define a factor F_{xc} to account for a gradient of the density $\mid \nabla n(r) \mid$. Giving,

$$E_{GGA}[n] = \int d^3r \epsilon_{xc}^{jellium}(n,r) F_{xc}(n(r), \mid \nabla n(r) \mid) \tag{2.25}$$

Different versions of GGA are set up to modify the behaviour of the function F_x at large gradients (as at small gradients most functions are equal, this is also true for the correlation energy term, F_c) in an attempt to reproduce desired properties of a system. The most widely used version, and used within some results of this thesis, is the method by Perdew, Burke and Ernzerhof (PBE) [102]. Generally most GGA's have the condition $F_x \geq 1$, where by comparison LDA has the equivalent value of $F_x^{LDA} = 1$, (Note, PBE-GGA uses a value of $F_x \sim const$). This leads to a lower GGA exchange energy relative to LDA. As there are likely to be more varying density regions in atoms than in condensed matter, giving a lowered exchange energy in atoms than in solids or molecules, resulting in a reduction of binding energy (correcting LDA's overbinding) generally improving experimental agreement for GGA's.

Correlation terms, F_c are much smaller compared to the exchange energy and vanishes at large gradients as large gradients correspond to strong confining potentials that increase level spacings and reduce interaction effects relative to independent-electron terms.

2.5.2 Van der Waals Density Functionals

As nonlocal, long-ranged interactions such as van der Waals (vdW) forces are also important for many particle systems, including hydrogen [151, 152] we turn our attention to the van der Waals - Density Functionals, (vdW-DF and more importantly vdW-DF2

which is used in this thesis). These functionals are derived in detail in the papers of Dion *et al.* [153] and Lee *et al.* [104] showing the correct $1/r^6$ asymptotic limit between molecular dimers. Here I will write about the vdW-DF2 functional as this is used rather than vdW-DF due to better agreement with experimental results such as the adsorption energy and optimal separation [154–156]. Initially the correlation energy is separated into two parts, $E_c^{new}[n] = E_c^0[n] + E_c^{nl}[n]$ where both terms are to be treated with different approximations. First, the local term E_c^0 for both vdW-DF and vdW-DF2 is treated in LDA due to all non-local effects occurring within E_c^{nl}.

Second, a new non-local correlation energy, E_c^{nl}, is defined,

$$E_c^{nl} = \int d^3r \int d^3r' n(r)\phi(r,r')n(r') \tag{2.26}$$

where $\phi(r,r')$ is some functional depending on $r - r'$ and $f(r)$ which is a function of $n(r)$ and its gradient. In the methods of vdW-DF2 the $f(r)$ functional is derived with the large-N asymptote [157] and the exchange energy asymptote series for neutral atoms.

We therefore have a new exchange correlation E_{xc}, giving, $E_{xc} = E_x^{GGA} + E_c^{new} = E_x^{GGA} + E_c^{LDA} + E_c^{nl}$. vdW-DF chooses a GGA exchange from the revPBE [158, 159] functional and vdW-DF2 chooses the PW86R [160, 161] functional due to being a more accurate semilocal exchange functional [160, 161].

Other methods know as Hybrid-functionals are also in use where a Hartree-Fock term is used to describe some exchange, E_x^{HF}, and the rest describing exchange and correlation is from either LDA or GGA. This gives the expression $E_{xc} = \frac{1}{2}(E_x^{HF} + E_{xc})$. Different versions of Hybrid functionals can take on slightly different appearances but generally follow this formulation.

It is briefly noted here that the exchange-correlation potential, $V_{xc}(r)$ is the functional derivative of E_{xc}, which is written as,

$$V_{xc}(r) = \epsilon_{xc}(n, r) + n(r)\frac{\delta\epsilon_{xc}(n, r)}{\delta n(r)} \tag{2.27}$$

For methods on efficiently obtaining the exchange-correlation potential from eq. (2.27) the reader is referred to the appropriate chapter in [134].

2.6 Plane Wave to Projector Augmented Wave method

2.6.1 Plane Wave Basis Function

Now we need to choose the representation of the orbitals, the basis sets. Plane waves and a linear combination of localized functionals are usually used. We represent the wave-function $\psi_n(r)$ from the Kohn-Sham equation using the basis set $e^{ik\cdot r}$ and obeying the Bloch's theorem [162] due to periodicity of the simulations, allowing,

$$\psi_n(r) = u(r)e^{ik\cdot r} \tag{2.28}$$

where $u(r)$ is represented by Fourier series,

$$u(r) = \sum_G c_G e^{iG\cdot r} \tag{2.29}$$

Here the G term belong to reciprocal space of the simulation cell (periodic cells from a Bravais lattice) and the sum extends over all vectors such that $|G|^2/2 < E_{cut}$, where E_{cut} is the cut-off parameter on the accuracy of the expansion. The value of E_{cut} depends on the pseudopotential and the nature of the electronic states. The value of E_{cut} is chosen such that the total energy is converged.

2.6.2 Pseudopotentials

These plane waves require a dense grid to represent localized or highly oscillatory orbitals presenting a problem for core states that are localised in the core regions. We therefore require 'pseudopotentials' to replace the true potential where the Kohn-Sham eigenvalues remain unaffected. Pseudopotentials are renormalised electron nuclei potentials for valence states that include both coulomb attraction of nuclei and screening effects from the presence of core electrons. Pseudopotentials greatly reduce computational demand and have the effect of removing core states from calculations to obtain smooth valence states in core regions, made possible since the tightly bound core electrons don't contribute greatly to the intermolecular bonding [163].

2.6.3 Projector Augmented Wave method, PAW

The Projector Augmented Wave method (PAW) [164–166] allows the calculation of all-electron observables from the pseudo wavefunction $|\tilde{\Psi}\rangle$ through a linear transformation operator $\mathcal{T}$ through eq. (2.31),

$$|\Psi_n\rangle = \hat{\mathcal{T}}\,|\tilde{\Psi}_n\rangle \tag{2.30}$$

where

$$\hat{\mathcal{T}} = 1 + \sum_a \hat{\mathcal{T}}^a \tag{2.31}$$

where $\mathcal{T}^a$ is non-zero within the radial grid surrounding each atom Ω_a enclosing atom a, where $\hat{\mathcal{T}}^a = \hat{\mathcal{T}}^a(r - R^a) = 0$ for $|r - R^a| > r_c^a$ where r_c^a is the cut-off radii and is chosen with no overlap of augmentation spheres. We next expand the pseudo wavefunction into pseudo partial waves $\tilde{\phi}_i$,

$$|\tilde{\Psi}_n\rangle = \sum_i |\tilde{\phi}_i\rangle\, c_i \text{ within } \Omega_a \tag{2.32}$$

The coefficients c_i can be written in relation to 'projector functions' $|p_i^a\rangle$, as $c_i = \langle p_i^a|\tilde{\Psi}\rangle$ where we have,

$$\langle p_i^a|\tilde{\phi}_j\rangle = \delta_{ij}, \quad \delta_{ij} = \begin{cases} 0 & \text{if } i \neq j \\ 1 & \text{if } i = j \end{cases} \tag{2.33}$$

where δ_{ij} is the Kronecker delta.

At this point the Kohn-Sham Schrödinger equation for an isolated system gives the all-electron partial waves $|\phi_i\rangle = \mathcal{T}\,|\tilde{\phi}_i\rangle$. Inserting c_i into eq. (2.32) gives,

$$\hat{\mathcal{T}} = \sum_a \sum_i \left(|\phi_i^a\rangle - |\tilde{\phi}_i^a\rangle\right) \langle \tilde{p_i^a}| \tag{2.34}$$

From eq. (2.34) we can get the Kohn-Sham wavefunctions, $\Psi_n(r) = \langle r|\Psi_n\rangle$ giving,

$$\Psi_n(r) = \tilde{\Psi}_n(r) + \sum_a \sum_i (\phi_i^a(r) - \tilde{\phi}_i^a(r)) \langle \tilde{p}_i^a|\tilde{\psi}_n\rangle \tag{2.35}$$

We therefore have three properties defining the PAW transformation, they are:

1. Partial waves ϕ_i^a from solutions of the Schrödinger equation for the isolated atom.
2. Pseudo partial waves $\tilde{\phi}_i^a$, smoothed within the augmentation sphere and are the true partial waves outside.
3. Pseudo projector functions $\tilde{p}_i^a$ for each partial wave, obeying eq. (2.33).

PAW assumes reliability of the Frozen-core approximation implying the core states are localised in the augmentation spheres and that the core states are not affected by their chemical environment.

Even though hydrogen and helium, both of which are studied in this thesis, have no core electrons it is still preferable to use pseudopotentials because the alternative in us-

ing the Coulomb potential $1/r$ requires a large E_{cut} which in turn greatly increases the computational demands. The reader is referred to [134] for a more in-depth account of pseudopotentials and PAW methods.

2.7 Molecular dynamics simulations

The motion of the ions are calculated using classical mechanics forces where the force on an ion, $\vec{F_A}$, is

$$\vec{F_A} = M_A\vec{a} = -\frac{dE}{d\vec{R_A}} = M_A\frac{d^2\vec{R_A}}{dt^2} \tag{2.36}$$

giving the equation of motion of the ions, where the ion mass is M_A, $\vec{a}$ is the (acceleration) second derivative of the position with respect to time $d^2\vec{R_A}/dt^2$. To propagate the atoms and obtain the trajectories the equation of motion is integrated with the Verlet algorithm [167] and the forces are calculated from the Hellmann-Feynman theorem as shown above in section 2.4.2 and is calculated after the electronic self-consistency is found. Note that in variable cell shape dynamics there is also another force due to the derivative of the basis set with respect to $\vec{R_A}$ [168]. The pulay stress on the unit cell can be non-zero if the total energy is not well converged.

Most of the MD simulations in this thesis are done using the (NVT) canonical ensemble meaning the number of atoms (N) the volume (V) and the temperature (T) are kept constant. The system is assumed isolated and in contact with a heat bath which is controlled with a Nosé-Hoover thermostat [169, 170], where the work of Nosé and Hoover shows the algorithms used to keep the kinetic-energy constant within MD simulations.

For calculating the Gibbs energy of mixing of H-He mixtures I use the Isothermal-isobaric ensemble (NPT), where I now keep atoms (N) pressure (P) and temperature (T) constant where I use the Souza-Martins barostat (keeping pressure constant) as implemented

by Hernandez [171, 172] with a fictitious mass of 1×10^{-4} amu where a Nosé-Poincaré thermostat [173] is used in keeping temperature constant.

2.8 K-Points

To deal with size effects and the periodic nature of the problem we integrate over the first Brillouin-zone. One sufficiently dense mesh is proposed by Monkhorst and Pack [174], and is uniformly distributed over the Brillouin zone (obtaining a measure of the periodic nature of the system), with sampled k-points parallel to reciprocal lattice vectors. Therefore the Brillouin zone is divided into equally sized small cells with their corners being the k-points of the sampling mesh. I use in all MD simulations the Γ point as all tests show this to be adequate for convergence of thermodynamic properties. For calculations involving the Kubo-Greenwood formula, eq. (3.13) as described below in section 3.2.2, a $(2 \times 2 \times 2)$ k-points sampling is used for convergence of the electrical and thermal conductivity.

Chapter 3

Theory and Simulation Methods

3.1 Introduction

I explain the theory and calculations behind work conducted in this thesis. Thermodynamic quantities are explained and how convergence is seen in simulations. The properties calculated through DFT-MD methods are explained with further insight into the Kubo-Greenwood theory and the properties this gives. Calculated compression paths are explained allowing for comparison to experiment. Testing and simulation input are explained describing ensembles used and the various molecular dynamics input parameters.

3.2 Theory

3.2.1 Thermodynamic Properties

Simulations are done giving microscopic detail of a system at each time step (atomic momenta, positions and more). Statistical mechanics is used to obtain the macroscopic observables (pressure, internal energy and more). In the $6N$ dimensional phase space of a system with N atoms, and a particular point $\vec{R}(t)$ we have at time t observable $A(\vec{R})$. The

microscopic observable $A(\vec{R})$ varies with time and by the ergodic hypothesis the average of $A(\vec{R})$ over a sufficiently long time is the macroscopic observable A_{obs},

$$A_{obs} = \left\langle A(\vec{R}(t)) \right\rangle = \lim_{t_{obs}\to\infty} \frac{1}{t_{obs}} \int_0^{t_{obs}} A(\vec{R}(t))\mathrm{d}t \tag{3.1}$$

Machine limitations do not allow an infinite time interval and as such molecular dynamics simulations use a long finite time. Uncertainties in A are computed accounting for the appropriate non-Gaussian statistics [175].

Fluctuations in A as measured by the mean square deviation

$$\sigma_A^2 = \left\langle \delta A^2 \right\rangle = \left\langle A^2 \right\rangle - \left\langle A \right\rangle^2 \tag{3.2}$$

also contain useful information. Thermodynamic derivative quantities can be calculated, by using eq. (3.2). For example the heat capacity (C_V), is calculated from the fluctuations of the electronic free energy (U),

$$\sigma_U^2 = \left\langle U^2 \right\rangle - \left\langle U \right\rangle^2 = \sum_j U_j^2 P_j - \left\langle U \right\rangle^2 \tag{3.3}$$

where,

$$P_j = \frac{e^{-\beta U_j}}{Q(N,V,\beta)} \tag{3.4}$$

P_j is the probability that the system is in the jth quantum state and $Q(N,V,\beta) = \sum_j e^{-\beta U_j(N,V)}$ in the canonical ensemble and $\beta = 1/k_B T$,

$$\begin{aligned}
\sum_j U_j^2 P_j &= \frac{1}{Q}\sum_j U_j^2 e^{-\beta U_j} = -\frac{1}{Q}\frac{\partial}{\partial\beta}\sum_j U_j e^{-\beta U_j} \\
&= -\frac{1}{Q}\frac{\partial}{\partial\beta}(\left\langle U \right\rangle Q) = -\frac{\partial \left\langle U \right\rangle}{\partial\beta} - \left\langle U \right\rangle \frac{\partial \ln Q}{\partial\beta} \\
&= k_B T^2 \frac{\partial \left\langle U \right\rangle}{\partial T} + \left\langle U \right\rangle^2
\end{aligned} \tag{3.5}$$

As $U = E - TS_{el}$, where E is the internal energy, T is the electronic temperature and S_{el}

is the electronic entropy giving,

$$\left(\frac{\partial \langle U \rangle}{\partial T}\right)_V = \frac{\langle U^2 \rangle - \langle U \rangle^2}{k_B T^2} = \frac{\partial \langle E \rangle}{\partial T} - S_{el} \tag{3.6}$$

giving,

$$C_V = \frac{\sigma_U^2}{k_B T^2} + S_{el} \tag{3.7}$$

where k_B is the Boltzmann constant and T is the temperature at constant volume (V). We can similarly calculate the Grüneisen parameter (γ),

$$\gamma = V\left(\frac{\partial P}{\partial E}\right)_V = V\left(\frac{\partial P}{\partial T}\right)_V \Big/ \left(\frac{\partial E}{\partial T}\right)_V = V\left(\frac{\langle PE \rangle - \langle P \rangle \langle E \rangle}{k_B T^2 C_V}\right) \tag{3.8}$$

Errors are calculated on C_V and γ from the propagation of the errors in E and P. For further information of thermodynamic properties and fluctuations the reader is referred to [176, 177].

The chemical potential (μ_i) of a species (in a two component system) is the slope of the Gibbs energy, G, with respect to the number of atoms N_i of species i, eq. (3.9).

$$\mu_i = \left(\frac{\partial G}{\partial N_i}\right)_{P,T,N_{j\neq i}} \tag{3.9}$$

Depending on the shape of $G(N_i)$ it is possible for the Gibbs energy to be lowered by separation into two phases of different composition and equal chemical potential, for example a hydrogen-rich and a helium-rich phase, fig. 3.1.

To evaluate this possibility, we perform simulations in the NPT ensemble which yield the enthalpy,

$$H = E + PV \tag{3.10}$$

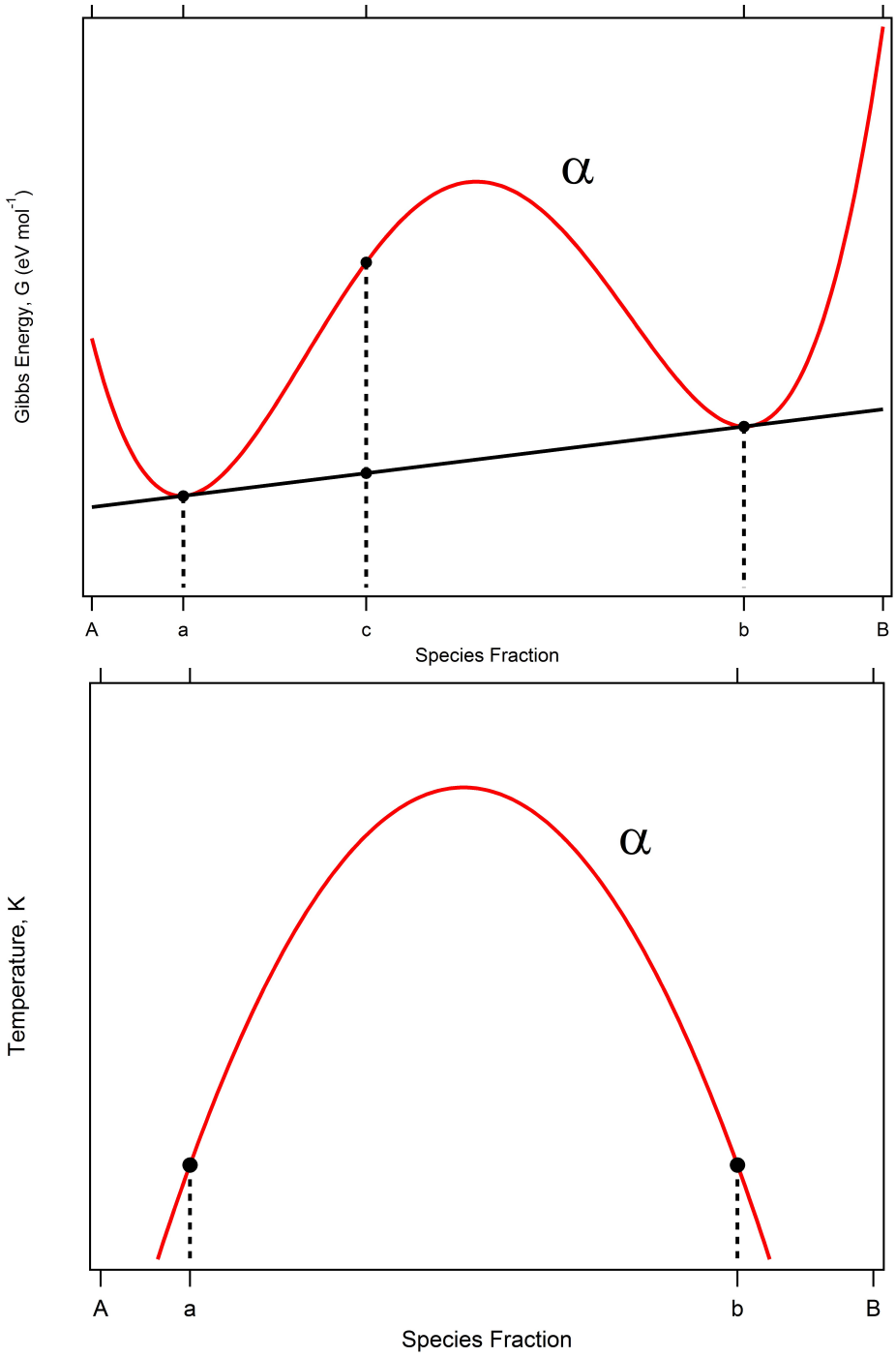

Figure 3.1: Gibbs Energy Curve and Phase Diagram. *Top:* Example Gibbs energy curve of composition α where species fraction c is shown to be unstable and will decompose into a lower Gibbs energy mixture of phases a and b along the common tangent construction. *Bottom:* Phase diagram from example Gibbs energy curve where conditions below state α is in a two-phase state of some fraction of a and b. Above the α the system is in equilibrium and homogeneous.

The Gibbs energy is,

$$G = H - TS \tag{3.11}$$

where H is the enthalpy, E is the internal energy, T is the temperature, S is the entropy, G is the Gibbs energy, P is the pressure and V is the volume. I obtain the entropy in the linear mixing approximation estimate,

$$\Delta S^{LM}(x) = x\ln x + (1-x)\ln(1-x) \tag{3.12}$$

where x is the helium number fraction, and $\Delta S = S(x) - xS(1) - (1-x)S(0)$.

3.2.2 Electronic Transport Properties

The Kubo-Greenwood formula for electrical conductivity $\sigma(\omega)$ [178, 179] is as follows,

$$\sigma(\omega) = \frac{2\pi e^2\hbar^2}{3m^2\omega\Omega}\sum_{\alpha}\sum_{k}W(k)\sum_{ij}F_{ij}|\langle\Psi_{j,k}|\bigtriangledown_{\alpha}|\Psi_{i,k}\rangle|^2\delta(\varepsilon_{i,k}-\varepsilon_{j,k}-\omega) \tag{3.13}$$

where terms e and m are the electron charge and its mass. Summations over i and j are over discrete energy bands, α averages the three spatial directions and Ω is the cubic supercell volume. The Fermi weight $F_{i,j} = F(\varepsilon_{i,k}) - F(\varepsilon_{j,k})$ is the difference in occupation of the ith and jth electronic energy bands and $\bigtriangledown_{\alpha}$ is the momentum operator acting on the wavefunctions $\Psi_{i,k}$. δ is a Dirac delta function. The summation over k-points includes the weight $W(k)$. The static frequency value of $\omega \to 0$ gives the Direct Current (DC) conductivity on a free charge moving freely over arbitrary distance in response to this DC field.

The electrical thermal conductivities by the Chester-Thellung formulation of the Kubo-Greenwood formula [180] is given by

$$\kappa(\omega) = \frac{1}{e^2 T}\left(L_{22}(\omega) - \frac{L_{12}(\omega)^2}{L_{11}(\omega)}\right) \tag{3.14}$$

where the coefficients L_{lm} are the Onsager coefficients [181] which through linear response theory describe the transport behaviour of a system in an electric field defined as,

$$L_{lm}(\omega) = (-1)^{l+m}\frac{2\pi e^2\hbar^2}{3m^2\omega\Omega}\sum_{i,j=1}^{n}\sum_{\alpha=1}^{3}[F(\epsilon_{i,k}) - F(\epsilon_{j,k})] \tag{3.15}$$
$$\times \left|\langle\Psi_{j,k}\left|\bigtriangledown_\alpha\right|\Psi_{i,k}\rangle\right|^2 [\epsilon_{j,k} - \mu]^{l-1}[\epsilon_{i,k} - \mu]^{m-l}\delta(\epsilon_{j,k} - \epsilon_{i,k} - \hbar\omega)$$

where μ is the chemical potential.

The link between the electrical conductivity and electrical thermal conductivity (both at $\omega = 0$) discovered by G. Wiedemann and R. Franz in 1853 [182] is known as the Wiedemann-Franz law. For a metal $\kappa(0)/\sigma(0) = LT$ where the Lorenz ratio, $L_0 \approx 2.44 \times 10^{-8}$ WΩK^{-2}. Note: the Lorenz number (L) is not to be confused with the Onsager coefficients (L_{lm}).

The Wiedemann-Franz relation is due to the heat and electrical transport both depending on the free electrons in the material. In a metal the thermal conductivity will increase with increasing temperature but electrical conductivity decreases with increasing particle velocity (brought on by increased temperature). Therefore, a departure from the expected L_0 value is either due to phonons also being significant in heat transport (where this will not effect our Kubo-Greenwood calculation as it only takes the electronic contributions) or inelastic scattering effecting the particle velocities and energy losses of order $k_B T$ during collisions thus affecting both thermal and electrical conductivities.

From the electrical conductivity, as given by the Kubo-Greenwood formula (eq. (3.13)), the real and imaginary part of the dielectric constant can be calculated. The imaginary

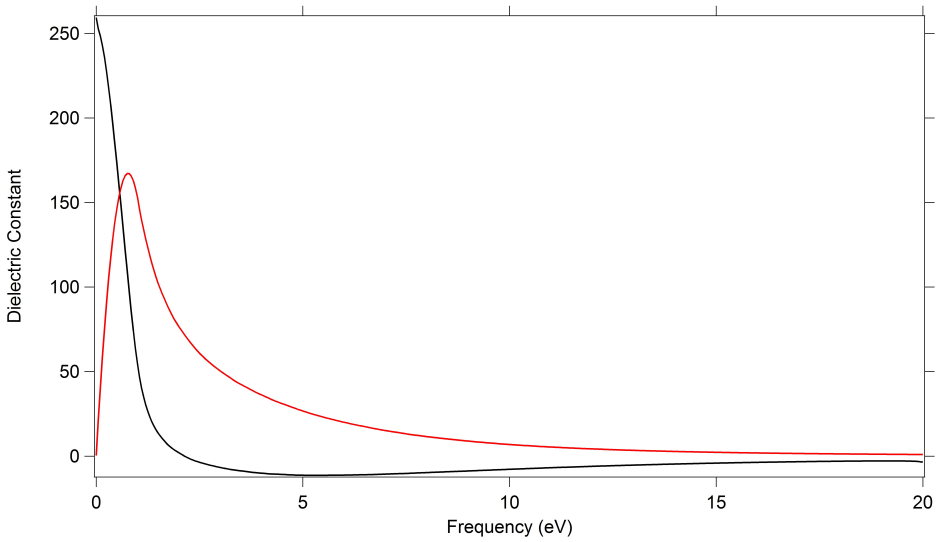

Figure 3.2: Real and imaginary parts of the dielectric constant as a function of frequency (eV). Results shown are for pure hydrogen at a density of 1500 kg m^{-3} at T = 1000 K and P = 611 GPa. The real part of the dielectric constant is shown as the black line and the imaginary part of the dielectric constant is shown as the red line as used in the calculation of the reflectivity.

part of the dielectric constant (shown in fig. 3.2 as the red line) is calculated from the relation given in [183, p. 776] eq. (3.16),

$$\varepsilon_2(\omega) = \frac{\sigma_1(\omega)}{\varepsilon_0 \omega}, \tag{3.16}$$

where $\sigma_1(\omega)$ is the real part of the conductivity and ε_0 is the permittivity of free space = 8.854187e-12 F/m. Next, using the Kramers-Kronig transformation, eq. (3.17), the real part of the dielectric constant (shown in fig. 3.2 as the black line) is calculated,

$$\varepsilon_1(\omega) = 1 + \frac{1}{\pi} P \int_0^\infty \frac{\varepsilon_2(\omega')\omega'}{\omega'^2 - \omega^2} d\omega' \tag{3.17}$$

where P denotes the Cauchy Principal Value of the integral allowing the evaluation of the improper integral.

The vacuum reflectivity, r, is calculated from the dielectric constant as follows, eq. (3.18),

$$r = \frac{(1-n)^2 + k^2}{(1+n)^2 + k^2} \tag{3.18}$$

where n is the real part of the square root of the dielectric constant and k is the imaginary part of the square root of the dielectric constant, ie $\kappa_d = \sqrt{\varepsilon}$, $n = \mathrm{Re}\,\kappa_d$, $k = \mathrm{Im}\,\kappa_d$, where κ_d is the total dielectric constant.

We gain additional insight into *ab initio* calculations of electrical conductivity via the approximate Mott-Ziman theory [184, 185]. The Ziman resistivity $1/\sigma_z$ at $\omega = 0$ is given by,

$$1/\sigma_z = \frac{a_0\hbar}{e^2}\frac{k_{TF}^2}{64ZE_F^2}\int_0^{2k_F} q^3 S(q)\nu^2(q)dq, \tag{3.19}$$

$$\nu(q) \approx \frac{-4\pi Ze^2}{q^2 + k_S^2} \tag{3.20}$$

where $S(q)$ is the structure factor with wave vector q, k_F is the Fermi wavevector and m is the electron mass. Using eq. (3.20) the effective ion-electron interaction $\nu(q)$ canonically includes a screening term (k_S), which we take to be zero as for the bare nuclear potential. The Ziman resistivity is then calculated by eq. (3.19), where $a_0\hbar/e^2 = 0.217\mu\Omega m$ is used, and E_F and k_F are the free-electron Fermi energy and wave vector respectively.

The Ziman theory assumes the free electron system. The influence of a pseudogap is included by means of eq. (3.21) [186], where $N_0(E_F)$ is the free-electron value of the density of states at the Fermi level, (the density of states being the number of states per unit cell volume Ω per unit energy E). Here $\overline{N}$ is the temperature-smoothed density of states at the chemical potential μ in eq. (3.22). Finally equation eq. (3.23) is used in calculating the electrical conductivity.

$$g = \frac{\overline{N}(\mu)}{N_0(E_F)} \tag{3.21}$$

$$\overline{N}(\mu) = \frac{\int N(\varepsilon)\frac{\partial f}{\partial \varepsilon}d\varepsilon}{\int \frac{\partial f}{\partial \varepsilon}d\varepsilon} \tag{3.22}$$

$$\sigma_{corrected} = g^2\sigma_z \tag{3.23}$$

3.2.3 Self-Diffusion Coefficient

The mean square displacement is calculated as fig. 3.3,

$$M(\Delta t) \equiv \left\langle \left(x\left(t\right) - x(t_0)\right)^2 \right\rangle \tag{3.24}$$

where $x(t)$ is the particle position at time t and angled brackets denote an ensemble average over all particles and over time origins t_0 and $\Delta t = t - t_0$.

From the mean square displacement we can see when the system has reached dynamical convergence. Once this is achieved the mean square displacement will be linear in time.

The self-diffusion coefficient can be calculated by taking the gradient of the linear part of the mean square displacement and dividing by 6, as in the relation determined by Einstein, eq. (3.25),

$$D = \frac{1}{2d}\lim_{\Delta t\to\infty}\frac{M(\Delta t)}{\Delta t} \tag{3.25}$$

where D is the self-diffusion coefficient and, d is the dimensionality of the system (where d=3 for our three dimensional space).

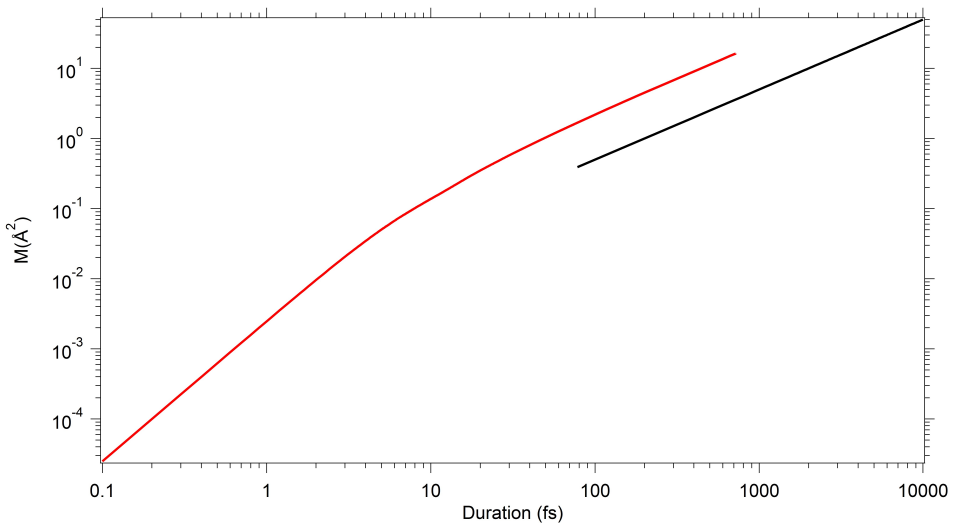

Figure 3.3: Mean Square Displacement showing convergence through MD simulation. Results are for pure hydrogen at a density of 1500 kg m^{-3} at T = 1000 K and P = 611 GPa. The red line shows the mean square displacement taken over all time origins and the black line indicates the unit slope expected of the diffusive process at long duration.

3.2.4 Structure

The atomic structure is analysed by the radial distribution function

$$g(r) = \frac{1}{4\pi r^2}\frac{1}{N_a\rho}\sum_{i=1}^{N_a}\sum_{k\neq i}^{N_a}\langle\delta(r-|r_k-r_i|)\rangle \tag{3.26}$$

where ρ is the number density ($\rho = N_a/V$), r is the particle distance in angstroms and subscripts i and k refer to individual atomic species. This gives the probability of finding one particle a distance r from a central particle.

We also consider the structure factors ($S(\mathbf{k})$) of the system by taking density fluctuations at $\mathbf{k}$, $\mathbf{k} = (2\pi/L)(k_x, k_y, k_z)$ where L is the box length and $k_{x,y,z}$ are integers. Then the Fourier transform of the number density is $\rho(\mathbf{k}) = \sum_{i=1}^{N_a} exp(i\mathbf{k}\cdot x_i)$, where N_a is the number of atoms and x_i is the atom coordinate. From ρ we can calculate $S(\mathbf{k})$

$$S(\mathbf{k}) = N_a^{-1} \langle \rho(\mathbf{k}) \rho(-\mathbf{k}) \rangle \tag{3.27}$$

Of particular interest in hydrogen-rich systems at high pressure is the transition from dominantly molecular (H_2) structure at low pressure to a dominantly atomic (H) structure at high pressure. I measure the progress of this structural change via the dissociation fraction,

$$\beta = \frac{N_a - 2n_2}{N_a} \tag{3.28}$$

where n_2 is the number of dimers. A completely atomic system corresponds to $\beta = 1$ and $\beta = 0$ to a completely molecular system. I use the nearest neighbour approach of only counting a molecule when two atoms are both mutual nearest neighbours of each other. Moreover I only count molecules that survive for a certain number of time steps. I take this to be equal to 10 vibrational periods where the H_2 vibrational frequency is $4161\,\mathrm{cm}^{-1}$ [187] giving ~ 80 fs (800 time steps) as the necessary interval for a molecule to be counted.

3.2.5 Compression Paths

Along the principal Hugoniot of a material the sample starts from an initially unshocked state of initial pressure P_0, internal energy E_0, initial density ρ_0. A shock wave of velocity U_s accelerates the material to velocity u_p. The final state has a pressure of P_1, internal energy E_1, and density ρ. From the conservation of mass, momentum and energy the above terms are related by the Rankine-Hugoniot equations ([188] and [189,190] translated in [191])

$$\text{mass conservation:} \qquad \rho_1(U_s - u_p) = U_s\rho_0 \tag{3.29}$$

$$\text{momentum conservation:} \qquad U_s u_p \rho_0 = P_1 - P_0 \tag{3.30}$$

$$\text{energy conservation:} \qquad P_1 u_p = \rho_2 U_s(\frac{1}{2}u_p^2 + E_1 - E_0) \tag{3.31}$$

Eliminating the two velocities gives the Hugoniot relation eq. (3.32),

$$E_1 - E_0 = \frac{1}{2}(P_1 + P_0)\left(\frac{1}{\rho_0} - \frac{1}{\rho_1}\right) = \frac{1}{2}(P_1 + P_0)(V_0 - V_1) \tag{3.32}$$

where V_1 and V_0 are respectively the final and initial specific volumes per unit mass.

Because the unshocked state is typically at very low temperature (room temperature or below) and DFT does not account for quantum effects we must make a correction to the internal energy as computed in our molecular dynamics simulations by the addition of the quantum harmonic oscillator and subtract the classical vibrational energy per molecule giving,

$$\Delta E = \beta \frac{1}{2} k_B \left[\Theta_{vib}\left(\frac{1}{2} + \frac{1}{\exp(\Theta_{vib}/T) - 1}\right) - T\right] \tag{3.33}$$

where β is the dissociation fraction, eq. (3.28), Θ_{vib} is the vibrational temperature given the value 4307 K for deuterium [187], T is the temperature and k_B is the Boltzmann constant.

An isentropic process is one in which the entropy is constant. From the definition of the Grüneisen parameter (γ) the temperature profile (T) is given by

$$\frac{\partial T}{\partial \rho} = \frac{T}{\rho}\gamma(\rho, T) \tag{3.34}$$

where ρ is the density. This ordinary differential equation may be solved by standard numerical techniques once $\gamma(\rho, T)$ is known.

3.3 Methods: Electronic Structure

MD simulations are conducted within the Vienna *Ab initio* Simulation Package (VASP) [192]. The Projected Augmented Wave method (PAW) is used as the solution to the electronic structure and calculates the total energy, forces and stresses. In calculating the exchange and correlation I use the van-der Waals Density Functional 2 (vdW-DF2) [104, 153, 193, 194] functional and I also use the Generalised Gradient Approximation, GGA [195], with the form of Perdew, Burke and Ernzerhof, PBE [102] to compare to vdW-DF2 results.

A plane wave cut-off energy of 1200 eV is used as per necessary for convergence of energies, a core radii of 0.80 Å is used for the hydrogen atoms and 1.1 Å for the helium atoms. A time step interval of 0.1 fs is used to capture the motion of the light hydrogen atoms through the simulation, with simulations requiring as much as 20 000 ionic steps (2 ps). A value of 1×10^{-6} eV (vdW-DF2) and 1×10^{-4} eV (PBE) is used for the break condition in the electronic self-consistency loop within VASP, and the Brillouin zone is sampled at zero wave vector ($k = 0$ Γ point) as, from testing, a higher number of k-points are unnecessary to meet convergence when using 1024 atoms (cubic shape), where I find convergence of the internal energy at ~ 0.2 meV/atom and ~ 0.6 kbar for the pressure.

The Kubo-Greenwood formulation, eq. (3.13), [178, 179] is implemented in VASP, and in doing this calculation I take 10 statistically spaced snap shots from the MD run. The snapshots are taken from the converged segment at spacings large enough to be considered statistically separated. Tests of k-points convergence found a $2 \times 2 \times 2$ k-point sampling was required for all temperatures and densities. A Dirac delta function broadening term δ is used within eq. (3.13) since we have a discrete energy spectrum resulting from the

finite simulation volume. The width of this broadening term is defined as the average electronic spacing between energy levels. Note, that the number of energy bands sampled is increased to make sure that there are plenty of unoccupied states available, which the Kubo-Greenwood method requires. Required values for the number of electronic bands range from 1000 for non-metallic systems to 2000+ for metallic systems when using 1024 atoms (for simulations of 256 atoms the number of electronic bands required range from 512 to 1000+ as required below for the calculation of the principal Hugoniot section 3.2.5). Electronic temperatures are chosen to be equal to nuclei temperatures.

3.4 Methods: Molecular Dynamics

A Nosé-Hoover thermostat is used to control the temperature oscillations with the Nosé-mass fixing the frequency of the temperature oscillations to a period of 40 time steps. An NVT ensemble is used where the number of atoms, N, the volume, V and the temperature, T, are constant throughout the MD run and electronic temperatures are set to equal the ionic temperature.

I also use in some H-He simulations the NPT ensemble simulations where some parameters are identical to that used for the NVT ensemble simulations with a plane wave cut-off energy equal to 1200 eV, a value of 1×10^{-6} eV as the break condition in the electronic self-consistency loop and a sampling of the Brillouin zone at zero wave vector ($k = 0$, Γ point). The chosen barostat is the Souza-Martins barostat as implemented by Hernandez [171,172] with a fictitious mass of 1×10^{-4} amu where the Nosé-Poincaré thermostat of Bond *et al.* [173] is now used.

3.4.1 Initial Conditions and Convergence Tests

Initial ion positions are chosen from previously converged simulations (i.e. a statistically uncorrelated liquid structure) of pure hydrogen at temperatures, $T \geq 1000$ K depending

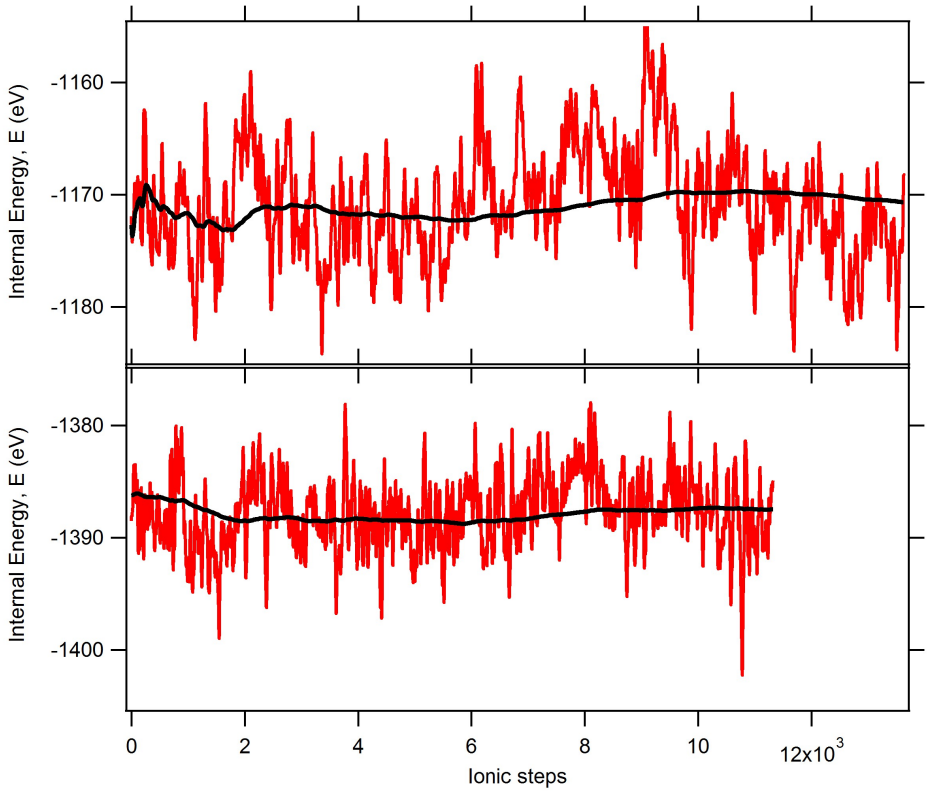

Figure 3.4: Internal energy fluctuations in pure hydrogen. Results are shown for 1000 K where the *top* figure shows the density of 1300 kg m^{-3} at P = 456 GPa (on the Widom line) and the *bottom* figure shows the density of 1250 kg m^{-3} at P = 439 GPa (just off the Widom line).

on the temperature of the current simulation. In the case of H-He mixtures the initial structure is taken from a pure hydrogen run and the helium ions are randomly populated, replacing the desired number of hydrogen ions with helium ions.

Simulations are allowed to continue for a minimum of 1000 time steps until convergence is met for the thermodynamic averages for pressure and internal energy (fig. 3.4). These quantities are monitored through the simulation until there is no significant change in the running average. The initial transient (20% of the total simulation) is discarded in the computation of averages.

3.4.2 Atom Number Conductivity Convergence

Electrical conductivity (σ) results are shown in fig. 3.5 showing the DC conductivities for different atom number simulations at 1000 K at the liquid-liquid phase transition of hydrogen using the PBE exchange correlation functional. General agreement is seen with the 512-atom simulations to that of Morales et al [79] which used 432 atoms. As previously shown for pressure in fig. 4.2 1024 atoms in the simulation cell is shown to correctly converge the DC conductivity in comparison to using 2048 atoms.

The inset shows the electrical conductivity as a function of photon frequency (eV) of three densities at the phase transition. Due to the finite sampling of the eigenvalue spectrum the conductivity non-physically falls to zero at zero frequency (not shown). I therefore extrapolate the conductivity to $\omega = 0$ using a Drude model when an increasing AC conductivity is observed going to lower frequencies, using $\sigma(\omega) = \sigma_0/(1 + \omega^2\tau^2)$, as in [120], where τ is the relaxation time used to fit to the data. Alternatively a linear fit is used when a decreasing AC conductivity is observed as $\omega \to 0$.

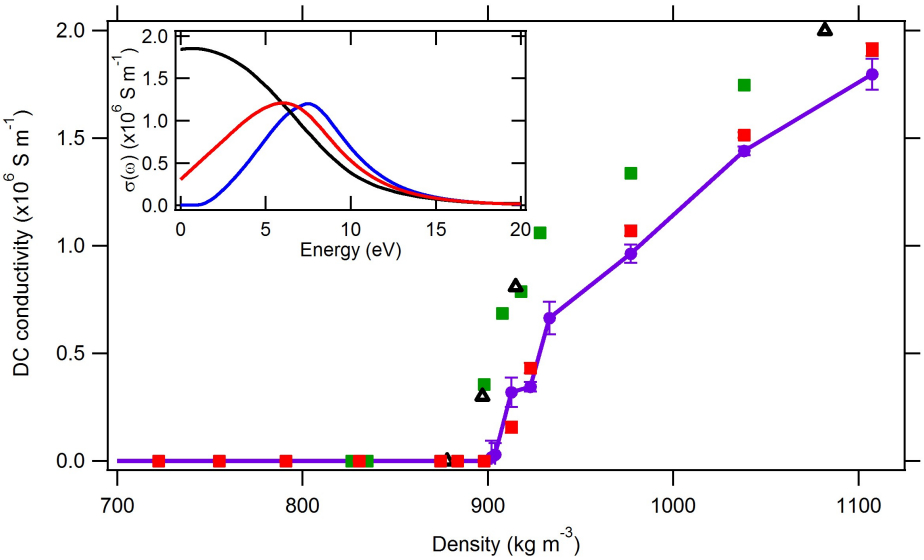

Figure 3.5: 1000 K DC conductivity vs density. Plot shows the dependence on the number of atoms with the PBE functional. Results are of 2048-atoms (red squares), 1024-atoms (purple circles, solid line), 512-atoms (green squares) and 432-atoms from Morales *et al.* [79] (open black triangles). *Inset:* PBE electrical conductivity as a function of energy for 1000 K at 1107 (black), 992 (red) and 830 (blue) kg m^{-3} showing initial electrical conductivity results calculated by the Kubo-Greenwood method.

Chapter 4

Hydrogen Thermodynamic Properties

I explore hydrogen at conditions of giant planet interiors with *ab initio* molecular dynamics. Hydrogen undergoes a first-order phase transition from a molecular to atomic liquid at high pressure. I find the super-critical extension of this transition to higher temperatures through anomalies in the Grüneisen parameter, heat capacity and dissociation fraction. I use the van der Waals exchange-correlation functional which is shown to produce a phase transition at much higher pressures and densities than does the generalised gradient approximation [95]. I find excellent agreement with the experimental deuterium principal Hugoniot.

4.1 Introduction

Hydrogen is the most abundant element in the universe, and it makes up the bulk content of giant planetary interiors, stars, stellar nebulae and more. This gives importance to understanding how it behaves under a large range of conditions. Knowledge of hydrogen

at the high densities and high temperatures found in giant planets is required, but is currently only adequately achievable through simulations. Experimental work has probed part of the pressure-temperature range of the Jovian interior [19, 20, 39, 80].

One of the most important questions concerning the interior of giant planets is the existence of a first-order liquid-liquid phase transition from a molecular to atomic hydrogen state. It is thought that this transition, if present, could produce a barrier to convection within Jupiter and other giant planets [9, 12, 196].

Hydrogen has been researched for many years. Early studies on its properties using classical and semi-classical models [16] at high pressures made some important predictions concerning the behaviour of hydrogen in the interior of gas giants. Among these was that hydrogen should become metallic at the liquid-liquid phase transition (LLPT). DFT has been used to calculate hydrogen properties more accurately [75, 79] and has shown some of these original predictions to be accurate. The specific exchange-correlation functional used within DFT has been shown to be important and can have large effects on properties such as the pressure and structure of the hydrogen atoms [95], with the location of the phase transition depending on the functional used. Models of planetary interiors depend sensitively on uncertainties associated with the choice of exchange-correlation functional [11].

Van der Waals (vdW) forces are commonly ignored in first principles calculations of hydrogen due to the difficulty in including non-local effects within the exchange-correlation functional of DFT. The non-local nature comes from eq. (2.26) showing the dependence on the point r to r'. The importance of the vdW-DF2 functional [104] on hydrogen is expected to decrease with increasing temperature and pressure due to greater kinetic forces masking the relatively weak vdW forces. Recent results comparing vdW-DF2 to the essentially exact Quantum Monte Carlo (QMC) simulations [101] shows more favourable results than PBE. Another possible explanation for this functional's improved results is that it is tuned towards exact-exchange [159]. Further, the LLPT location in pressure is

tested in [101] and shows vdW-DF2 agreeing with error bars with HSE. This gives further motivation to using vdW-DF2 in the simulations of hydrogen.

4.2 Methods

I have tested differences in various thermodynamic properties predicted between the vdW-DF2 [104, 194] and the GGA-PBE [195] functionals as implemented in VASP (Vienna *Ab initio* Simulation Package) [192]. First principles simulations are conducted for pure hydrogen within DFT where the Projected Augmented Wave method (PAW) [165, 197] is used as the solution to the electronic structure and calculates the total energy, forces and stresses.

After a simulation is converged, the radial distribution function $g(r)$ can be calculated, giving the proton-proton correlation function,

$$g(r) = \frac{1}{4\pi r^2} \frac{1}{N_a \rho} \sum_{i=1}^{N_a} \sum_{k \neq i}^{N_a} \langle \delta(r - |r_k - r_i|) \rangle \tag{4.1}$$

where ρ is the number density ($\rho = N_a/V$), r is the particle distance in angstroms and subscripts i and k refer to individual atomic species.

The principal Hugoniot is calculated from my simulations for comparison to experimental Hugoniot data for deuterium. Conservation of energy, mass and momentum give the Rankine-Hugoniot equation, eq. (3.32).

From experimental data on deuterium an initial density of 85.5 kg m^{-3} [23] at 20 K is used. The initial internal energy is calculated by a conjugate-gradient relaxation on a final state from a MD simulation conducted at the initial density at 1000 K giving $E_0 = -3.799$ eV/atom. As DFT does not account for quantum effects the internal energy is corrected by adding the quantum-mechanical harmonic oscillator and subtracting the

classical vibrational energy per atom eq. (3.33).

Comparisons between simulations using different numbers of k-points show no change from a sampling of the Brillouin zone at zero wave vector ($k = 0$, Γ point) to any higher order k-point sampling. I therefore chose a Γ point sampling as sufficient for hydrogen. Tests were also carried out for the plane-wave cut-off within VASP. Convergence of the internal energy was found at 1200 eV to within $\sim$ 0.2 meV/atom and is used throughout these results.

4.3 Results

4.3.1 Equation of State

All simulated temperatures and densities conducted for pure hydrogen are shown in fig. 4.1. The inset in fig. 4.1 shows vdW-DF2 and PBE results at the highest density conducted (9000 kg m^{-3}) at 1000 K, 2000 K and 5000 K showing pressure increasing with temperature also at higher densities. This behaviour is followed at all densities except at 1000 - 2000 K. At 2000 K just after its gradual (second-order) phase transition where the pressures here are below that of 1000 K until 1000 K reaches its first-order phase transition, fig. 4.2. PBE pressures are shown to be smaller than vdW-DF2 with results of 2000 K and 5000 K having significant differences. At the higher temperatures of 10 kK and above results show identical pressure. This shows the effect of these functionals on the pressures to be negligible for temperatures at and above 10 kK

The phase transition is first-order in character at 1000 K showing a van der Waals loop in pressure-density space (fig. 4.2). The properties of the first-order phase transition extracted via the Maxwell equal area construction converge at 1024 atoms as there are insignificant differences to 2048-atom simulations and thus I use a 1024-atom system for analysis of the phase transition. The vdW-DF2 phase transition results are shown in

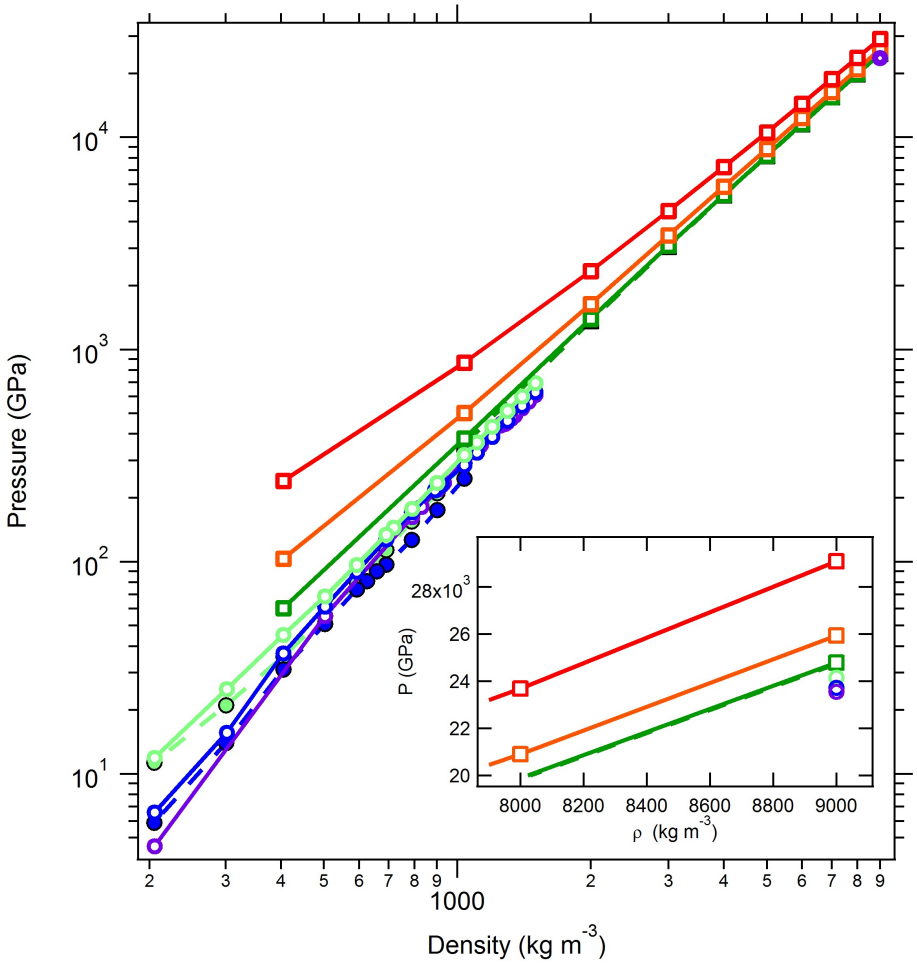

Figure 4.1: Pressure as a function of density for different isotherms of hydrogen. vdW-DF2 functional (open symbols): 1000 K (purple), 2000 K (blue), 5000 K (light green), 10 kK (green), 20 kK (orange) and 50 kK (red). For comparison, PBE (dashed line, closed symbols) at 2000 K, 5000 K and 10 kK. *Inset:* Highest density simulated at 9000 kg m^{-3} of all temperatures 1000 K to 50 kK. Also showing 10 kK PBE.

(fig. 4.2 Lower inset) showing a significant shift in the phase transition from ∼900 kg m^{-3} and 181 GPa for PBE to ∼1270 kg m^{-3} and 449 GPa for vdW-DF2.

The constant volume heat capacity (C_V/Nk_B) is shown in fig. 4.3. The heat capacity shows the effect of the phase transition at 1000 K producing a relatively sudden change (sharp increase) at the phase transition density ∼1300 kg m^{-3} and this feature is shown to continue to higher temperatures of 5000 K at ∼340 kg m^{-3}. I also see this discontinuity in the 256 atom simulations of 3000 K at ∼700 kg m^{-3}. PBE results show the discontinuity feature in C_V at the phase transition location predicted by PBE simulations occurring at ∼900 kg m^{-3}. For the higher temperatures reported (T $\geq$ 10 kK) the heat capacity shows a non-ideal behaviour (where $C_V^{ideal}/Nk_B = 1.5$), where no further discontinuity due to phase transitions are seen. C_V is shown here to decrease with increasing temperature beyond the density of $\sim$ 2500 kg m^{-3} where below this density results of C_V increase with increasing temperature.

Anomalies in the Grüneisen parameter (γ) occur at the same density-temperature regions as those in C_V (fig. 4.3). The Grüneisen parameter is seen to increase with increasing temperature at 1000 K to 5000 K the opposite to the trend seen in C_V. At higher temperatures (T $\geq$ 10 kK) the Grüneisen parameter is shown to decrease with increasing density and decrease with increasing temperature. A cross over of temperature effects occurs at $\sim$ 600 kg m^{-3} for the higher temperatures where the lower temperatures show an increase in Grüneisen parameter with increasing temperature throughout the densities sampled. Results show a tendency towards an ideal value of the Grüneisen parameter (2/3) as temperature and density are increased.

The principal Hugoniot of Deuterium (D_2) using vdW-DF2 is shown in fig. 4.4, calculated from the experimental D_2 initial condition of 85.5 kg m^{-3} at 20 K and initial internal energy -3.799 eV/atom, and using eq. (3.32). Principal Hugoniot simulations are conducted with 256 atoms as agreement in pressures and internal energies is seen with 1024 atoms at the lower densities simulated here, well below the phase transition. Good agreement

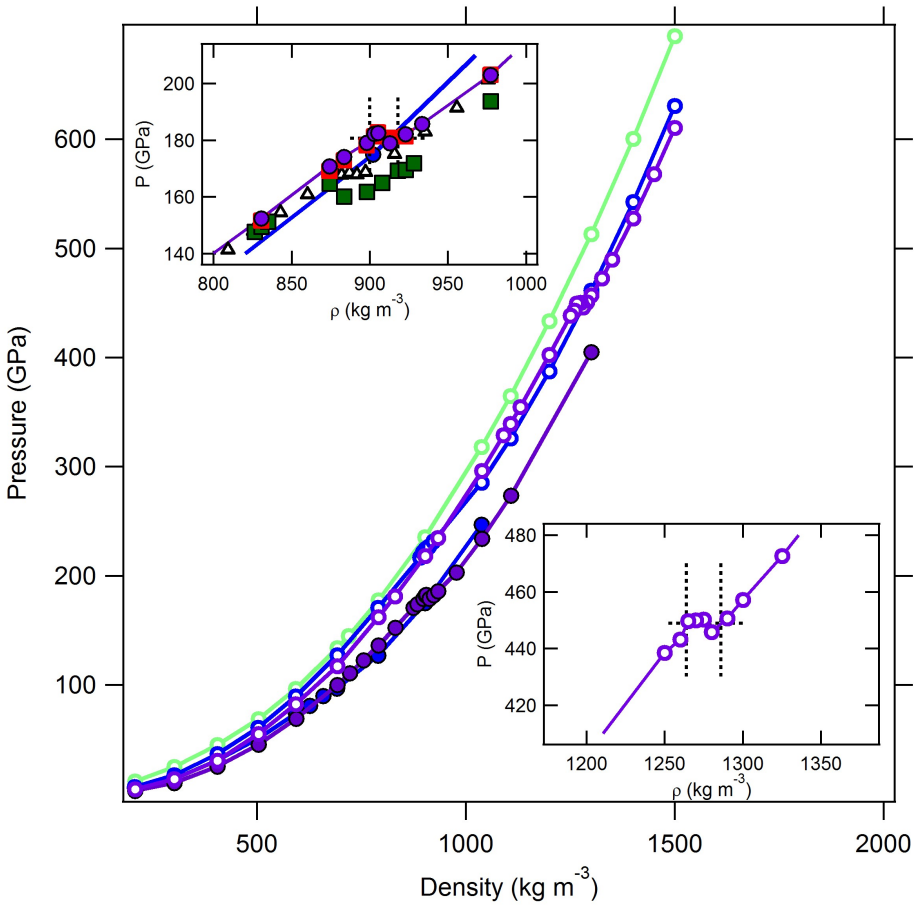

Figure 4.2: Pressure as a function of density for 1000 K (purple), 2000 K (blue) and 5000 K (light-green) isotherms of hydrogen (Temperatures are coloured equally for main and inset plots). VdW-DF2 (open circles) and PBE (closed circles). *Upper inset:* PBE phase transition showing dependence on atom number used. Phase transition marked with black dashed lines. Simulations of 1024 atoms are purple circles, 2048 atoms are red squares, 512 atoms are green squares and 2000 K PBE are closed circles. Results of Morales *et al.* [79] using PBE with 432 atoms shown as black triangles. *Lower inset:* vdW-DF2 phase transition with black dashed lines marking phase transition area. Errors are smaller than symbol sizes typically < 0.17 GPa (Root mean square deviation error).

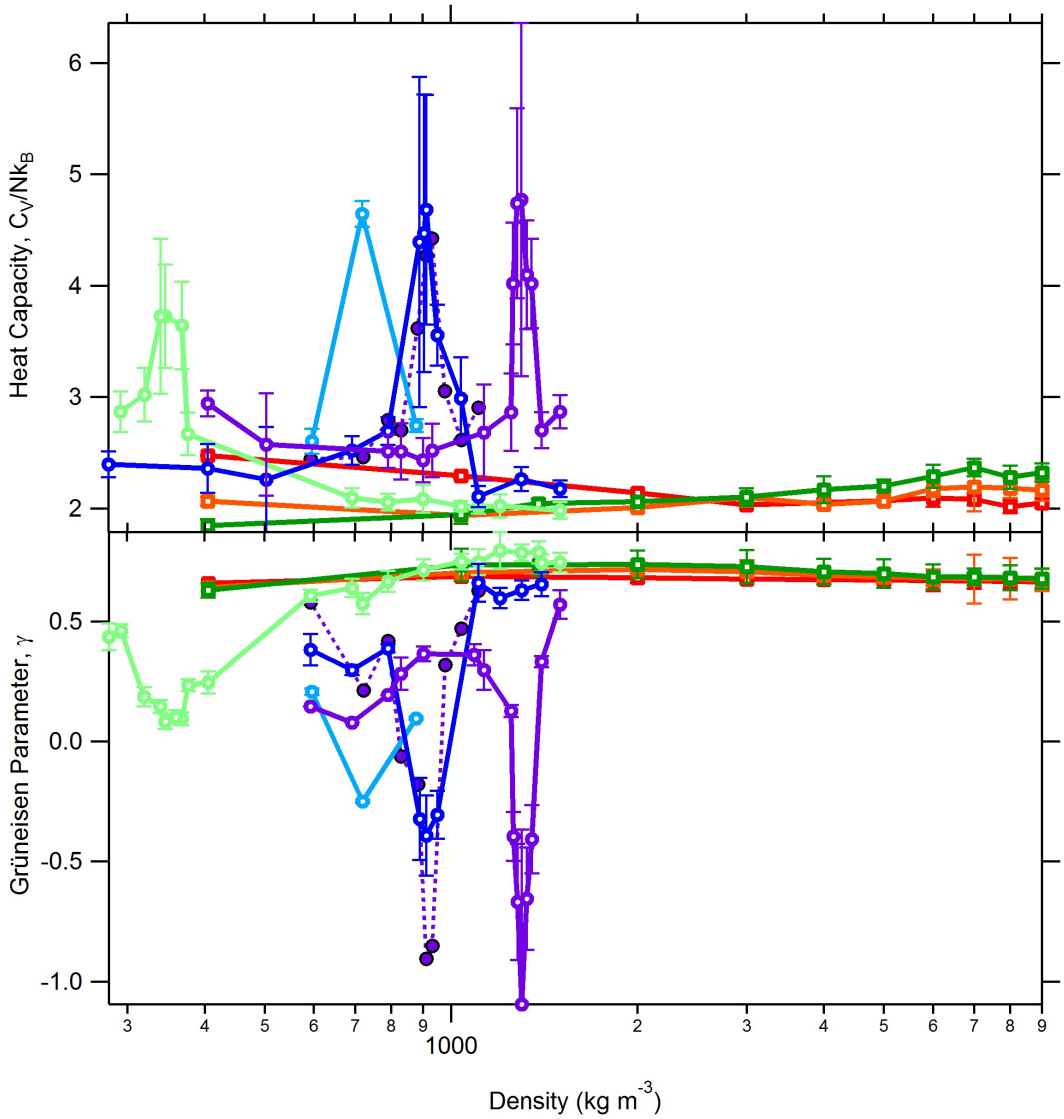

Figure 4.3: *top* panel: Heat capacity (C_V/NK_B) and *bottom* panel: Grüneisen parameter both as a function of density. VdW-DF2 (solid lines, open symbols) from fluctuation methods at 1000 K (purple), 2000 K (blue), 3000 K (cyan, 256-atoms), 5000 K (light-green), 10 kK (green), 20 kK (orange) and 50 kK (red). PBE results (dotted line, closed circles) are shown for 1000 K (purple) only.

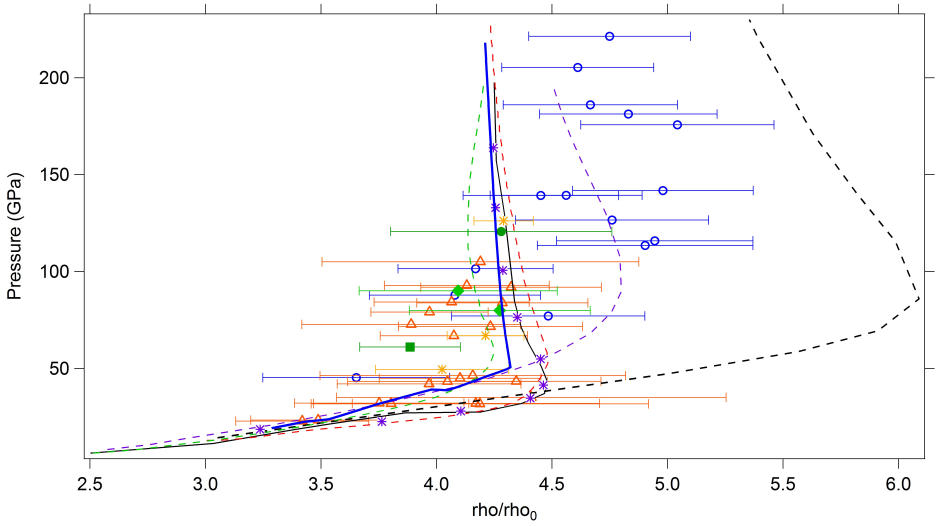

Figure 4.4: Deuterium principal Hugoniot. Results are shown for our 256 atom simulations on a comparison to deuterium initial density of 85.5 kg m^{-3} (blue solid line). Data from shock experiments are shown for laser-driven shock of Hicks *et al.* [26] (blue circles), impedance-match method of Knudson *et al.* [23, 40] (orange triangles), explosive shock Grishechkin *et al.* [51] (green diamonds), Boriskov *et al.* [50] (green circles) and Belov *et al.* [21] (green squares). Results from various chemical models: Ross [54] (black dashed line), Kerley *et al.* [53] (green dashed). From FVT: from Juranek *et al.* [198] (purple dashed line). From PBE: Holst *et al.* [199] (black solid line), Caillabet *et al.* [200] (red dashed line), Desjarlais [201] (purple stars). RPIMC: Militzer *et al.* [202] (orange stars).

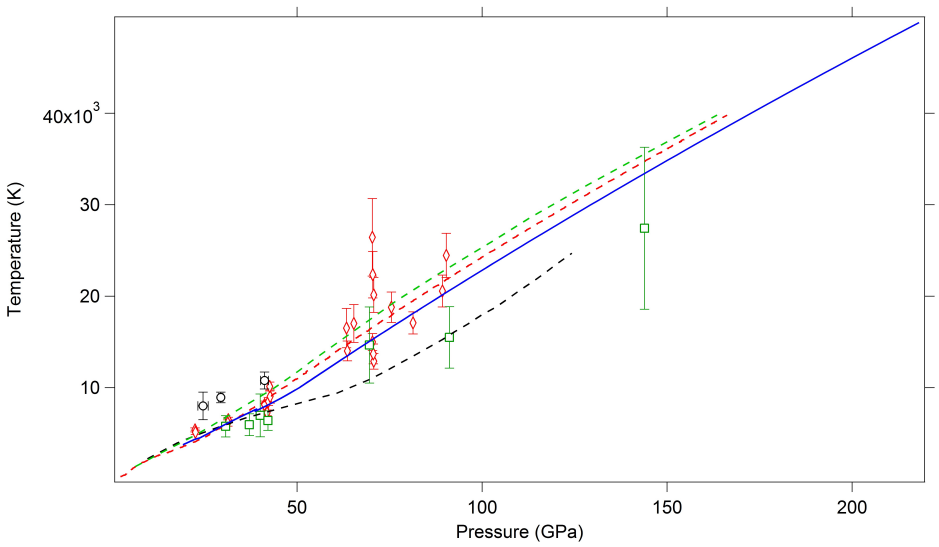

Figure 4.5: Temperature as a function of pressure through the principal Hugoniot of deuterium. Comparison of the D_2 Hugoniot from various theoretical studies and experimental data in the P-T diagram. Z machine experiments of Bailey *et al.* [203] are red diamonds, laser experiments of Collins *et al.* [92] are green squares. Dashed line results (green, red and black dashed lines) are as in fig. 4.4 with the inclusion of the liquid hydrogen principal Hugoniot laser-driven shock data of Sano *et al.* [39] are black open circles.

is seen with Knudson *et al.* [23, 40] and with PBE results at high pressure from Holst *et al.*, Caillabet *et al.* and Desjarlais [199–201] though showing disagreement for the location of maximum compression. There is generally good agreement at lower pressures with the slope matching experimental results of Knudson *et al.*.

Temperature against pressure along the principal Hugoniot is shown in fig. 4.5. Experimental data of Bailey *et al.* show large discrepancies at high pressures and temperatures but good agreement is seen due to the scatter of their data. Excellent agreement is seen below 50 GPa and 10 K between all work shown.

4.3.2 Structure

I now analyse the atomic structure of the system by means of the radial distribution function to gain further insight into the change in structure through the phase transition as molecular hydrogen becomes atomic. Figure 4.6 shows the vdW-DF2 radial distribution

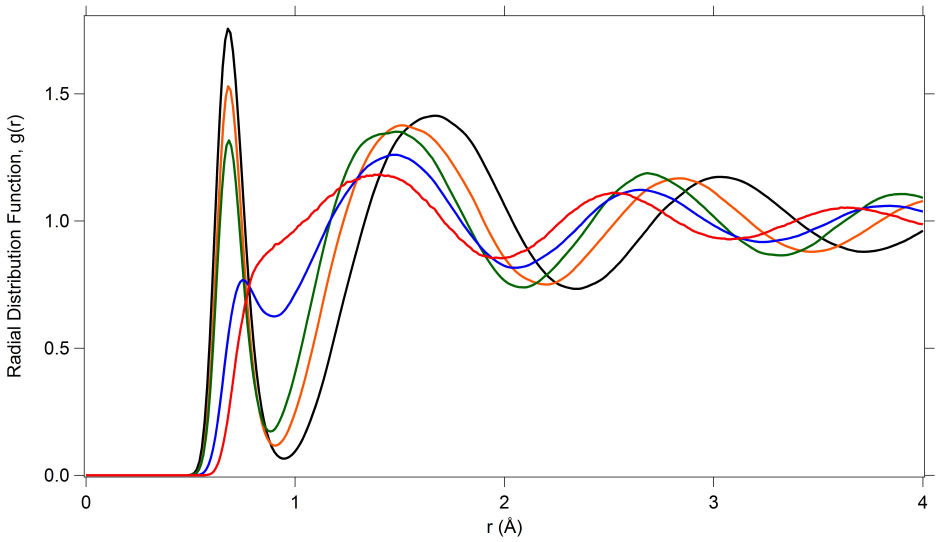

Figure 4.6: 1000 K Radial Distribution Functions of hydrogen. vdW-DF2 results through a range of densities going through the liquid-liquid phase transition. Densities shown: 1500 kg m^{-3} red line, 1325 kg m^{-3} blue line, 1265 kg m^{-3} green line, 1107 kg m^{-3} orange line and 902 kg m^{-3} black line.

function evolution at 1000 K. A gradual change from molecular, at lower densities, to a more atomic system at higher densities is seen. The first (molecular) peak eventually fades and the peak position shifts to larger distances, indicating the nuclei are separating as the density is increased.

The dissociation fraction (β) calculated using eq. (3.28) is shown in fig. 4.7. The molecular to atomic transition occurs over a broader range as density and temperature increases. Nevertheless the transition is well defined even at 5000 K. The structural transition occurs at higher densities in vdW-DF2 as compared with PBE: the hydrogen atoms are kept in the molecular state to higher densities.

Interpolated pressures at $\beta = 0.5$ are shown in fig. 4.8 (i.e. half atomic and half molecular) for vdW-DF2 and are compared with my PBE and PBE from Tamblyn *et al.* [204]. This can be seen as the phase diagram boundary for a molecular to atomic state for liquid hydrogen where vdW-DF2 is predicting a shifted boundary to higher pressures. Results are also shown here of the pressures of the anomalies in heat capacity and Grüneisen

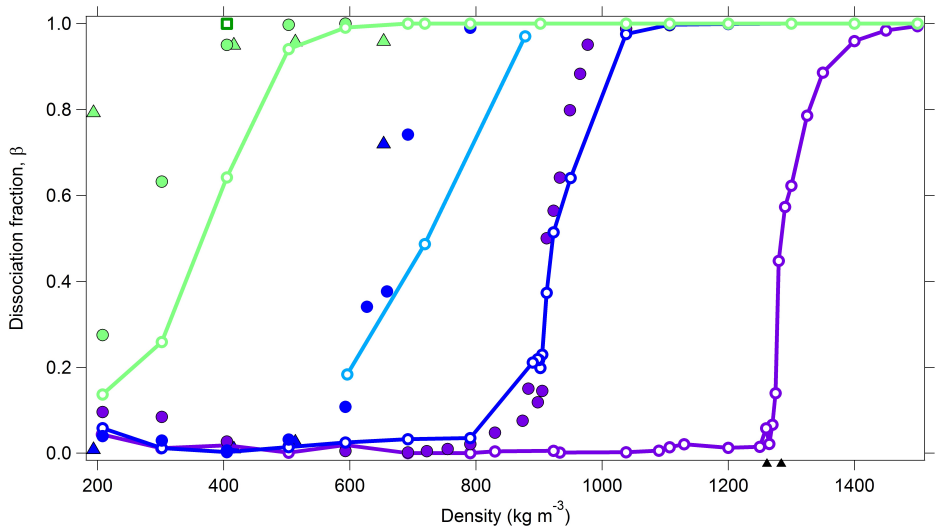

Figure 4.7: Dissociation fraction as a function of density. Values are from taking bond lifetime as $\sim$ 80 fs shown as solid lines. VdW-DF2 1000 K (purple, open circles) showing the location and range of the liquid-liquid phase transition in density with black arrow markers, PBE 1000 K (purple, closed circles). VdW-DF2 2000 K (blue, open circles), PBE (blue, closed circles). 3000 K vdW-DF2 (cyan, open circles). 5000 K vdW-DF2 (light-green, open circles), PBE (light-green, closed circles). 10 kK vdW-DF2 (green, open square) showing a slightly lower than fully atomic value at 405 kg m^{-3} (PBE completely atomic at this condition). Vorberger *et al.* [91] PBE results using 128 atoms are shown as closed triangles for 2000 K and 5000 K.

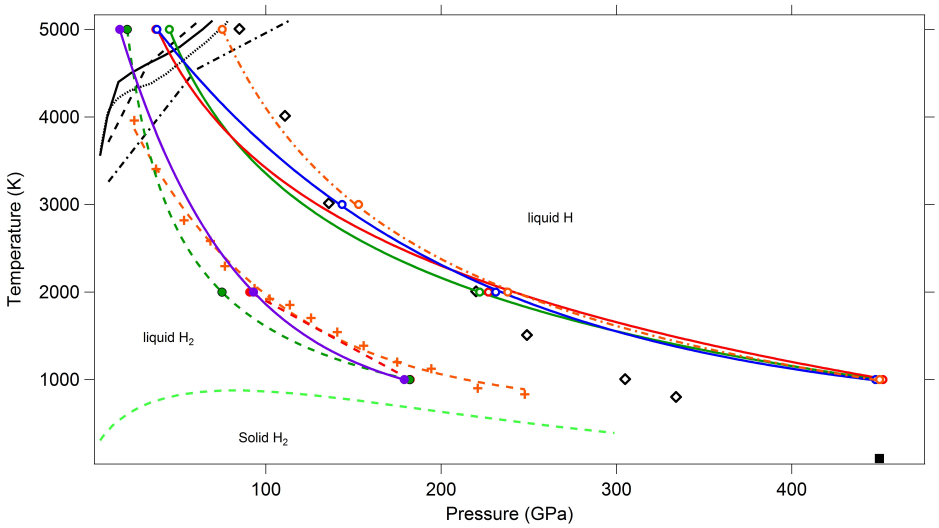

Figure 4.8: Pressures at predicted phase transition. Values are interpolated for dissociation fraction $\beta = 0.5$ with vdW-DF2 (blue open circles) showing densities from (all densities shown here are reported left to right): 371, 723, 921 and 1284 kg m^{-3} and PBE (purple closed circles, solid line) showing densities: 264, 670 and 912 kg m^{-3} shown with PBE results of Tamblyn *et al.* [204] (orange crosses, dashed line). Results are shown for the phase transition predicted by the heat capacity (C_V) and Grüneisen parameter (γ) with vdW-DF2 (red open circles, solid line) showing densities: 368, 719, 912, and 1300 kg m^{-3} and for PBE (red closed circles, dashed line) at densities: 659 and 923 kg m^{-3}. Results are also shown for the predicted phase transition from the self-diffusion coefficient (shown in chapter 5) for vdW-DF2 (green open circles, solid line) with densities: 405, 900 and 1265 kg m^{-3} and for PBE (green closed circles, dashed line) at densities: 301, 593 and 301 kg m^{-3}. Comparisons are made of the pressures and temperatures at a conductivity of 0.2 $\times 10^6$ S m^{-1} from this work DFT vdW-DF2 (open orange circles, dotted-dashed line) to Path Integral Molecular Dyanmics (PIMD) simulations also using the vdW-DF2 functional [95] (black open diamonds). The solid to liquid melt line of hydrogen as calculated from first principles Bonev *et al.* [78] (light-green dashed line) and the solid hydrogen extrapolated band gap closure in diamond anvil cell experiments of Loubeyre *et al.* [2] (black square). Jovian isentropes are from French *et al.* [205] (black solid line), Nettelmann *et al.* [206] (black dotted line) and as shown in Bagenal *et al.* [12] both the Jovian isentrope (black dashed line) and the Saturnian isentrope (black dashed dotted line).

parameter from vdW-DF2 and PBE showing good agreement with the $\beta = 0.5$ curves. Isentropes show these gas giant planets should pass the phase transition at 5000 K where no first-order behaviour is present.

4.4 Discussion and Conclusions

VdW-DF2 is shown to predict a first-order phase transition in hydrogen at 1000 K at the pressure of 449 GPa. The density contrast is 22 kg m^{-3}. The phase transition is shown to persist to higher temperatures (shown up to 5000 K) but it is no longer a first order phase transition (no van der Waals loop). The phase transition occurs at progressively lower densities with increasing temperature giving the phase diagram shown in fig. 4.8 marking the molecular to atomic line. This figure shows the phase transition pressures as predicted from the dissociation fractions, the heat capacity (and γ) and the self-diffusion coefficient (chapter 5) showing all these properties producing the same line up to 5000 K.

The similarities of the phase transition properties predicted by both functionals are also seen in the dissociation fraction (fig. 4.7). While there is a density shift for the phase transition, the gradients of the dissociation fraction (at the phase transition) is similar for both functionals. Results for both functionals show the first-order behaviour vanishing after 1000 K with 2000 K showing a second-order phase transition. Similarities are also seen in both functionals with the C_V and γ results with the anomalies showing equal magnitude but with the shifted density location.

The higher temperatures of 10 - 50 kK (fig. 4.1) show differences in pressure between both functionals to be minimal at all densities shown. The agreement is shown to occur at 10 kK with vdW-DF2 and PBE results being approximately identical. Other properties are also equal at these higher temperatures such as the C_V and γ showing vdW-DF2 effects to only be important below a temperature of 10 kK.

We expect the vdW-DF2 results presented here to be more accurate than earlier PBE results on the basis of comparison with essentially exact calculations based on Quantum Monte Carlo (QMC). Comparison of test sets of condensed periodic molecular and atomic structures show that vdW-DF2 agrees better with QMC energetics than does PBE [101]. QMC molecular dynamics simulations show a much higher molecular to atomic transition

pressure than does PBE [207]. We also find a much higher transition pressure with vdW-DF2, although not nearly so high as the QMC molecular dynamics study. Some caution should be applied to the QMC molecular dynamics results however, as they are based on much smaller systems than we have featured here (256 atoms vs. our 1024 atoms). Further, as shown in fig. 4.8 DFT vdW-DF2 results agree well with PIMD vdW-DF2 results of [95], showing nuclear quantum effects described in the PIMD approach to have negligible effect above 2000 K.

The differences between vdW-DF2 and PBE are largest in the vicinity of the phase transformation. The vdW-DF2 functional in addition to predicting a higher pressure for the molecular to atomic transition also predicts a much smaller density contrast across the transition. The density in vdW-DF2 is lower than that in PBE over a wide pressure interval in the temperature range 1000-5000 K. Differences between the two functionals however diminish at high temperatures, and at densities both higher and lower than the liquid-liquid phase transition. The higher temperatures of 10 - 50 kK (fig. 4.1) show differences in pressure between both functionals to be minimal at all densities shown. The agreement is shown to occur at 10 kK with vdW-DF2 and PBE results being approximately identical. Other properties are also equal at these higher temperatures such as the C_V and γ showing vdW-DF2 effects to only be important below a temperature of 10 kK.

Because the difference between vdW-DF2 and PBE becomes small at temperatures greater than 5000 K, we expect the impact of the newer exchange-correlation functional on models of the giant planetary structure to be most significant for planets older and colder than Jupiter or Saturn. The reason is that the Jovian and Saturnian interiors intersect the structural transition at relatively high temperature (5000 K) and relatively low pressure, affecting little of the planet's mass.

We find that vdW-DF2 agrees reasonably well, within large experimental uncertainties, with the experimental principal Hugoniot at least up to 100 GPa and that the agreement is comparable to previous PBE calculations. Serious disagreement among different ex-

periments at high pressure make comparison difficult. Our results lie within and towards the lower density side of existing experimental Hugoniot points with the maximum compression at $\rho/\rho_0 = 4.32$ as compared with $\rho/\rho_0 = 4.46$ from PBE. Among the sources of experimental uncertainty that have been discussed are uncertainties in the equation of state of the standard in impedance matching experiments [26], and the quality of the sample-standard interface in the case of absolute density measurements at the NOVA laser [28].

Hydrogen shows an exceptionally clear example of the Widom line: a continuation of the first order phase transition into the super-critical regime as defined by extrema in thermodynamic properties. Indeed, the location of anomalies in the compressibility, heat capacity, and Grüneisen parameter all coincide in pressure-temperature space to within the resolution of our simulation over the entire extent of the Widom line. Moreover the Widom line in hydrogen is closely linked to changes in the underlying microscopic physics: thermodynamic anomalies coincide with the change in structure from molecular to atomic at $\beta = 0.5$, and with a rapid increase in the electrical conductivity and self-diffusion coefficient (chapter 5). The situation contrasts with that of the Lennard-Jones system in which the structural change across the Widom line is subtle and anomalies in different thermodynamic properties follow different paths in pressure-temperature space, converging only at the critical point [208].

Chapter 5

Hydrogen Transport Properties

Ab initio molecular dynamics simulations are conducted on hydrogen at conditions of giant planet interiors. Transport properties are calculated such as the self-diffusion and electrical conductivity where these properties are shown to have anomalies at the predicted phase transition. Conductivity is shown through the phase transition boundary in a comparison between exchange-correlation used showing larger differences at lower temperature. Finally, conductivity and reflectivity are calculated along the principal Hugoniot and compared with experimental data showing excellent agreement. Analysis of the underlying properties that affect the conductivity show structural properties to be of significant importance in explaining its change with temperature and density.

5.1 Introduction

The onset of metallic conductivity in hydrogen and its subsequent change with temperature and density has been of great interest to scientists and has been studied through various theoretical methods such as semi-classical models [67, 209], *ab-initio* first principles using DFT [79, 210] and experimental methods [20, 29]. Experimental methods have had important advancements in measuring conductivity at the extreme conditions

required for hydrogen metallisation. Single shock experiments [19, 29] and double shock experiments [20] show evidence for hydrogen becoming conductive at extreme conditions. Theoretical studies have also shown metallisation in hydrogen and its change with increasing pressure and temperature [79, 210, 211]. There are still many questions as to the exact characteristics of hydrogen conductivity and what factors are involved in its onset and change.

Here I will show the importance of which functional is used and how this changes the onset of electrical conductivity in hydrogen. Mott-Ziman methods are shown and give insight to the mechanism responsible for electrical conductivity at these conditions where this method has shown good agreement in describing conductivity against experiment for alkali metals [212, 213] and for some other materials [214–216]. An interesting point shown here is the maximum electrical conductivity reached at various densities with increasing temperature and the comparison between the Kubo-Greenwood and Mott-Ziman methods of the onset in conductivity. Reflectivity is shown next with emphasis on comparison to experimental work.

5.2 Results

Results of the self-diffusion coefficient, calculated from the Mean Square Displacement using the relation determined by Einstein (eq. (3.25)), in fig. 5.1 show a large difference with functional used. Here I compare to the self-diffusion coefficient of Stevenson *et al.* [16] obtained from their hard sphere model. Contrary to the DFT results the hard sphere model shows a decrease in self-diffusion coefficient from molecular to atomic phases.

The electrical conductivity from Kubo-Greenwood calculations are shown in fig. 5.2. Results show the conductivity increasing rapidly with compression and temperature in the vicinity of the liquid-liquid phase transition. VdW-DF2 shows a lower conductivity than PBE due to the shift to higher pressure and density of the phase transition. At higher

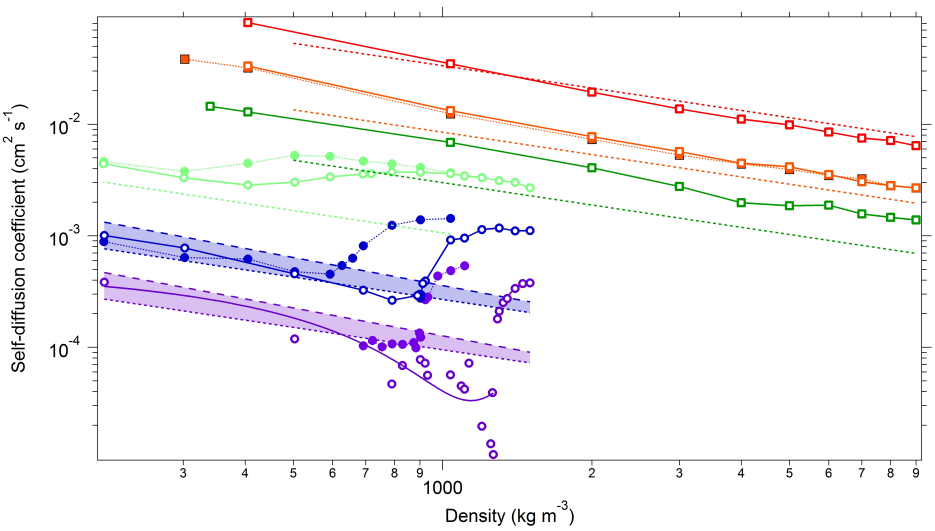

Figure 5.1: Hydrogen self-diffusion coefficient against density. VdW-DF2 results are shown as open circles from 1000 K (purple), 2000 K (blue) to 5000 K (light-green) and open squares from 10 kK (green), 20 kK (orange) to 50 kK (red), where closed circles and squares are of PBE results. From the hard sphere model of Stevenson *et al.* [16] dotted lines refer to metallic state and at the temperatures of 1000 K and 2000 K dashed lines (with shaded region) show molecular state diffusions.

densities the conductivity continues to increase on compression but more gradually. On heating at high density the conductivity decreases with maxima in conductivity shifting to lower pressures at higher temperatures, where at the highest pressure the maximum is seen at 2000 K. Good agreement is seen with Path integral Molecular Dynamics (PIMD) results at 3000 K and 5000 K. The minimum metallic conductivity, as calculated from Mott [217] is shown as the grey line from $0.03e^2/\hbar 2a$, where a is the Wigner-Seitz radius, e is the electron charge and $\hbar = h/2\pi$ where h is the Planck constant. DC conductivity is plotted along the principal Hugoniot of deuterium in fig. 5.3 showing good agreement with experimental single shock data of Nellis *et al.* [29].

Reflectivity calculated from the electrical conductivity from the Kubo-Greenwood formula, is shown in figs. 5.4 and 5.5. General agreement is seen for vdW-DF2 and precompressed experimental data of Loubeyre *et al.* [22], where the highest reflectivities reported are at a temperature of $\sim$ 5000 K giving good agreement to the vdW-DF2 5000 K. PBE results show a large shift to higher reflectivities. The reflectivity along the principal Hugoniot

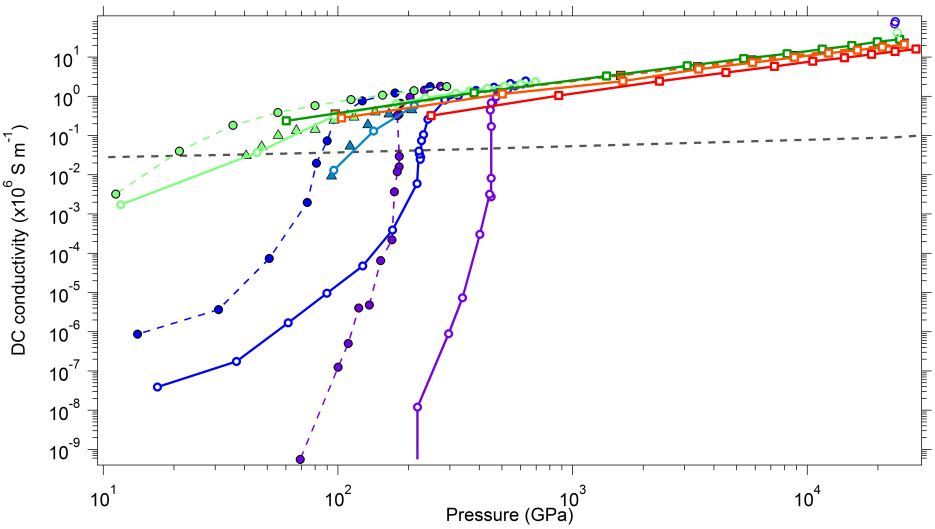

Figure 5.2: DC conductivities of hydrogen at 1000 K (purple), 2000 K (blue), 5000 K (light-green), 10 kK (green), 20 kK (orange) and 50 kK (red) with vdW-DF2 (solid lines, open circles). PIMD results using vdW-DF2 functional (triangles) [95] at 3000 K (cyan) and 5000 K (light-green). Note: all are 1024 atoms except the 3000 K (cyan open circles) which are 256 atoms simulations showing good agreement with PIMD (triangles). PBE are dashed lines with closed circles. The Mott minimum conductivity is shown as the solid grey line [217].

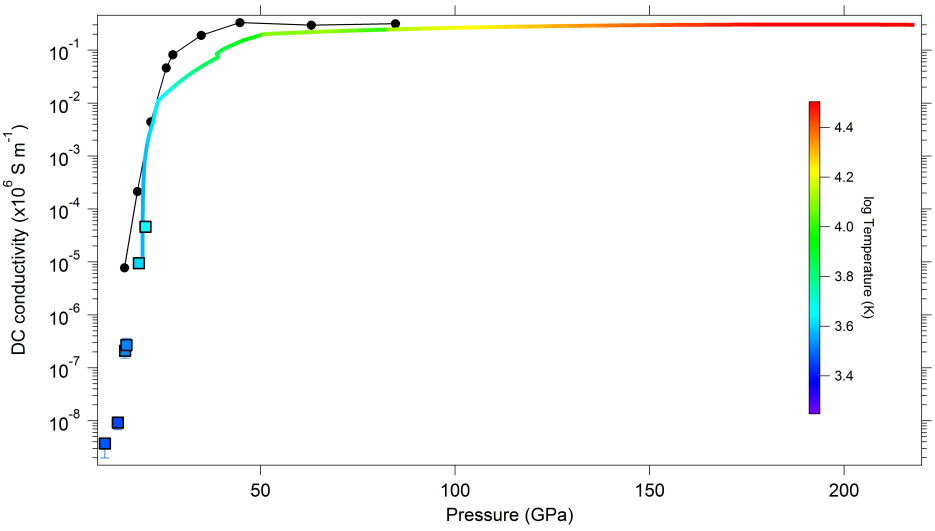

Figure 5.3: DC conductivity along the principal Hugoniot of deuterium (coloured line indicating temperature). Experimental results (squares) are light-gas gun shock experiments of Nellis *et al.* [29] coloured for temperature as in scale. PBE principal Hugoniot results are from Holst *et al.* [199] (black).

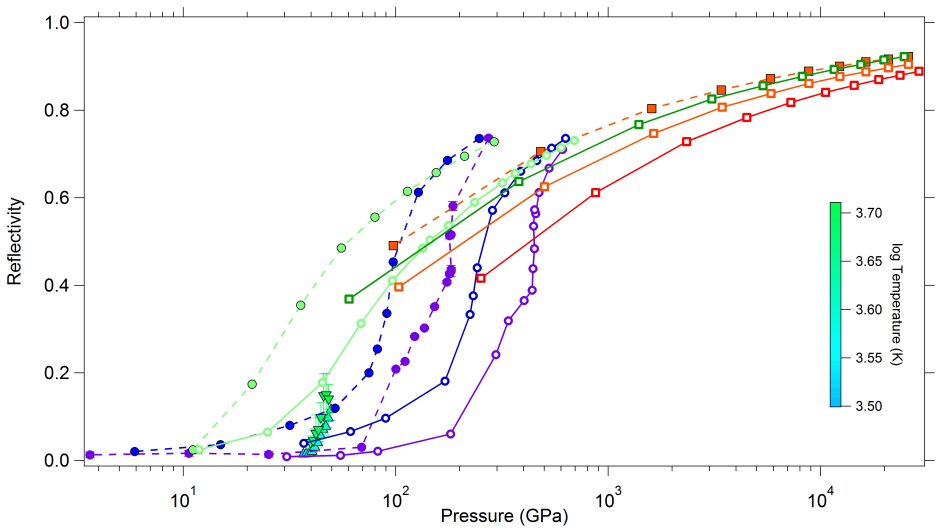

Figure 5.4: Reflectivity at 532 nm against pressure. Results are from vdW-DF2 (open symbols) at temperatures of 1000 K (purple), 2000 K (blue), 5000 K (light-green), 10 kK (red), 20 kK (blue), 50 kK (green). PBE (closed circles and squares) shown at 1000 K, 2000 K, 5000 K and 20 kK. Errors are approximately the size of symbols. Loubeyre *et al.* [22] precompressed experiments from 3500 - 4300 K (up triangles) and 4600 - 5200 K (down triangles) coloured for temperature as in legend.

agrees within experimental scatter with the results of Loubeyre *et al.* [28] and Celliers *et al.* [218].

The electrical thermal conductivity (κ) is shown in fig. 5.6 as calculated by the Chester-Thellung formulation of the Kubo-Greenwood formula (eq. (3.15)). Thermal conductivity is seen to increase with increasing temperature and density at all conditions. The Lorenz number (L) is shown in the *inset* of fig. 5.6 calculated with the thermal conductivity and electrical conductivity giving the expected free-electron value in the atomic phase showing the behaviour of a metal. The Lorenz number is seen to differ from this value in the molecular state at all temperatures. Hydrogen therefore does not follow the Wiedemann-Franz Law at pressure $<$ 400 GPa. This indicates the importance of inelastic scattering of electrons.

DC conductivity results are shown at 0.5 dissociation in fig. 5.7. Conductivity increases on compression and cooling along the Widom line in both vdW-DF2 and PBE results.

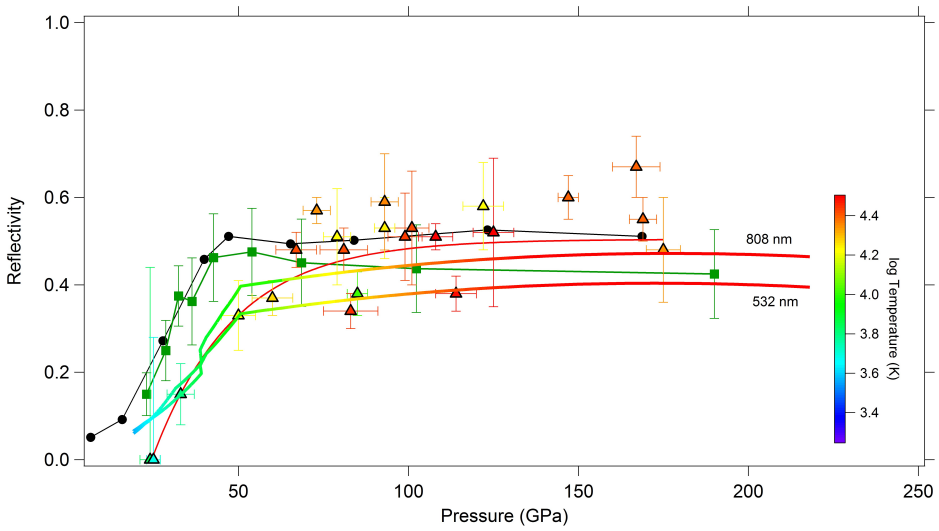

Figure 5.5: Reflectivity at 808 nm and 532 nm along the principal Hugoniot of deuterium (multi-coloured line indicating temperatures as in legend). Laser-driven shock experiments by Loubeyre *et al.* [28] at 532 nm with multicoloured triangles showing temperatures and the red solid line is a guide to the eye. Shock compression experiments of Celliers *et al.* [218] at 808 nm shown along experimental principal Hugoniot (green) and PBE principal Hugoniot results from Holst *et al.* [199] (black) also at 808 nm. FVT results [219] are shown as dashed orange line.

The conductivity from vdW-DF2 is lower than that from PBE at $\beta = 0.5$ indicating that vdW-DF2 has a larger pseudogap for similar underlying ionic arrangement.

Mott-Ziman calculation results are shown with conductivity from the Kubo-Greenwood method in fig. 5.8 showing remarkably good agreement in the onset of metallisation occurring at the phase transition of hydrogen.

Figure 5.9 shows the local maximum in the conductivity on heating which occurs over a wide range of density in both Kubo-Greenwood and Mott-Ziman methods. The maxima occur at approximately 2000 K at 9000 kg m^{-3}, 5000 K at 1037 kg m^{-3} and 50 kK at 405 kg m^{-3}.

To gain further insight into the origin of metallisation we examine the two factors that limit conductivity: the structure factor and the pseudogap. Structure factors of vdW-DF2 results are shown varying with density at 1000 K (*top* fig. 5.10) and varying with

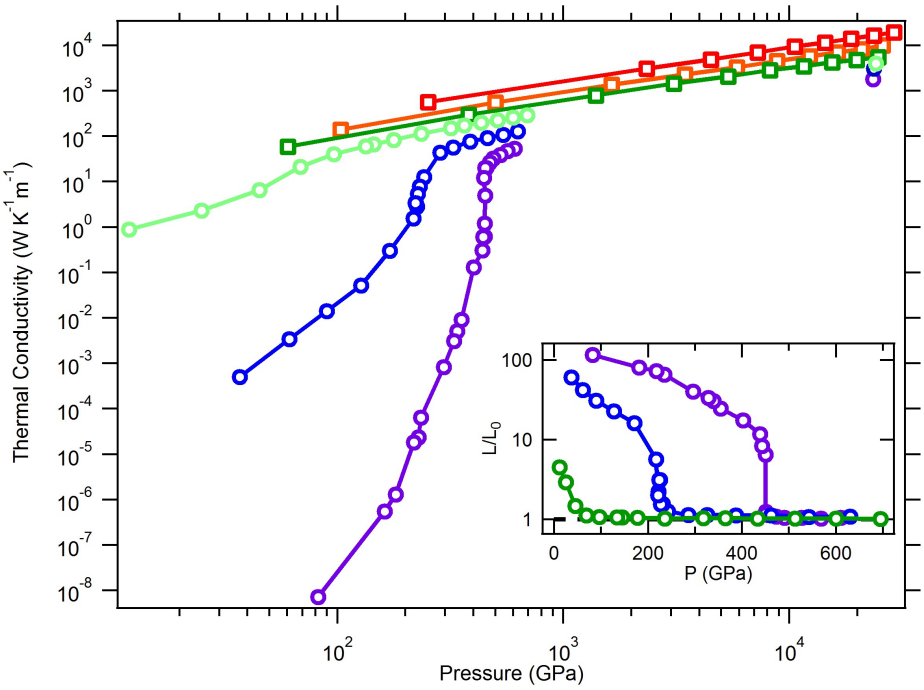

Figure 5.6: Thermal Conductivity as a function of pressure (vdW-DF2). 1000 K (purple), 2000 K (blue), 5000 K (light-green), 10 kK (green), 20 kK (orange) and 50 kK (red). *Inset:* Results of Lorenz number (L/L_0) against pressure, with vdW-DF2, showing differences to the proportionality constant L. The constant value expected of L is marked as a solid black line falling behind 5000 K results.

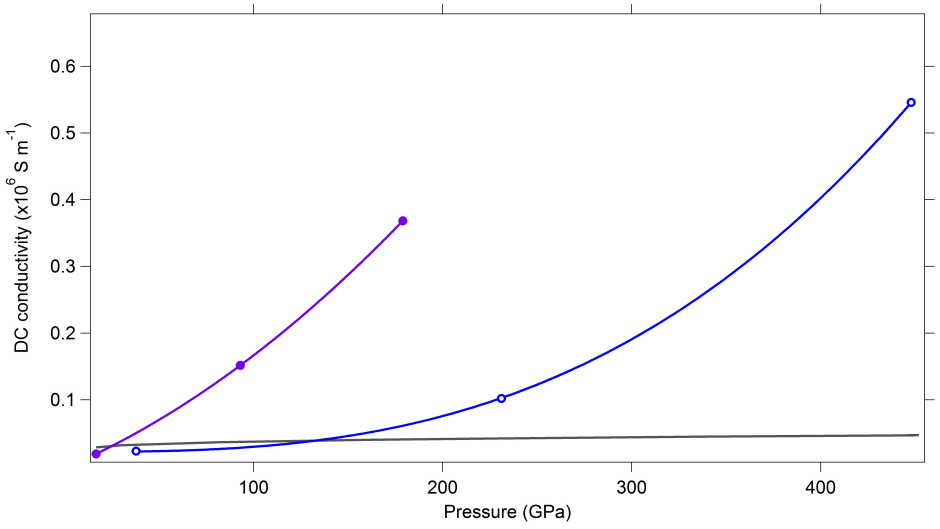

Figure 5.7: DC conductivity at the predicted phase transition at the pressures as in fig. 4.8. Pressure increases with decreasing temperature. Values are interpolated for $\beta = 0.5$ from vdW-DF2 (blue open circles, solid line) and PBE (purple closed circles, solid line). The Mott minimum conductivity is shown as the solid grey line [220].

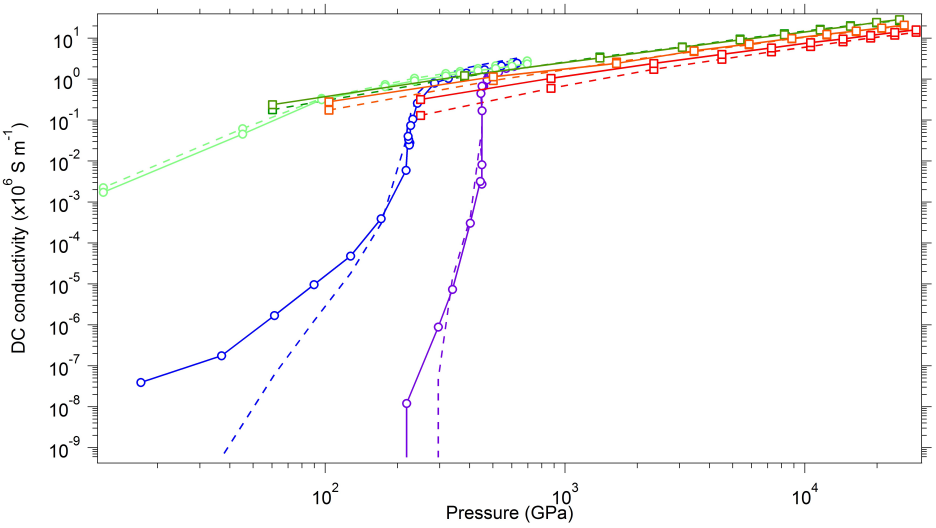

Figure 5.8: DC conductivities as a function of pressure. Showing Mott-Ziman method for comparison to Kubo-Greenwood method. Results are of vdW-DF2 at 1000 K (purple), 2000 K (blue), 5000 K (light-green), 10 kK (green), 20 kK (orange) and 50 kK (red) from the Kubo-Greenwood method (solid lines) and Mott-Ziman method (dashed lines).

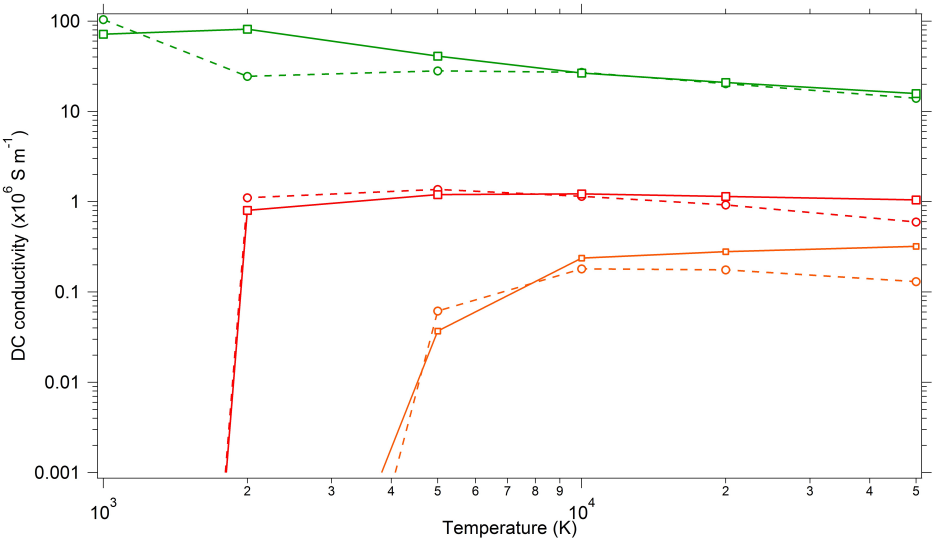

Figure 5.9: Maximum conductivity of hydrogen from the Kubo-Greenwood and Mott-Ziman methods for 9000 kg m^{-3} (green), 1037 kg m^{-3} (red) and 405 kg m^{-3} (orange). Conductivities from the Mott-Ziman method (dashed-lines).

temperature at a constant density of 1037 kg m^3 (*bottom* fig. 5.10) where the density of states at this density is also shown in fig. 5.11. These figures illustrate the contribution to the integral ($2k_F$) of the structure factor (S(q)) in the Mott-Ziman formulation, eq. (3.19), for conductivity, showing the expected increase with temperature and density up to 5000 K and the decrease in conductivity from 10 - 50 kK. Also shown in fig. 5.11 (*inset*) is the g factor as in eq. (3.21) showing the influence of the pseudogap on the non interacting conductivity.

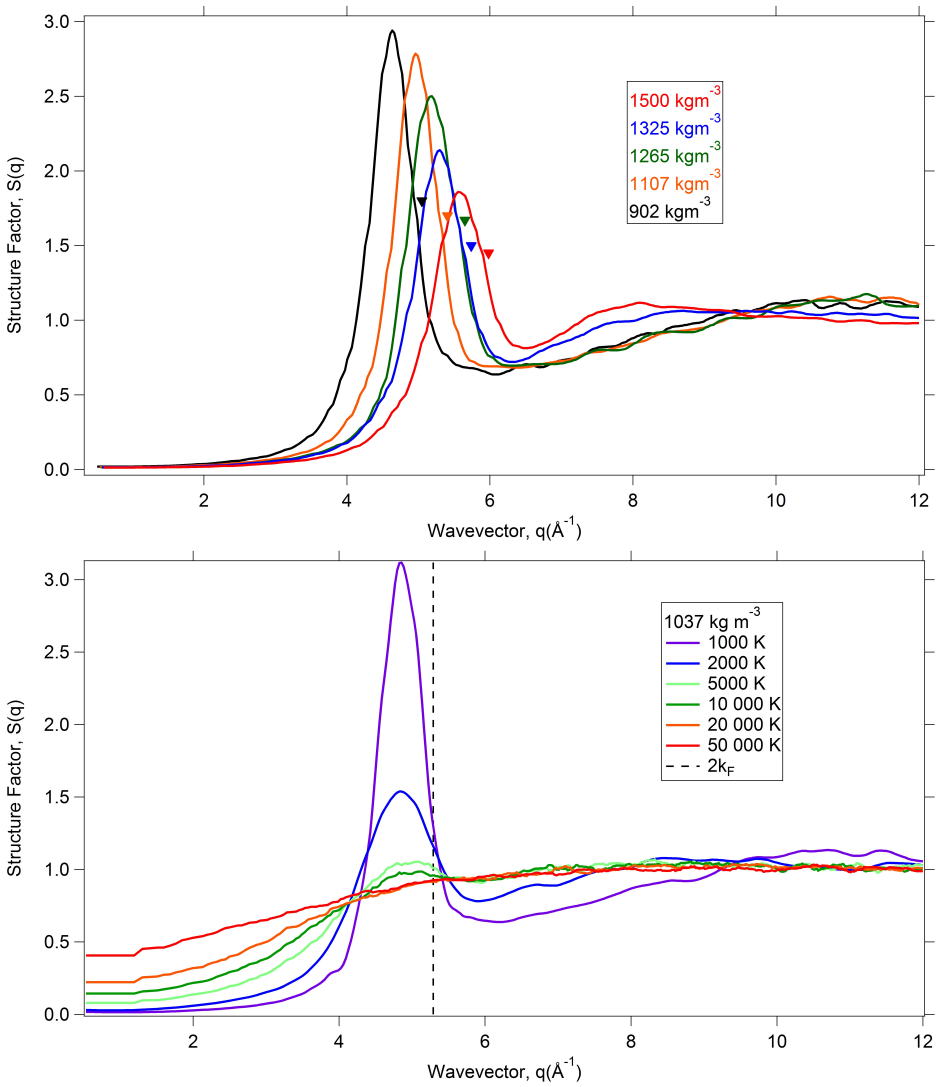

Figure 5.10: Structure Factors of hydrogen. *top:* 1000 K vdW-DF2 structure factor evolution through densities as in figure 4.6. Triangles mark location of $2k_F$ for evaluation of conductivity from the Mott-Ziman formalism as in equation (3.19). *Bottom:* Structure factor dependence with temperatures 1000 K - 50 kK at the density 1037 kg m^{-3} where the dashed line marks the $2k_F$ location.

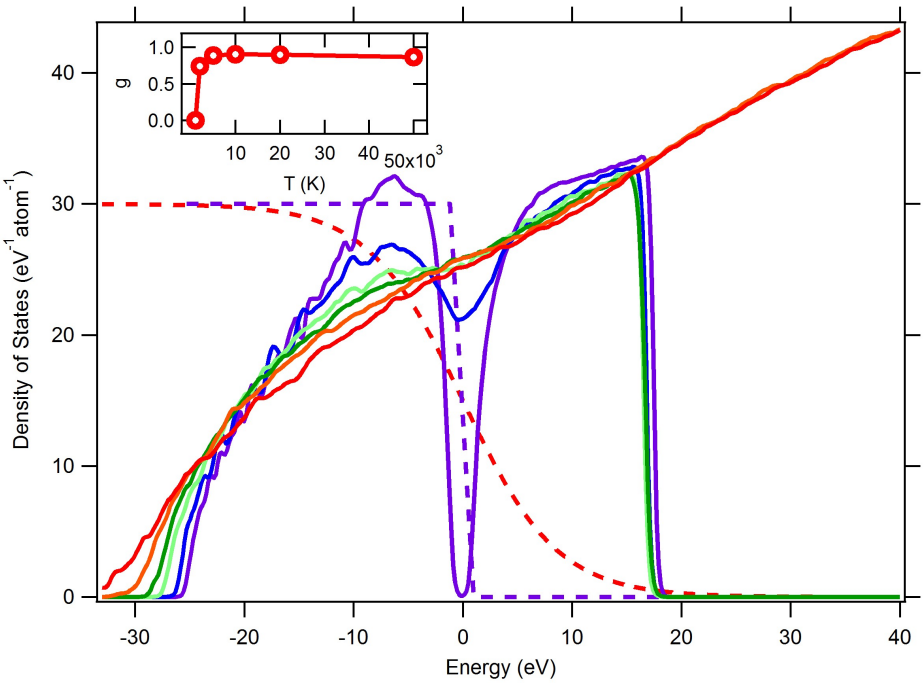

Figure 5.11: Density of States of hydrogen at the Fermi level of ρ =1037 kg m^{-3} at all temperatures. Colours referring to temperatures as in *bottom* fig. 5.10. Fermi-Dirac distributions are shown for 1000 K and 50 kK (dashed lines). *Inset:* g factor from the Mott-Ziman formula eq. (3.21) for this density.

5.3 Discussion and Conclusions

Anomalies in transport properties closely follow the Widom line defined by anomalies in thermodynamic properties. Therefore the Widom line is not only defined by the thermodynamics of the system but also the underlying atomic structure and dynamics. Supercritical anomalies in the dynamics mark the Frenkel line. The Frenkel line and Widom line are not coincident in general. However in hydrogen they are providing a remarkably clear connection between the dynamical properties and underlying microscopic processes.

VdW-DF2 partially corrects the band gap problem in DFT as shown by better agreement with experimental Hugoniot conductivity, where PBE is shown to over-estimate the conductivities particularly at low values of conductivity and reflectivity (figs. 5.3 and 5.5). This overestimation is also shown in the dissociation fraction conductivities where vdW-DF2 predicts a lower conductivity at equal pressures. VdW-DF2 shows a smaller conductivity than PBE when compared at similar structural states, i.e. half dissociation (fig. 5.7).

The conductivity from the Mott-Ziman method is in remarkably good agreement with the Kubo-Greenwood method (fig. 5.8). The agreement points towards the ionic structure playing a significant role in electron transport.

Analysis of the structure shows it's importance in the description of the conductivity. From the structure factor in fig. 5.10 it is clear that the increase in conductivity with temperature is initially expected due to the initial decrease in scattering associated with the decrease in the first peak in the structure factor. Diminished scattering also lifts the pseudogap (fig. 5.11). The pseudogap is shown to sharply vanish with increasing temperature.

The conductivity decreases with increasing temperature, at high temperature. This is due to changes in the structure factor as the area involved in the Mott-Ziman calculation is shown (fig. 5.10) to increase, as after the peak disappears the low wavevector (q) structure begins to increase and would increase scattering and hence decrease the conductivity.

Chapter 6

Planetary Applications of Hydrogen Helium Simulations

I perform ab initio molecular dynamics simulations of hydrogen-helium fluids giving insight into giant planetary interiors. Addition of helium increases the pressure-temperature range over which H_2 molecules are stable. The molecular to atomic transition is shifted to higher pressure as compared with pure hydrogen, as are anomalies in the heat capacity, Grüneisen parameter, self-diffusion coefficient, and electrical conductivity that are associated with the transition. Simulations in the NPT ensemble with varying helium number fractions show that vdW-DF2 predicts much lower de-mixing temperatures than PBE, predicting complete solubility throughout the interiors of Jupiter and Saturn contrary to recent PBE results [115].

6.1 Introduction

The modelling of gas giant interiors requires accurate equation of state data: results are sensitive to small uncertainties [6]. Correctly modelling the interior of Jupiter and Saturn

with constraints set by observation (with more in the near future from the upcoming NASA *Juno* mission) will become more challenging. This requires a more accurate equation of state and will lead to a better understanding of the interior structure, evolution and origin. An increased accuracy in available results for hydrogen and helium will lead to improved models, which in turn will lead to improved understanding of internal fluid dynamics, magnetic field generation, the evolution of the planet [112] and the size or even the existence of a rocky core [221, 222].

Jupiter and Saturn are generally accepted to have been formed at the same time as the Sun, being composed equally from the surrounding molecular cloud constituents [223]. A large number of gas giant exoplanets have been discovered through ever improving observational techniques [224]. This has sparked new found interest in high pressure hydrogen and helium to better understand these exoplanets, ranging from Jupiter like in mass (M_J) to much larger $\sim 10\, M_J$.

The interesting problem with current understanding is that Saturn and Jupiter both have an excess in luminosity, where they emit more heat than which they receive from the Sun. One possible explanation for this excess is release of latent heat by the fall of helium under gravity as it de-mixes from the hydrogen interior, termed helium rain. This feature requires that the helium become immiscible in hydrogen at the extreme conditions present. Recent PBE simulations in the NVT ensemble using thermodynamic integration to obtain non-ideal entropies have placed helium de-mixing within the outer region of the interior of Saturn [115]. Differences in de-mixing temperatures depend on theoretical methods implemented where Pfaffenzeller *et al.* [114] using structural minimisation, find systematically lower de-mixing temperatures and Lorenzen *et al.* [225] using PBE, with ideal entropy of mixing, show similar results to those of Morales *et al.* [115], who used full thermodynamic integration within PBE.

6.2 Methods

Simulations are conducted with vdW-DF2 and PBE. I carry out simulations as in previous chapters but with the inclusion of helium to the cell at the primordial composition where $X_{He} = 0.09$ is the helium number fraction giving 934 hydrogen and 90 helium atoms (1024 atoms in total). In starting the hydrogen-helium (H-He) simulations I take the final snap shot from a pure hydrogen system and make a random selection of 90 particles to be helium particles. I compare properties to the pure hydrogen system. Properties calculated are as before with the electrical conductivity being calculated from the Kubo-Greenwood formula. The equation of state is obtained in the NVT ensemble through Born-Oppenheimer Molecular Dynamic (MD) simulations which give the pressure and internal energy at given density and temperature. NVT settings are as per the pure hydrogen case using a Nosé-Hoover thermostat.

I also conduct NPT ensemble calculations, with vdW-DF2, for a range of hydrogen-helium fractions at 1000 GPa and temperatures of 5000 K and 10 kK. NPT simulations are performed with a total of 1024 atoms but with varying X_{He} from 0.0 (pure hydrogen) to 1.0 (pure helium). Settings used for NPT ensemble simulations are identical to that used for the NVT ensemble simulations with a plane wave cut-off energy equal to 1200 eV, a value of 1×10^{-6} eV as the break condition in the electronic self-consistency loop and a sampling of the Brillouin zone at zero wave vector ($k = 0$, Γ point). For NPT simulations the inclusion of the Souza-Martins barostat as implemented by Hernandez [171, 172] with a fictitious mass of 1×10^{-4} amu where the Nosé-Poincaré thermostat of Bond *et al.* [173] is used.

From the NPT results I calculate the Gibbs energy of mixing ($\Delta G = \Delta H - T\Delta S$) and estimate the de-mixing temperature when hydrogen and helium become immiscible to see whether helium rainout occurs within the interiors of Jupiter and Saturn. Entropy, S, is calculated in the ideal mixing limit as $\Delta S^{LM}(x) = x\ln x + (1-x)\ln(1-x)$, where x is the helium number fraction.

The isentrope is calculated via eq. (3.34) from the Grüneisen parameter (γ) giving the temperature through a series of densities. With this, comparisons are made to previous estimates of the Jovian isentrope. For Jovian interiors the initial condition is taken as a pressure of 1 bar, a temperature of 170 K [12, 226], a primordial helium abundance and an initial density of 0.164 kg m^{-3}. Also I calculate the Saturnian isentrope from an initial temperature of 134 K [227] and a density of 0.21 kg m^{-3} at 1 bar pressure. Jupiter contains a helium abundance by mass of $Y_{He} = 0.231$ as reported from the Galileo entry probe [228]. For both planets I have chosen a primordial value as to apply to a more general giant exoplanet, using a value of $Y_{He} = 0.278$ by mass [3].

6.3 Results

The full equation of state, as calculated with vdW-DF2, is shown for the primordial H-He mixture in fig. 6.1. Pressure is shown to increase with increasing density and temperature. An increase in pressure is seen at 2000 K from PBE to vdW-DF2. The differences in functional used are negligible at 10 kK and above.

Comparison of pure hydrogen and the primordial H-He mixture at 1000 K (fig. 6.2) shows that when helium is added to hydrogen the first-order phase transition is washed out. A higher order anomaly remains (change in compressibility) and this is shifted to higher pressures in H-He.

Comparisons are made at 2000 K in fig. 6.3 showing vdW-DF2 and PBE for pure hydrogen, primordial H-He mixture and pure helium simulations. VdW-DF2 systematically predicts higher pressures than PBE in the H-He mixture. For pure helium, vdW-DF2 and PBE yield identical results.

Dissociation of H-H in the primordial fraction H-He mixture simulations are shown in fig. 6.4. Hydrogen in the H-He mixtures remains in the molecular phase to larger densities relative to the hydrogen dissociation in pure hydrogen. The influence of helium on the

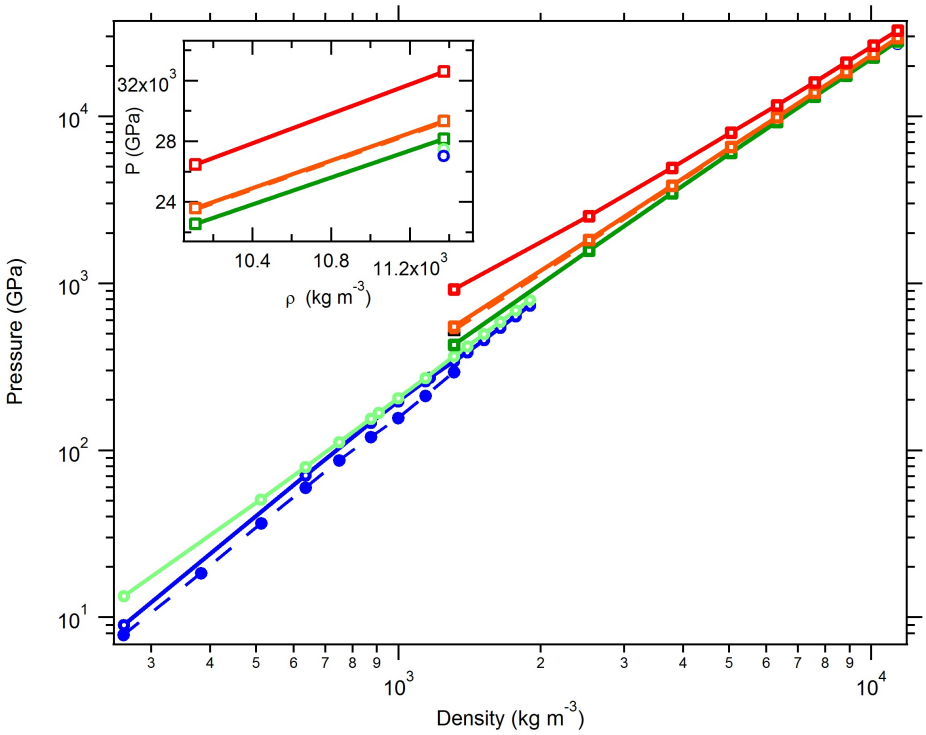

Figure 6.1: H-He mixture of 0.09 helium number fraction. VdW-DF2 (open circles, solid lines) pressures of 2000 K (blue), 5000 K (light-green), 10 kK (green), 20 kK (orange) and 50 kK (red). For comparison PBE H-He (dashed lines) simulations at 2000 K (blue closed circles, dashed lines) and 20 kK (orange closed squares, dashed line). *Inset:* Pressures at the highest density simulated showing ρ =11 373 kg m^{-3} at the lower temperatures of 2000 K and 5000 K for vdW-DF2 (open circles). The other results are as in main plot.

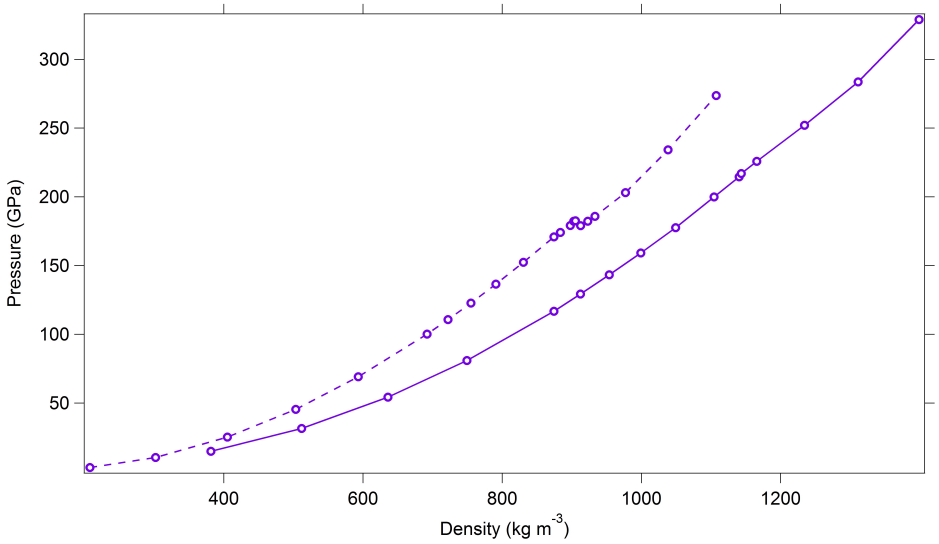

Figure 6.2: 1000 K PBE pure hydrogen (purple dashed line, open circles) and H-He mixture of 0.09 helium number fraction (purple solid line, open circles).

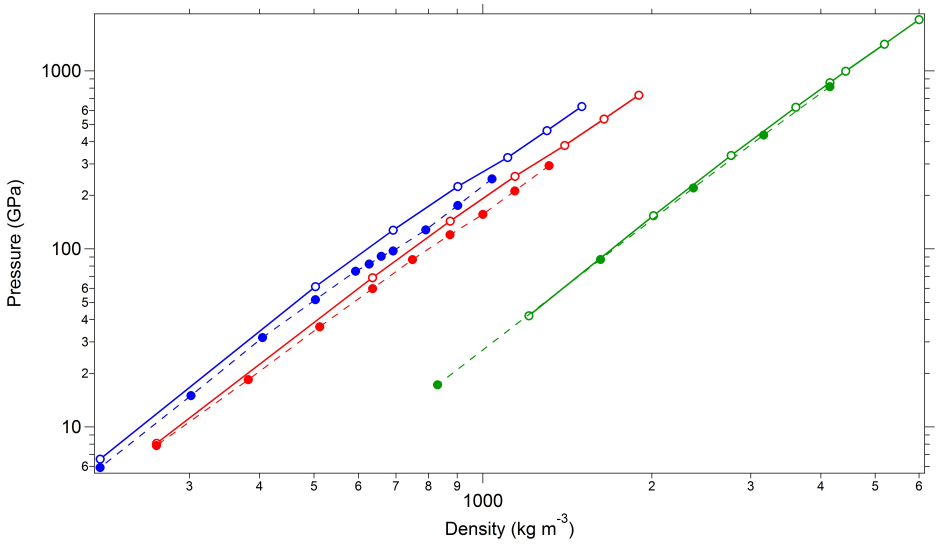

Figure 6.3: Pressure density at 2000 K. Results are of vdW-DF2 (open circles) and PBE (closed circles). Pure H (blue), H-He at 0.09 helium number fraction (red) and pure He (green).

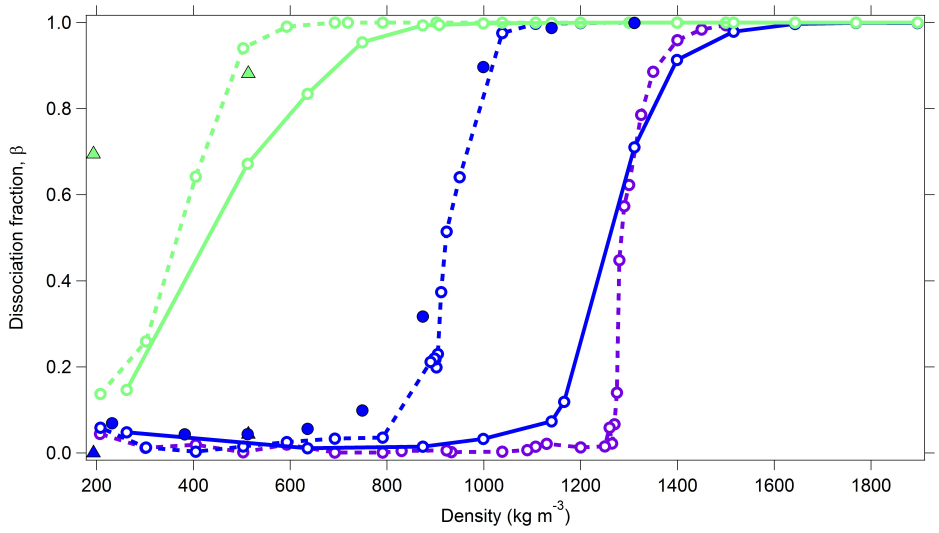

Figure 6.4: H-H dissociation fraction from H-He simulations at 0.09 helium number fraction. Temperatures shown of 2000 K (blue) and 5000 K (light-green). Open circles with solid lines are vdW-DF2, and closed circles are PBE (2000 K). Also shown for comparison is the vdW-DF2 pure hydrogen (open circles, dashed lines) dissociation along 1000 K (purple), 2000 K (blue) and 5000 K (light-green). Dissociation fraction using the bond life time method with PBE using 64 hydrogen and 64 helium ($X_{He} = 0.5$) atoms of Vorberger *et al.* [91] are shown as closed triangles for 5000 K and 2000 K.

location of the dissociation lessens on heating and has nearly vanished by 5000 K. PBE predicts dissociation at lower density than vdW-DF2.

The radial distribution function also shows the influence of helium on the H_2 molecular fraction (fig. 6.5). The H-H radial distribution function shows that hydrogen becomes increasingly molecular with increasing helium fraction. VdW-DF2 predicts greater molecular fraction than PBE at similar pressure, temperature and composition.

The molecular to atomic transition (fig. 6.6) occurs at higher pressure in the H-He primordial mixture as compared with pure hydrogen for the vdW-DF2 functional at all temperatures. The difference is minimal at 5000 K close to where giant planetary isentropes cross the structural transition.

The heat capacity (C_V), (fig. 6.7) also reflects the shift of the phase transition from pure hydrogen to H-He primordial mixture simulations. The effects of the phase transition are seen up to the 5000 K with a small discontinuity at a density of ρ ~636 kg m^{-3}. Heat capacity at higher temperatures T $\geq$ 10 kK for vdW-DF2 and pure hydrogen of vdW-DF2 are very similar, showing that helium has little effect on the heat capacity. Previous results from French *et al.* show a value of the heat capacity that is systematically lower than mine. The difference cannot be attributed to the exchange-correlation functional (vdW-DF2 vs PBE) I note that the difference is comparable to the electronic contribution to C_V and speculate that the contribution was neglected in the earlier results.

The Grüneisen parameter (γ), is shown for vdW-DF2. Small differences between pure hydrogen and primordial H-He are still present at 5000 K (not shown) and are still smaller at higher densities.

Isentropes are shown in fig. 6.8 comparing vdW-DF2 H-He to the Jovian interior modelling of Nettelmann *et al.* [206] where they use PBE for the H-He equation of state. My results show the cooling anomaly associated with the molecular to atomic transition shifted to higher density as compared with PBE. This produces somewhat colder temperatures at

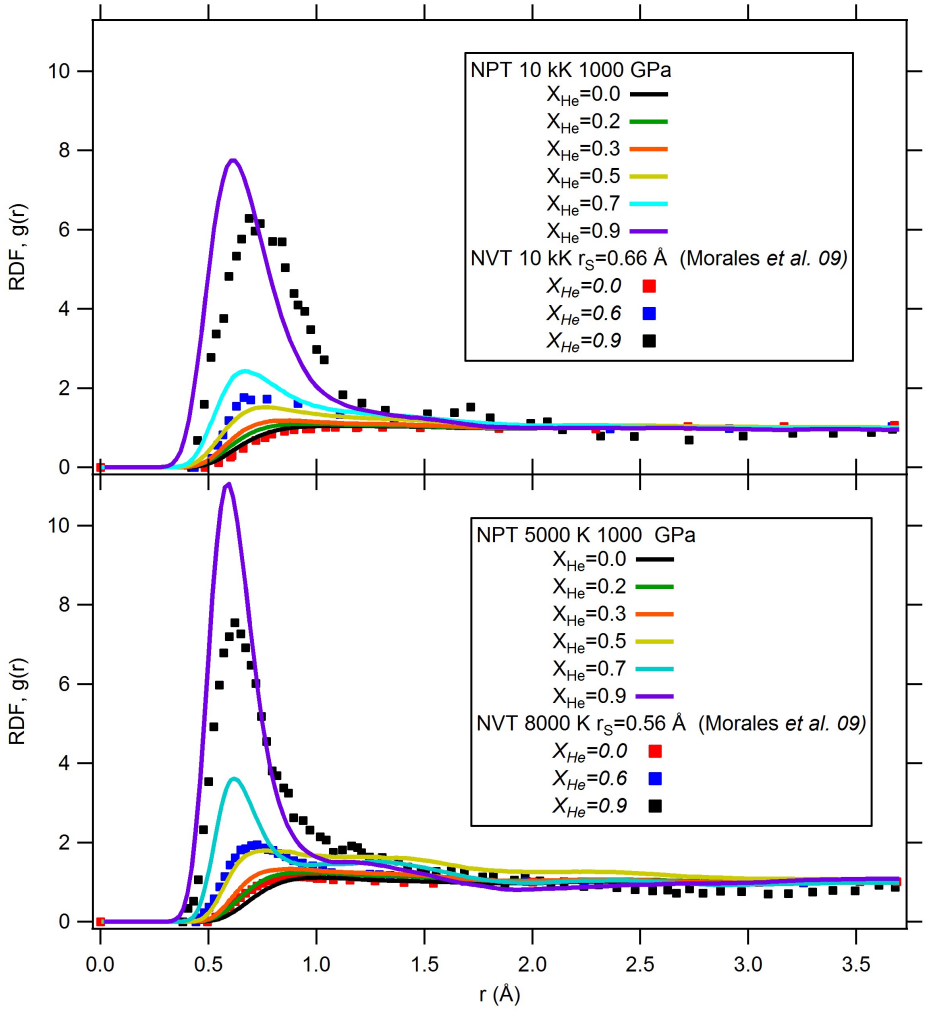

Figure 6.5: H-H radial distribution function against helium number fractions. Results are from vdW-DF2 NPT simulations at 10 kK (*Top figure*) and 5 kK (*Bottom figure*) both at 1000 GPa. H-He fractions shown are 0.9 (purple), 0.7 (light-blue), 0.5 (dark-yellow), 0.3 (orange), 0.2 (green) and 0.0 (black). Morales *et al.* [115] PBE NVT simulations are shown at 10 kK and electronic density $r_S = 0.66$ Å (*Top figure*) and at 8 kK and $r_s = 0.56$ Å (*Bottom figure*) as squares for helium number fraction 0.9 (black), 0.6 (blue) and 0.0 (red).

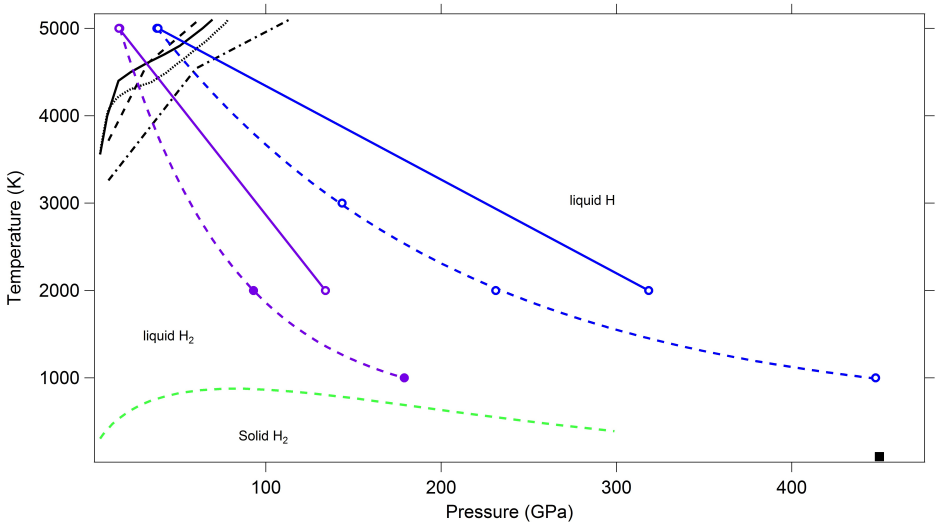

Figure 6.6: H-He at 0.09 helium number fraction mixture pressure and temperature at half dissociation fraction. Results are of vdW-DF2 (blue open circles, solid lines) and PBE (purple open circles, solid lines) where lines are a guide to the eye. Pure hydrogen results as in fig. 4.8 are shown for vdW-DF2 (blue open circles, dashed lines) and PBE (purple open circles, dashed lines). The solid to liquid melt line of hydrogen as calculated from first principles Bonev *et al.* [78] (light-green dashed line) and the solid hydrogen extrapolated band gap closure in diamond anvil cell experiments of Loubeyre *et al.* [2] (black square). Jovian isentropes are from French *et al.* [205] (black solid line), Nettelmann *et al.* [206] (black dotted line) and as shown in Bagenal *et al.* [12] both the Jovian isentrope (black dashed line) and the Saturnian isentrope (black dashed-dotted line).

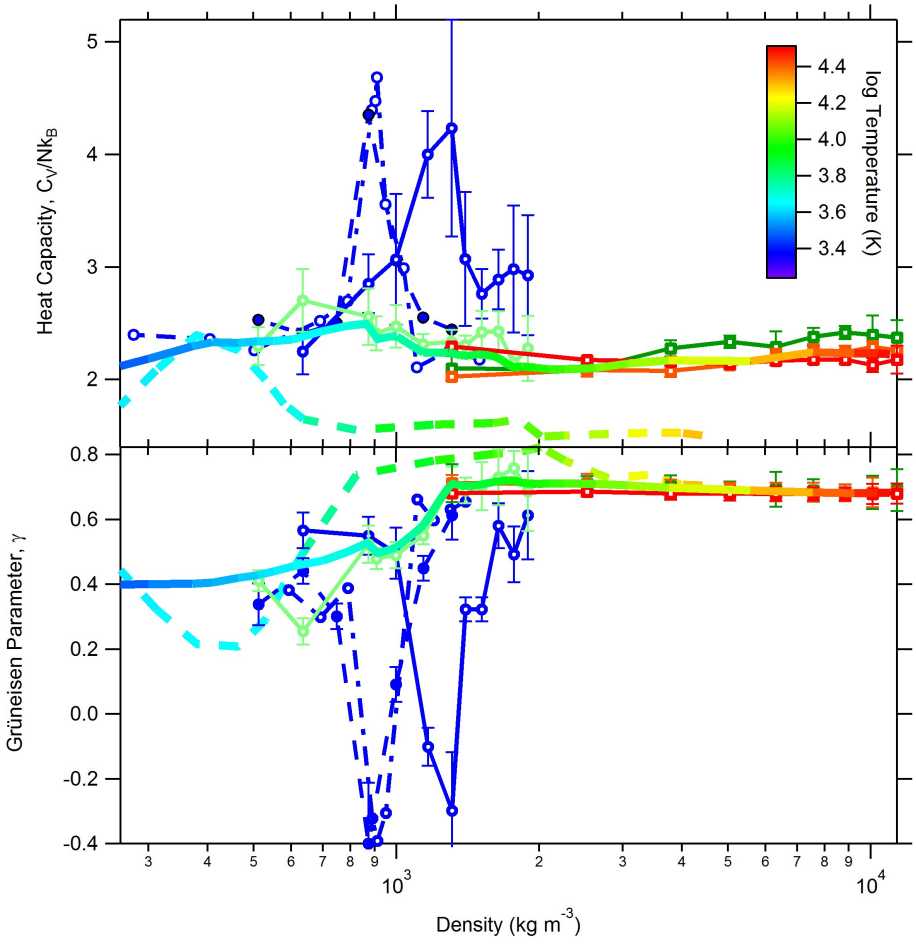

Figure 6.7: Top panel: H-He Heat capacity (C_V/NK_B), bottom panel: H-He Grüneisen parameter both as a function of density and of $X_{He} = 0.09$. Results are shown from the fluctuation method: vdW-DF2 H-He (solid lines, open symbols) and PBE H-He for 2000 K (blue closed circles,dashed line). Results are shown of pure hydrogen vdW-DF2 (blue open circles, dash-dotted line) at 2000 K. Jovian Isentropes are from vdW-DF2 (solid multicoloured line indicating temperature as in scale) and PBE results of French *et al.* [205] (dashed multicoloured line indicating temperatures as in scale).

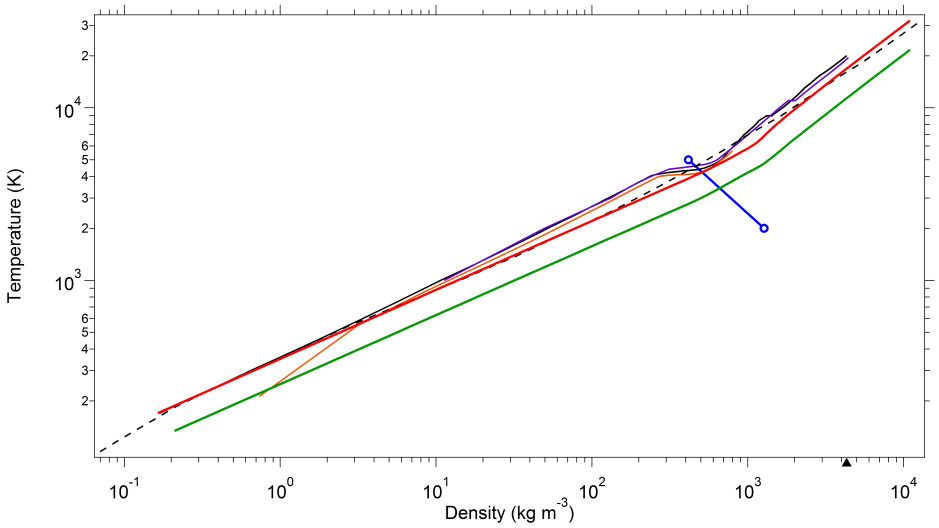

Figure 6.8: Temperature against density of gas giant isentropic trajectories. VdW-DF2 isentrope for H-He Jupiter (red) by using a primordial helium abundance $Y_{He} = 0.278$ giving an initial density of 0.164 kg m^{-3} and a temperature of 170 K at a pressure of 1 bar. Also shown is the Saturnian isentrope (green) with initial conditions of density 0.21 kg m^{-3} at 134 K and 1 bar pressure. Results are shown for the Jovian isentrope from PBE results of Nettelmann *et al.* [206] (black line). Further theoretical results for the Jovian isentrope using PBE French *et al.* [205] (purple line) and Becker *et al.* [229] (orange line) and the chemical model of Saumon *et al.* [62] (dashed black line). The Frenkel line from the $\beta = 0.5$ vdW-DF2 results as in fig. 4.8 are shown (blue open circles). Black arrow on x-axis shows the location of French *et al.* core-mantle boundary.

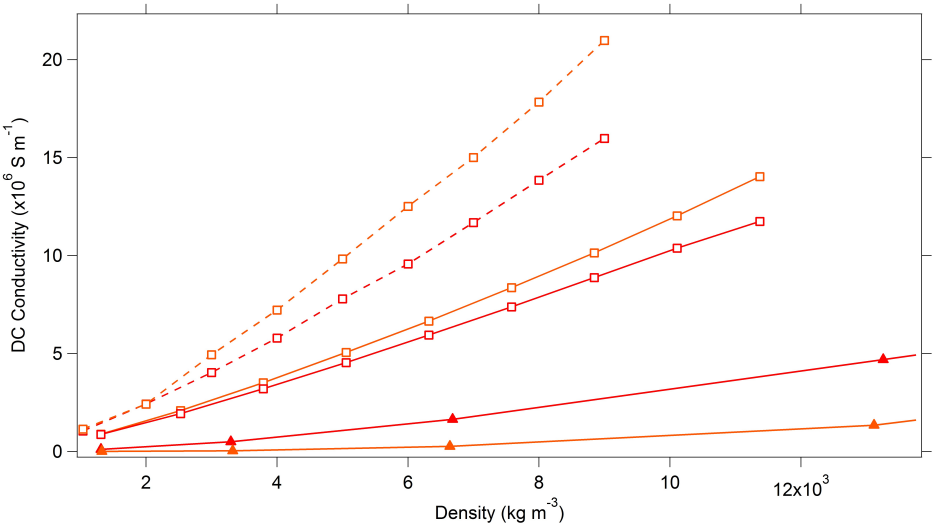

Figure 6.9: DC conductivity comparing pure and mixed ($X_{He} = 0.09$) H-He systems. Conductivities from the Kubo-Greenwood method are shown of 50 kK (red) and 20 kK (orange). VdW-DF2 results are pure hydrogen (open squares, dashed line) and H-He mixture (open squares, solid line). Results of Stixrude *et al.* [59] for pure helium (triangles, solid line) using Mott-Ziman method.

greater depth. Small differences at low density ($\rho < 100$ kg m^{-3}) are due to differing assumptions in the nearly ideal gas regime that lies below that of DFT calculations.

Figure 6.9, shows the comparison of DC conductivities for pure hydrogen, mixed H-He and the pure helium [59] at 20 kK and 50 kK. As expected our H-He mixture values fall in between those of pure hydrogen and pure helium. The dependence of σ on helium fraction is non-linear with a small helium fraction causing a large decrease in σ.

Comparing the vdW-DF2 pure hydrogen and primordial H-He mixture DC conductivities of 2000 - 50 kK in fig. 6.10, results show a shift in the 2000 K onset of metallisation. The electrical conductivity of primordial H-He exceeds the minimum metallic value at very low pressure (50 GPa) along giant planetary isentropes. This pressure corresponds to 90 % at Jupiter's radius: nearly all of the Jovian envelope is metallic. VdW-DF2 conductivities are systematically lower than those of PBE everywhere, due to the larger molecular fraction.

The self-diffusion coefficient of hydrogen in the primordial H-He mixture is smaller than in pure hydrogen (fig. 6.11). This is attributed to the larger effective size of the helium

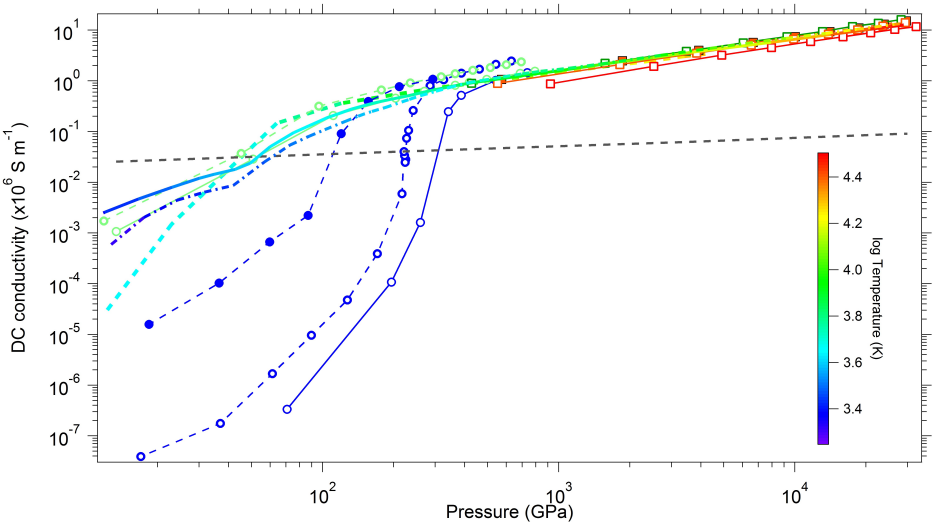

Figure 6.10: H-He mixture ($X_{He} = 0.09$) DC conductivities against pressure. VdW-DF2 H-He (open symbols, solid lines) are shown for 2000 K (blue), 5000 K (light-green), 10 kK (green), 20 kK (orange) and 50 kK (red). Additionally pure hydrogen simulations with vdW-DF2 (open circles, dashed lines) are shown for 2000 K (blue) and 5000 K (light-green). PBE H-He simulations (closed circles, dashed lines) at 2000 K and 20 kK are shown for comparison. Jovian Isentropes are from vdW-DF2 (solid multicoloured line) and PBE results of French *et al.* [205] (dashed multicoloured line). Also shown is the vdW-DF2 Saturnian isentrope (dashed-dotted multicoloured line). All isentropes are coloured by temperature as in scale. The Mott minimum conductivity is shown as the solid grey line [220].

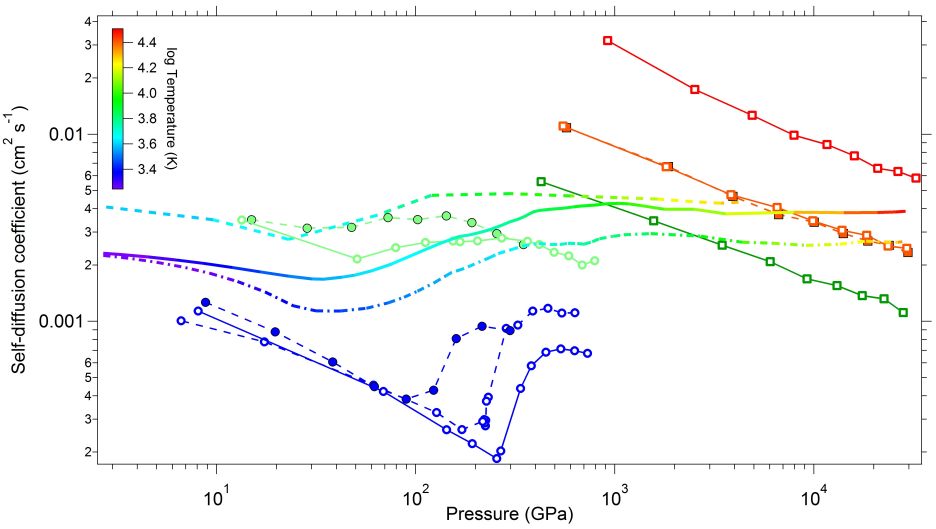

Figure 6.11: Self-Diffusion coefficient of hydrogen in H-He (X_{He} = 0.09) simulations. VdW-DF2 (open circles and squares) are shown at 2000 K (blue), 5000 K (light-green), 10 kK (green), 20 kK (orange) and 50 kK (red). PBE H-He simulations (dashed lines, closed symbols) for 2000 K, 5000 K and 20 kK and pure H vdW-DF2 at 2000 K (open circles, dashed line) is shown for comparison. Jovian Isentropes are from vdW-DF2 (solid multicoloured line) and PBE results of French *et al.* [205] (dashed multicoloured line). Also shown is the vdW-DF2 Saturnian isentrope (dashed-dotted multicoloured line). All isentropes are coloured by temperature as in scale.

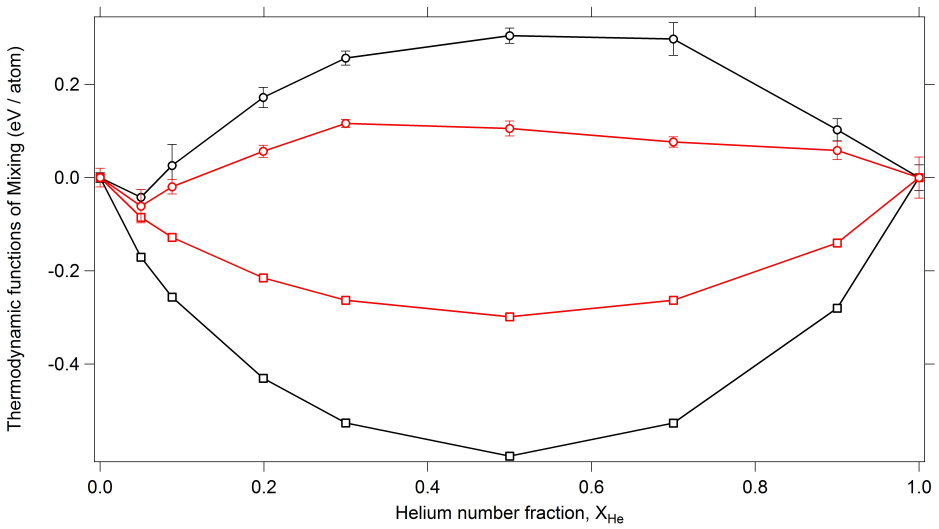

Figure 6.12: Thermodynamic functions of mixing per atom against helium number fraction. Results are for 5000 K (red) and 10 kK (black). Enthalpy of mixing from NPT ensemble simulations (open circles, solid lines) at a pressure of 1000 GPa. The ideal entropy of mixing (TS) for both temperatures (open squares, solid lines).

atoms, reducing the free volume available for diffusive motion. VdW-DF2 produces smaller self-diffusion coefficients as compared with PBE, although the difference is large only in the vicinity of the structural transition.

The enthalpy of mixing increases with increasing temperature (fig. 6.12). The enthalpy of mixing is positive except at very low helium fractions.

The Gibbs energy of mixing ΔG is shown in fig. 6.13. Results show the Gibbs energy of mixing at 5000 K reported in Morales *et al.* giving all positive values where vdW-DF2 Gibbs energies at 5000 K still show negative values indicating H-He solutions are energetically more favourable in vdW-DF2 as compared with PBE.

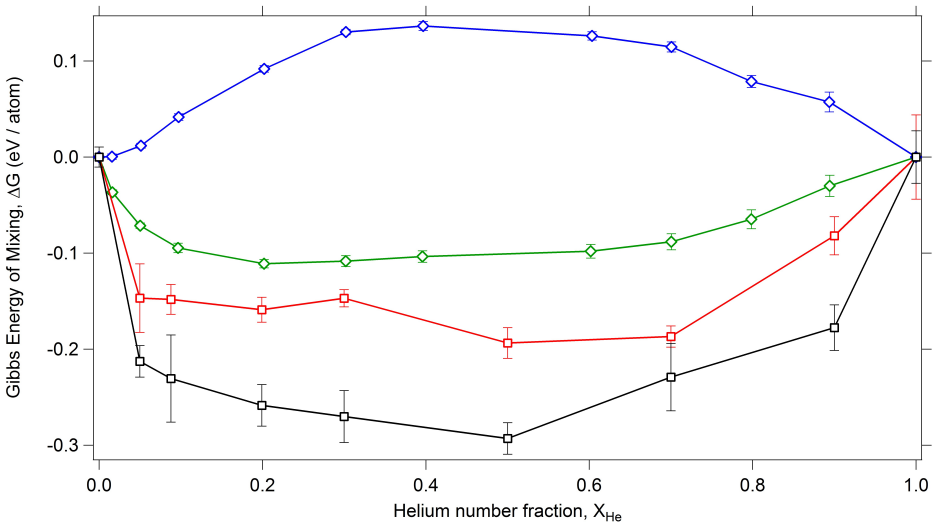

Figure 6.13: Gibbs energy per atom against helium number fraction ($X_{He} = 0.09$). 5000 K (red) and 10 kK (black). Results are shown for the Gibbs energy calculated with NPT vdW-DF2 ΔH results and using the ideal entropy (open squares, solid lines) at P = 1000 GPa. NVT ensemble results are shown Morales *et al.* [115] using PBE (open diamonds, solid lines) for temperatures 5000 K (blue) and 10 kK (green) both at a pressure of P = 1000 GPa.

6.4 Discussion and conclusions

Hydrogen is seen to become more molecular with the inclusion of helium as shown in the partial radial distribution functions in fig. 6.5 and by the shift in the phase transition to higher densities in the dissociation fraction (fig. 6.4). This effect is greater for vdW-DF2 over PBE due to the preferred molecular state in vdW-DF2 for the hydrogen ions. The partial radial distribution functions in fig. 6.5 also show helium making the H-H pair more molecular-like with increasing helium number fraction. This effect is shown to be greater for vdW-DF2 over PBE [115] as vdW-DF2 favours molecular hydrogen. Helium making hydrogen more molecular is also shown in the Gibbs energy results. Where this is shown to persist to higher temperatures. Consequences of the increased molecular nature in hydrogen, from the vdW-DF2 functional, is the onset of conductivity in Jovian planets at greater depths relative to that predicted by PBE results. Other effects are that isentropes will be cooler and interiors are more dense than previously thought, indicating the requirement of smaller core masses for matching observations when modelling interiors.

Recently Gonzalez-Cataldo *et al.* [230] has shown that minor constituents of gas giant planets (MgO, SiO_2, Fe etc.) dissolve in hydrogen at pressure-temperature conditions typical of the bottom of giant planetary envelopes. This presents the possibility that for initially formed rocky cores, when the envelope is formed (from gravitational capture) the core has been dissolving into the envelope ever since. Estimations can be made for the core erosion from the primordial core radius, assuming that this process is diffusion limited, using the diffusion length, $L = \sqrt{Dt}$, where L is the depth of erosion, D is the self-diffusion at the core-envelope boundary and t is the time from the planets formation (t=4.5 Gyr). From vdW-DF2 using a core temperature at 20 kK for Jupiter where self-diffusion is 3.8×10^{-3} cm^2 s^{-1} giving an erosion depth of $L = 233$ km. Assuming a core mass of 10 Earth masses, the diffusion length corresponds to approximately 1 Earth mass dissolved into the envelope.

NPT ensemble simulations of the Gibbs energy of mixing shown in fig. 6.13, using vdW-

DF2, show significant differences to the PBE simulations of Morales *et al.* [115]. VdW-DF2 results show helium to be soluble in hydrogen to lower temperatures due to values being negative for all X_{He} with one minimum. Results of the Gibbs energy show no evidence for H-He phase separation within the interiors of Jupiter or Saturn. I attribute the difference between vdW-DF2 and PBE results to be structure: vdW-DF2 stabilises molecules which have a similar effective size to helium allowing for more energetically favourable mixing.

Chapter 7

Conclusions

From all thermodynamic and transport properties we see the existence of the molecular to atomic phase transition from 1000 K being first-order with the critical point between 2000 K and 1000 K. The phase transition is seen to persist to higher temperatures as defined by Widom and Frenkel lines up to at least 5000 K where anomalies are still seen in the heat capacity and the Grüneisen parameter.

The inclusion of helium with hydrogen at 0.09 number fraction allows for more appropriate predictions on gas giant interiors due to their interiors containing a small fraction of helium approximately of primordial composition. This small amount of helium is shown to have significant effects on the location of the phase transition and on various thermodynamic and transport properties. I have shown the importance of using the vdW-DF2 functional due to improved agreement with experiment in conductivity and reflectivity. The vdW-DF2 functional shows a shift to higher densities of the phase transition at all temperatures where the transition exists as compared with PBE. The functional is shown to favour the molecular state. Contrary to results using PBE [115] predicting de-mixing to occur within the Jovian interior, the vdW-DF2 results show helium to be soluble throughout the Jovian and Saturnian interiors as helium is more soluble with molecular hydrogen likely due to comparable radii.

Appendix A

Acknowledgements

I would like to thank my supervisors Lars Stixrude and Dario Alfé for all the great enthusiasm in science and unlimited wealth of knowledge. I would also like to thank Roberto Scipioni, Eero Holmström and Carlos Pinilla Castellanos for their invaluable support. Ever since I was a child I have been interested in the gas giants in our solar system. This project, allowing me to study the physics of their interiors, has made a dream come true. At this point I would like to thank my family for always being supportive and my friends for all the many laughs.

This work was funded by Science & Technology Facilities Council (STFC). This work used the ARCHER UK National Supercomputing Service (http://www.archer.ac.uk). Also the facilities of HECToR, the UK's national high-performance computing service, which is provided by UoE HPCx Ltd at the University of Edinburgh, Cray Inc and NAG Ltd, and funded by the Office of Science and Technology through EPSRC's High End Computing Programme. Also the IRIDIS High Performance Computing Facility provided by the Science & Engineering South (SES) Centre for Innovation. The Centre is formed by the University of Oxford, Southampton, Bristol and University College London. Finally, the UCL Legion High Performance Computing Facility (Legion@UCL), and associated support services, in the completion of this work.

Bibliography

[1] I. Baraffe, G. Chabrier, and T. Barman, "The physical properties of extra-solar planets," *Reports on Progress in Physics*, vol. 73, no. 1, pp. 1–30, 2010.

[2] P. Loubeyre, F. Occelli, and R. LeToullec, "Optical studies of solid hydrogen to 320 GPa and evidence for black hydrogen," *Nature*, vol. 416, no. 6881, pp. 613–617, 2002.

[3] J. N. Bahcall and M. H. Pinsonneault, "Solar models with helium and heavy-element diffusion," *Reviews of Modern Physics*, vol. 67, no. 4, pp. 781–808, 1995.

[4] U. von Zahn, D. M. Hunten, and G. Lehmacher, "Helium in Jupiter's atmosphere: Results from the Galileo probe helium interferometer experiment," *Journal of Geophysical Research-Planets*, vol. 103, no. E10, pp. 22815–22829, 1998.

[5] B. J. Conrath and D. Gautier, "Saturn helium abundance: A reanalysis of voyager measurements," *Icarus*, vol. 144, no. 1, pp. 124–134, 2000.

[6] D. Saumon and T. Guillot, "Shock compression of deuterium and the interiors of Jupiter and Saturn," *Astrophysical Journal*, vol. 609, no. 2, pp. 1170–1180, 2004.

[7] T. Guillot, "A comparison of the interiors of Jupiter and Saturn," *Planetary and Space Science*, vol. 47, no. 10-11, pp. 1183–1200, 1999.

[8] G. I. Kerley, "Structures of the planets Jupiter and Saturn," *Kerley Technical Services Research Report KTS04-2*, 2004.

[9] N. Nettelmann, B. Holst, A. Kietzmann, M. French, R. Redmer, and D. Blaschke, "Ab initio equation of state data for hydrogen, helium, and water and the internal structure of Jupiter," *Astrophysical Journal*, vol. 683, no. 2, pp. 1217–1228, 2008.

[10] B. Militzer, W. B. Hubbard, J. Vorberger, I. Tamblyn, and S. A. Bonev, "A massive core in Jupiter predicted from first-principles simulations," *Astrophysical Journal Letters*, vol. 688, no. 1, pp. L45–L48, 2008.

[11] N. Nettelmann, "Predictions on the core mass of Jupiter and of giant planets in general," *Astrophysics and Space Science*, vol. 336, no. 1, pp. 47–51, 2011.

[12] F. Bagenal, T. Dowling, and W. McKinnon, *Jupiter, The Planets, Satellites and Magnetosphere.* Cambridge University Press, 2004.

[13] R. Smolucho, "Internal structure and energy emission of Jupiter," *Nature*, vol. 215, no. 5102, pp. 691–695, 1967.

[14] D. J. Stevenson, "Thermodynamics and phase separation of dense fully ionized hydrogen-helium fluid mixtures," *Physical Review B*, vol. 12, no. 10, pp. 3999–4007, 1975.

[15] D. J. Stevenson and E. E. Salpeter, "Dynamics and helium distribution in hydrogen-helium fluid planets," *Astrophysical Journal Supplement Series*, vol. 35, no. 2, pp. 239–261, 1977.

[16] D. J. Stevenson and E. E. Salpeter, "Phase-diagram and transport properties for hydrogen-helium fluid planets," *Astrophysical Journal Supplement Series*, vol. 35, no. 2, pp. 221–237, 1977.

[17] W. B. Hubbard, T. Guillot, M. S. Marley, A. Burrows, J. I. Lunine, and D. S. Saumon, "Comparative evolution of Jupiter and Saturn," *Planetary and Space Science*, vol. 47, no. 10-11, pp. 1175–1182, 1999.

[18] J. B. Pollack, O. Hubickyj, P. Bodenheimer, J. J. Lissauer, M. Podolak, and Y. Greenzweig, "Formation of the giant planets by concurrent accretion of solids and gas," *Icarus*, vol. 124, no. 1, pp. 62–85, 1996.

[19] S. T. Weir, A. C. Mitchell, and W. J. Nellis, "Metallization of fluid molecular hydrogen at 140 GPa (1.4 Mbar)," *Physical Review Letters*, vol. 76, no. 11, pp. 1860–1863, 1996.

[20] W. J. Nellis, S. T. Weir, and A. C. Mitchell, "Metallization of fluid hydrogen at 140 GPa (1.4 Mbar) by shock compression," *Shock Waves*, vol. 9, no. 5, pp. 301–305, 1999.

[21] S. I. Belov, G. V. Boriskov, A. I. Bykov, R. I. Il'kaev, N. B. Luk'yanov, A. Y. Matveev, O. L. Mikhailova, V. D. Selemir, G. V. Simakov, R. F. Trunin, I. P. Trusov, V. D. Urlin, V. E. Fortov, and A. N. Shuikin, "Shock compression of solid deuterium," *JETP Letters*, vol. 76, no. 7, pp. 433–435, 2002.

[22] P. Loubeyre, P. M. Celliers, D. G. Hicks, E. Henry, A. Dewaele, J. Pasley, J. Eggert, M. Koenig, F. Occelli, K. M. Lee, R. Jeanloz, D. Neely, A. Benuzzi-Mounaix, D. Bradley, M. Bastea, S. Moon, and G. W. Collins, "Coupling static and dynamic compressions: First measurements in dense hydrogen," *High Pressure Research*, vol. 24, no. 1, pp. 25–31, 2004.

[23] M. D. Knudson, D. L. Hanson, J. E. Bailey, C. A. Hall, J. R. Asay, and C. Deeney, "Principal Hugoniot, reverberating wave, and mechanical reshock measurements of liquid deuterium to 400 GPa using plate impact techniques," *Physical Review B*, vol. 69, no. 14, p. 144209, 2004.

[24] V. E. Fortov, R. I. Ilkaev, V. A. Arinin, V. V. Burtzev, V. A. Golubev, I. L. Iosilevskiy, V. V. Khrustalev, A. L. Mikhailov, M. A. Mochalov, V. Y. Ternovoi, and M. V. Zhernokletov, "Phase transition in a strongly nonideal deuterium plasma generated by quasi-isentropical compression at megabar pressures," *Physical Review Letters*, vol. 99, no. 18, p. 185001, 2007.

[25] W. J. Nellis, "Dynamic compression of materials: metallization of fluid hydrogen at high pressures," *Rep. Prog. Phys.*, vol. 69, pp. 1479–1580, 2006.

[26] D. G. Hicks, T. R. Boehly, P. M. Celliers, J. H. Eggert, S. J. Moon, D. D. Meyerhofer, and G. W. Collins, "Laser-driven single shock compression of fluid deuterium from 45 to 220 GPa," *Physical Review B*, vol. 79, no. 1, p. 014112, 2009.

[27] P. M. Celliers, G. W. Collins, D. G. Hicks, and J. H. Eggert, "Systematic uncertainties in shock-wave impedance-match analysis and the high-pressure equation of state of Al," *Journal of Applied Physics*, vol. 98, no. 11, p. 113529, 2005.

[28] P. Loubeyre, S. Brygoo, J. Eggert, P. M. Celliers, D. K. Spaulding, J. R. Rygg, T. R. Boehly, G. W. Collins, and R. Jeanloz, "Extended data set for the equation of state of warm dense hydrogen isotopes," *Physical Review B*, vol. 86, no. 14, p. 144115, 2012.

[29] W. J. Nellis, A. C. Mitchell, P. C. McCandless, D. J. Erskine, and S. T. Weir, "Electronic-energy gap of molecular-hydrogen from electrical-conductivity measurements at high shock pressures," *Physical Review Letters*, vol. 68, no. 19, pp. 2937–2940, 1992.

[30] A. F. Goncharov, E. Gregoryanz, R. J. Hemley, and H.-k. Mao, "Spectroscopic studies of the vibrational and electronic properties of solid hydrogen to 285 GPa," *Proceedings of the National Academy of Sciences*, vol. 98, no. 25, pp. 14234–14237, 2001.

[31] W. J. Nellis, A. C. Mitchell, M. Vanthiel, G. J. Devine, R. J. Trainor, and N. Brown, "Equation-of-state data for molecular-hydrogen and deuterium at shock pressures in the range 2-76 GPa (20-760 kbar)," *Journal of Chemical Physics*, vol. 79, no. 3, pp. 1480–1486, 1983.

[32] T. Guillot and A. P. Showman, "Evolution of 51 Pegasus b-like planets," *AA*, vol. 385, no. 1, pp. 156–165, 2002.

[33] A. Burrows, W. B. Hubbard, J. I. Lunine, and J. Liebert, "The theory of brown dwarfs and extrasolar giant planets," *Rev. Mod. Phys.*, vol. 73, pp. 719–765, 2001.

[34] J. M. McMahon, M. A. Morales, C. Pierleoni, and D. M. Ceperley, "The properties of hydrogen and helium under extreme conditions," *Reviews of Modern Physics*, vol. 84, no. 4, pp. 1607–1653, 2012.

[35] W. J. Nellis, M. Ross, A. C. Mitchell, M. Vanthiel, D. A. Young, F. H. Ree, and R. J. Trainor, "Equation of state of molecular-hydrogen and deuterium from shock-wave experiments to 760 kbar," *Physical Review A*, vol. 27, no. 1, pp. 608–611, 1983.

[36] L. B. Da Silva, P. Celliers, G. W. Collins, K. S. Budil, N. C. Holmes, T. W. Barbee Jr, B. A. Hammel, J. D. Kilkenny, R. J. Wallace, M. Ross, R. Cauble, A. Ng, and G. Chiu, "Absolute equation of state measurements on shocked liquid deuterium up to 200 GPa (2 Mbar)," *Physical Review Letters*, vol. 78, no. 3, pp. 483–486, 1997.

[37] L. Collins, J. Kress, I. Kwon, W. Windl, T. Lenosky, N. Troullier, and R. Bauer, "Quantum molecular dynamics simulations of dense matter," *Journal of Computer-Aided Materials Design*, vol. 5, no. 2-3, pp. 173–191, 1998.

[38] G. W. Collins, L. B. Da Silva, P. Celliers, D. M. Gold, M. E. Foord, R. J. Wallace, A. Ng, S. V. Weber, K. S. Budil, and R. Cauble, "Measurements of the equation of state of deuterium at the fluid insulator-metal transition," *Science*, vol. 281, no. 5380, pp. 1178–1181, 1998.

[39] T. Sano, N. Ozaki, T. Sakaiya, K. Shigemori, M. Ikoma, T. Kimura, K. Miyanishi, T. Endo, A. Shiroshita, H. Takahashi, T. Jitsui, Y. Hori, Y. Hironaka, A. Iwamoto, T. Kadono, M. Nakai, T. Okuchi, K. Otani, K. Shimizu, T. Kondo, R. Kodama, and K. Mima, "Laser-shock compression and Hugoniot measurements of liquid hydrogen to 55 GPa," *Physical Review B*, vol. 83, no. 5, p. 054117, 2011.

[40] M. D. Knudson, D. L. Hanson, J. E. Bailey, C. A. Hall, J. R. Asay, and W. W. Anderson, "Equation of state measurements in liquid deuterium to 70 GPa," *Physical Review Letters*, vol. 87, no. 22, p. 225501, 2001.

[41] M. D. Knudson and M. P. Desjarlais, "Shock compression of quartz to 1.6 TPa: Redefining a pressure standard," *Physical Review Letters*, vol. 103, no. 22, p. 225501, 2009.

[42] G. V. Boriskov, A. I. Bykov, R. I. Ilkaev, V. D. Selemir, G. V. Simakov, R. F. Trunin, V. D. Urlin, A. N. Shuikin, and W. J. Nellis, "Shock compression of liquid deuterium up to 109 GPa," *Physical Review B*, vol. 71, no. 9, p. 092104, 2005.

[43] M. Van Thiel and B. J. Alder, "Shock compression of liquid hydrogen," *Molecular Physics*, vol. 10, no. 5, pp. 427–435, 1966.

[44] M. Van Thiel, M. Ross, B. L. Hord, A. C. Mitchell, W. H. Gust, M. J. D'Addario, R. N. Keeler, and K. Boutwell, "Shock-wave compression of liquid deuterium to 0.9 Mbar," *Phys. Rev. Lett.*, vol. 31, pp. 979–982, 1973.

[45] Vankesse.Cg and R. Sigel, "Observation of laser-driven shock-waves in solid hydrogen," *Physical Review Letters*, vol. 33, no. 17, pp. 1020–1023, 1974.

[46] W. J. Nellis, S. T. Weir, and A. C. Mitchell, "Metallization and electrical conductivity of hydrogen in Jupiter," *Science*, vol. 273, no. 5277, pp. 936–938, 1996.

[47] W. J. Nellis, S. T. Weir, and A. C. Mitchell, *Metallization of fluid hydrogen at 140 GPa (1.4 Mbar)*. Strongly Coupled Coulomb Systems, New York: Plenum Press Div Plenum Publishing Corp, 1998.

[48] V. E. Fortov, V. Y. Ternovoi, M. V. Zhernokletov, M. A. Mochalov, A. L. Mikhailov, A. S. Filimonov, A. A. Pyalling, V. B. Mintsev, V. K. Gryaznov, and I. L. Iosilevskii, "Pressure-produced ionization of nonideal plasma in a megabar range of dynamic pressures," *Journal of Experimental and Theoretical Physics*, vol. 97, no. 2, pp. 259–278, 2003.

[49] P. S. Hawke, T. J. Burgess, D. E. Duerre, J. G. Huebel, R. N. Keeler, H. Klapper, and W. C. Wallace, "Observation of electrical-conductivity of isentropically compressed hydrogen at megabar pressures," *Physical Review Letters*, vol. 41, no. 14, pp. 994–997, 1978.

[50] G. V. Boriskov, A. I. Bykov, R. I. Il'Kaev, V. D. Selemir, G. V. Simakov, R. F. Trunin, V. D. Urlin, V. E. Fortov, and A. N. Shuikin, "Shock-wave compression of solid deuterium at a pressure of 120 GPa," *Doklady Physics*, vol. 48, no. 10, pp. 553–555, 2003.

[51] S. K. Grishechkin, S. K. Gruzdev, V. K. Gryaznov, M. V. Zhernokletov, R. I. Il'kaev, I. L. Iosilevskii, G. N. Kashintseva, S. I. Kirshanov, S. F. Manachkin, V. B. Mintsev, A. L. Mikhailov, A. B. Mezhevov, M. A. Mochalov, V. E. Fortov, V. V. Khrustalev, A. N. Shuikin, and A. A. Yukhimchuk, "Experimental measurements of the compressibility, temperature, and light absorption in dense shock-compressed gaseous deuterium," *JETP Letters*, vol. 80, no. 6, pp. 398–404, 2004.

[52] G. I. Kerley, "Equation of state and phase diagram of dense hydrogen," *Physics of the Earth and Planetary Interiors*, vol. 6, pp. 78–82, 1972.

[53] G. I. Kerley, "Equations of state for hydrogen and deuterium." Sandia National Laboratory, Technical Report No. SAND2003-3613, 2003.

[54] M. Ross, "Linear-mixing model for shock-compressed liquid deuterium," *Physical Review B*, vol. 58, no. 2, pp. 669–677, 1998.

[55] H.-k. Mao and R. J. Hemley, "Ultrahigh-pressure transitions in solid hydrogen," *Reviews of Modern Physics*, vol. 66, no. 2, pp. 671–692, 1994.

[56] A. F. Goncharov and R. J. Hemley, "Probing hydrogen-rich molecular systems at high pressures and temperatures," *Chemical Society Reviews*, vol. 35, pp. 899–907, 2006.

[57] N. Subramanian, A. F. Goncharov, V. V. Struzhkin, M. Somayazulu, and R. J. Hemley, "Bonding changes in hot fluid hydrogen at megabar pressures," *Proceedings of the National Academy of Sciences*, vol. 108, no. 15, pp. 6014–6019, 2011.

[58] P. M. Celliers, P. Loubeyre, J. H. Eggert, S. Brygoo, R. S. McWilliams, D. G. Hicks, T. R. Boehly, R. Jeanloz, and G. W. Collins, "Insulator-to-conducting transition in dense fluid helium," *Physical Review Letters*, vol. 104, no. 18, p. 184503, 2010.

[59] L. Stixrude and R. Jeanloz, "Fluid helium at conditions of giant planetary interiors," *Proceedings of the National Academy of Sciences of the United States of America*, vol. 105, no. 32, pp. 11071–11075, 2008.

[60] I. F. Silvera and V. V. Goldman, "The isotropic intermolecular potential for H_2 and D_2 in the solid and gas phases," *The Journal of Chemical Physics*, vol. 69, no. 9, pp. 4209–4213, 1978.

[61] M. Ross, F. H. Ree, and D. A. Young, "The equation of state of molecular hydrogen at very high density," *The Journal of Chemical Physic*, vol. 79, pp. 1487–1494, 1983.

[62] D. Saumon, G. Chabrier, and H. M. Vanhorn, "An equation of state for low-mass stars and giant planets," *Astrophysical Journal Supplement Series*, vol. 99, no. 2, pp. 713–741, 1995.

[63] W. Ebeling and W. Richert, "Thermodynamic properties of liquid hydrogen metal," *Phys. Status Solidi B*, vol. 128, pp. 467–474, 1985.

[64] M. S. Marley and W. B. Hubbard, "Thermodynamics of dense molecular-hydrogen helium mixtures at high-pressure," *Icarus*, vol. 73, no. 3, pp. 536–544, 1988.

[65] D. Saumon and G. Chabrier, "Fluid hydrogen at high-density - the plasma phase-transition," *Physical Review Letters*, vol. 62, no. 20, pp. 2397–2400, 1989.

[66] D. Saumon and G. Chabrier, "Fluid hydrogen at high-density - pressure dissociation," *Physical Review A*, vol. 44, no. 8, pp. 5122–5141, 1991.

[67] D. Saumon and G. Chabrier, "Fluid hydrogen at high-density - pressure ionization," *Physical Review A*, vol. 46, no. 4, pp. 2084–2100, 1992.

[68] H. Kitamura and S. Ichimaru, "Metal-insulator transitions in dense hydrogen: Equations of state, phase diagrams and interpretation of shock-compression experiments," *Journal of the Physical Society of Japan*, vol. 67, no. 3, pp. 950–963, 1998.

[69] D. Beule, W. Ebeling, A. Forster, H. Juranek, R. Redmer, and G. Ropke, "Hydrogen equation of state and plasma phase transition," *Contributions to Plasma Physics*, vol. 39, no. 1-2, pp. 21–24, 1999.

[70] P. P. Edwards, M. T. J. Lodge, F. Hensel, and R. Redmer, "' ... a metal conducts and a non-metal doesn't'," *Philosophical Transactions of the Royal Society a-Mathematical Physical and Engineering Sciences*, vol. 368, no. 1914, pp. 941–965, 2010.

[71] R. Redmer and B. Holst, *Metal-Insulator Transition in Dense Hydrogen*, vol. 132 of *Springer Series in Materials Science*, pp. 63–84. 2010.

[72] G. Chabrier, D. Saumon, and C. Winisdoerffer, "Hydrogen and helium at high density and astrophysical implications," *Astrophysics and Space Science*, vol. 307, no. 1-3, pp. 263–267, 2007.

[73] D. Saumon, *A new tabular EOS for hydrogen isotopes*, vol. 955 of *AIP Conference Proceedings*, pp. 101–104. 2007.

[74] M. Pozzo, C. Davies, D. Gubbins, and D. Alfe, "Thermal and electrical conductivity of iron at Earth's core conditions," *Nature*, vol. 485, no. 7398, pp. 355–358, 2012.

[75] A. Becker, N. Nettelmann, U. Kramm, W. Lorenzen, M. French, and R. Redmer, *Modeling giant planets and brown dwarfs*, vol. 276, pp. 473–474. 2011.

[76] M. Mookherjee, L. Stixrude, and B. Karki, "Hydrous silicate melt at high pressure," *Nature*, vol. 452, no. 7190, pp. 983–986, 2008.

[77] S. Scandolo, "Liquid-liquid phase transition in compressed hydrogen from first-principles simulations," *Proceedings of the National Academy of Sciences*, vol. 100, no. 6, pp. 3051–3053, 2003.

[78] S. A. Bonev, E. Schwegler, T. Ogitsu, and G. Galli, "A quantum fluid of metallic hydrogen suggested by first-principles calculations," *Nature*, vol. 431, no. 7009, pp. 669–672, 2004.

[79] M. A. Morales, C. Pierleoni, E. Schwegler, and D. M. Ceperley, "Evidence for a first-order liquid-liquid transition in high-pressure hydrogen from ab initio simulations," *Proceedings of the National Academy of Sciences of the United States of America*, vol. 107, no. 29, pp. 12799–12803, 2010.

[80] S. Deemyad and I. F. Silvera, "Melting line of hydrogen at high pressures," *Physical Review Letters*, vol. 100, no. 15, p. 155701, 2008.

[81] M. I. Eremets and I. A. Trojan, "Evidence of maximum in the melting curve of hydrogen at megabar pressures," *JETP Letters*, vol. 89, no. 4, pp. 174–179, 2009.

[82] F. Datchi, P. Loubeyre, and R. LeToullec, "Extended and accurate determination of the melting curves of argon, helium, ice (H_2O), and hydrogen (H_2)," *Physical Review B*, vol. 61, no. 10, pp. 6535–6546, 2000.

[83] E. Gregoryanz, A. F. Goncharov, K. Matsuishi, H.-k. Mao, and R. J. Hemley, "Raman spectroscopy of hot dense hydrogen," *Physical Review Letters*, vol. 90, no. 17, p. 175701, 2003.

[84] R. M. Hazen, H. K. Mao, L. W. Finger, and R. J. Hemley, "Single-crystal x-ray diffraction of n-H_2 at high pressure," *Phys. Rev. B*, vol. 36, pp. 3944–3947, 1987.

[85] T. Cui, E. Cheng, B. J. Alder, and K. B. Whaley, "Rotational ordering in solid deuterium and hydrogen: A path integral Monte Carlo study," *Phys. Rev. B*, vol. 55, pp. 12253–12266, 1997.

[86] C. J. Pickard and R. J. Needs, "Structure of phase III of solid hydrogen," *Nature Phys*, vol. 3, no. 7, pp. 473–476, 2007.

[87] C. J. Pickard, M. Martinez-Canales, and R. J. Needs, "Density functional theory study of phase IV of solid hydrogen," *Phys. Rev. B*, vol. 85, p. 214114, 2012.

[88] S. A. Bonev, B. Militzer, and G. Galli, "Ab initio simulations of dense liquid deuterium: Comparison with gas-gun shock-wave experiments," *Physical Review B*, vol. 69, no. 1, p. 014101, 2004.

[89] E. Liberatore, M. A. Morales, D. M. Ceperley, and C. Pierleoni, "Free energy methods in coupled electron ion monte carlo," *Molecular Physics*, vol. 109, no. 23-24, pp. 3029–3036, 2011.

[90] J. Vorberger, I. Tamblyn, S. A. Bonev, and B. Militzer, "Properties of dense fluid hydrogen and helium in giant gas planets," *Contributions to Plasma Physics*, vol. 47, no. 4-5, pp. 375–380, 2007.

[91] J. Vorberger, I. Tamblyn, B. Militzer, and S. A. Bonev, "Hydrogen-helium mixtures in the interiors of giant planets," *Physical Review B*, vol. 75, no. 2, p. 024206, 2007.

[92] L. A. Collins, S. R. Bickham, J. D. Kress, S. Mazevet, T. J. Lenosky, N. J. Troullier, and W. Windl, "Dynamical and optical properties of warm dense hydrogen," *Physical Review B*, vol. 63, no. 18, p. 184110, 2001.

[93] M. P. Desjarlais, J. D. Kress, and L. A. Collins, "Electrical conductivity for warm, dense aluminum plasmas and liquids," *Physical Review E*, vol. 66, no. 2, p. 025401, 2002.

[94] F. Lambert, V. Recoules, A. Decoster, J. Clerouin, and M. Desjarlais, "On the transport coefficients of hydrogen in the inertial confinement fusion regime," *Physics of Plasmas*, vol. 18, no. 5, p. 056306, 2011.

[95] M. A. Morales, J. M. McMahon, C. Pierleoni, and D. M. Ceperley, "Nuclear quantum effects and nonlocal exchange-correlation functionals applied to liquid hydrogen at high pressure," *Physical Review Letters*, vol. 110, no. 6, p. 065702, 2013.

[96] J. P. Perdew and M. Levy, "Physical content of the exact Kohn-Sham orbital energies - band-gaps and derivative discontinuities," *Physical Review Letters*, vol. 51, no. 20, pp. 1884–1887, 1983.

[97] L. J. Sham and M. Schluter, "Density-functional theory of the energy-gap," *Physical Review Letters*, vol. 51, no. 20, pp. 1888–1891, 1983.

[98] H. Chacham and S. G. Louie, "Metallization of solid hydrogen at megabar pressures - a first-principles quasi-particle study," *Physical Review Letters*, vol. 66, no. 1, pp. 64–67, 1991.

[99] M. Stadele and R. M. Martin, "Metallization of molecular hydrogen: Predictions from exact-exchange calculations," *Physical Review Letters*, vol. 84, no. 26, pp. 6070–6073, 2000.

[100] K. A. Johnson and N. W. Ashcroft, "Structure and bandgap closure in dense hydrogen," *Nature*, vol. 403, no. 6770, pp. 632–635, 2000.

[101] R. C. Clay, J. McMinis, J. M. McMahon, C. Pierleoni, D. M. Ceperley, and M. A. Morales, "Benchmarking exchange-correlation functionals for hydrogen at high pressures using quantum Monte Carlo," *Physical Review B*, vol. 89, no. 18, p. 184106, 2014.

[102] J. P. Perdew, K. Burke, and M. Ernzerhof, "Generalized gradient approximation made simple," *Physical Review Letters*, vol. 77, no. 18, pp. 3865–3868, 1996.

[103] J. Heyd, G. E. Scuseria, and M. Ernzerhof, "Hybrid functionals based on a screened Coulomb potential," *The Journal of Chemical Physics*, vol. 118, no. 18, pp. 8207–8215, 2003.

[104] K. Lee, E. D. Murray, L. Z. Kong, B. I. Lundqvist, and D. C. Langreth, "Higher-accuracy van der Waals density functional," *Physical Review B*, vol. 82, no. 8, p. 081101, 2010.

[105] C. Attaccalite and S. Sorella, "Stable liquid hydrogen at high pressure by a novel *ab-initio* molecular-dynamics calculation," *Phys. Rev. Lett.*, vol. 100, p. 114501, 2008.

[106] M. I. Eremets and I. A. Troyan, "Conductive dense hydrogen," *Nature Materials*, vol. 10, no. 12, pp. 927–931, 2011.

[107] J. P. Hansen, G. M. Torrie, and P. Vieillefosse, "Statistical-mechanics of dense ionized matter. 7. Equation of state and phase separation of ionic mixtures in a uniform background," *Physical Review A*, vol. 16, no. 5, pp. 2153–2168, 1977.

[108] E. L. Pollock and B. J. Alder, "Phase separation for a dense fluid mixture of nuclei," *Physical Review A*, vol. 15, no. 3, pp. 1263–1268, 1977.

[109] D. M. Straus, N. W. Ashcroft, and H. Beck, "Phase separation of metallic hydrogen-helium alloys," *Physical Review B*, vol. 15, no. 4, pp. 1914–1928, 1977.

[110] D. J. Stevenson, "Solubility of helium in metallic hydrogen," *Journal of Physics F-Metal Physics*, vol. 9, no. 5, pp. 791–801, 1979.

[111] W. B. Hubbard and H. E. Dewitt, "Statistical-mechanics of light-elements at high-pressure. 7. A perturbative free-energy for arbitrary mixtures of H and He," *Astrophysical Journal*, vol. 290, no. 2, pp. 388–393, 1985.

[112] J. J. Fortney and W. B. Hubbard, "Effects of helium phase separation on the evolution of extrasolar giant planets," *Astrophysical Journal*, vol. 608, no. 2, pp. 1039–1049, 2004.

[113] J. E. Klepeis, K. J. Schafer, T. W. Barbee, and M. Ross, "Hydrogen-helium mixtures at megabar pressures - implications for Jupiter and Saturn," *Science*, vol. 254, no. 5034, pp. 986–989, 1991.

[114] O. Pfaffenzeller, D. Hohl, and P. Ballone, "Miscibility of hydrogen and helium under astrophysical conditions," *Physical Review Letters*, vol. 74, no. 13, pp. 2599–2602, 1995.

[115] M. A. Morales, E. Schwegler, D. Ceperley, C. Pierleoni, S. Hamel, and K. Caspersen, "Phase separation in hydrogen-helium mixtures at Mbar pressures," *Proceedings of the National Academy of Sciences of the United States of America*, vol. 106, no. 5, pp. 1324–1329, 2009.

[116] H. F. Wilson and B. Militzer, "Sequestration of noble gases in giant planet interiors," *Physical Review Letters*, vol. 104, no. 12, p. 121101, 2010.

[117] P. Hohenberg and W. Kohn, "Inhomogeneous electron gas," *Physical Review B*, vol. 136, no. 3B, p. B864, 1964.

[118] W. Kohn and L. J. Sham, "Self-consistent equations including exchange and correlation effects," *Physical Review*, vol. 140, no. 4A, p. 1133, 1965.

[119] D. Prendergast, J. C. Grossman, and G. Galli, "The electronic structure of liquid water within density-functional theory," *Journal of Chemical Physics*, vol. 123, no. 1, p. 014501.

[120] M. Pozzo, M. P. Desjarlais, and D. Alfe, "Electrical and thermal conductivity of liquid sodium from first-principles calculations," *Physical Review B*, vol. 84, no. 5, p. 054203, 2011.

[121] B. B. Karki, J. Zhang, and L. Stixrude, "First principles viscosity and derived models for MgO-SiO_2 melt system at high temperature," *Geophysical Research Letters*, vol. 40, no. 1, pp. 94–99, 2013.

[122] Z. Liu, F. Xu, and D. D. Yan, "New progress in the device physics of polymer-fullerene solar cells," *Acta Chimica Sinica*, vol. 72, no. 2, pp. 171–184, 2014.

[123] P. J. Ren, A. M. Zheng, X. L. Pan, X. W. Han, and X. H. Bao, "DFT Study on the NMR chemical shifts of molecules confined in carbon nanotubes," *Journal of Physical Chemistry C*, vol. 117, no. 44, pp. 23418–23424, 2013.

[124] S. F. Matar, R. Pottgen, and B. Chevalier, "Electronic and magnetic structures and bonding properties of Ce_2T_2X (T = nd element; X = Mg, Cd, Pb or Sn) intermetallics from first principles," *Intermetallics*, vol. 51, pp. 18–23, 2014.

[125] M. Y. Antipin, E. P. Ivakhnenko, Y. V. Koshchienko, P. A. Knyazev, M. S. Korobov, A. V. Chernyshev, K. A. Lyssenko, A. G. Starikov, and V. I. Minkin, "Adducts of cobalt(II) bis(salicylaldiminates) and redox-active phenoxazin-1-one: synthesis, structure, and magnetic properties," *Russian Chemical Bulletin*, vol. 62, no. 8, pp. 1744–1751, 2014.

[126] V. Poltev, V. M. Anisimov, V. I. Danilov, D. Garcia, C. Sanchez, A. Deriabina, E. Gonzalez, F. Rivas, and N. Polteva, "The role of molecular structure of sugar-phosphate backbone and nucleic acid bases in the formation of single-stranded and double-stranded DNA structures," *Biopolymers*, vol. 101, no. 6, pp. 640–650, 2014.

[127] A. Mladek, M. Krepl, D. Svozil, P. Cech, M. Otyepka, P. Banas, M. Zgarbova, P. Jurecka, and J. Sponer, "Benchmark quantum-chemical calculations on a complete set of rotameric families of the DNA sugar-phosphate backbone and their comparison with modern density functional theory," *Physical Chemistry Chemical Physics*, vol. 15, no. 19, pp. 7295–7310, 2013.

[128] A. Sommerfeld, "On the electron theory of metals due to Fermi statistics," *Zeitschrift Fur Physik*, vol. 47, no. 1-2, pp. 1–32, 1928.

[129] A. Sommerfeld, "For the electron theory of metals due to Fermi statistics," *Zeitschrift Fur Physik*, vol. 47, no. 1-2, pp. 43–60, 1928.

[130] E. Fermi, "Un metodo statistico per la determinazione di alcune prioprieta dell'atome," *Rend. Accad Naz. Lincei*, vol. 6, pp. 602–607, 1927.

[131] L. H. Thomas, "The calculation of atomic fields," *Proceedings of the Cambridge Philosophical Society*, vol. 23, pp. 542–548, 1927.

[132] P. A. M. Dirac, "Note on exchange phenomena in the Thomas atom," *Proceedings of the Cambridge Philosophical Society*, vol. 26, pp. 376–385, 1930.

[133] N. Feynman, R. P. Metropolis and E. Teller, "Equations of state of elements based on the generalized Fermi-Thomas theory," *Phys. Rev.*, vol. 75, pp. 1561–1573, 1946.

[134] R. M. Martin, *Electronic Structure: Basic Theory and Practical Methods*. Cambridge University Press, Cambridge, England, 2004.

[135] N. D. Mermin, "Thermal properties of inhomogeneous electron gas," *Physical Review*, vol. 137, no. 5A, p. 1441, 1965.

[136] R. Parr and W. Yang, *Density-Functional Theory of Atoms and Molecules*. Oxford University Press, USA, 1994.

[137] J. Kohanoff, *Electronic Structure Calculations for Solids and Molecules: Theory and Computational Methods*. Cambridge University Press, 2006.

[138] P. Pulay, "Convergence acceleration of iterative sequences - the case of SCF iteration," *Chemical Physics Letters*, vol. 73, no. 2, pp. 393–398, 1980.

[139] J. H. Vanlenthe and P. Pulay, "A space-saving modification of Davidson eigenvector algorithm," *Journal of Computational Chemistry*, vol. 11, no. 10, pp. 1164–1168, 1990.

[140] E. R. Davidson, "Iterative calculation of a few of lowest eigenvalues and corresponding eigenvectors of large real-symmetric matrices," *Journal of Computational Physics*, vol. 17, no. 1, pp. 87–94, 1975.

[141] E. R. Davidson and W. J. Thompson, "Monster matrices: Their eigenvalues and eigenvectors," *Computers in Physics*, vol. 7, no. 5, pp. 519–522, 1993.

[142] A. Booten, H. v. d. Vorst, and W. J. Thompson, "Cracking large-scale eigenvalue problems, part I: algorithms," *Comput. Phys.*, vol. 10, no. 3, pp. 239–242, 1996.

[143] E. R. Davidson, *Methods in Computational Molecular Physics*. Dordrecht, Co., 1983.

[144] M. Born and R. Oppenheimer, "Quantum theory of molecules," *Annalen Der Physik*, vol. 84, no. 20, pp. 0457–0484, 1927.

[145] M. C. Payne, M. P. Teter, D. C. Allan, T. A. Arias, and J. D. Joannopoulos, "Iterative minimization techniques for ab-initio total-energy calculations - molecular-dynamics and conjugate gradients," *Reviews of Modern Physics*, vol. 64, no. 4, pp. 1045–1097, 1992.

[146] D. Marx and J. Hutter, *Ab initio Molecular Dynamics: Basic Theory and Advanced Methods*. Cambridge University Press, Cambridge, England, 2009.

[147] H. Hellmann, *Einfuhrung in die Quantumchemie*. Franz Duetsche, Leipzig, 1937.

[148] R. P. Feynman, "Forces in molecules," *Physical Review*, vol. 56, no. 4, pp. 340–343, 1939.

[149] U. v. Barth and L. Hedin, "A local exchange-correlation potential for the spin polarized case. i," *Journal of Physics C: Solid State Physics*, vol. 5, no. 13, p. 1629, 1972.

[150] D. M. Ceperley and B. J. Alder, "Ground-state of the electron-gas by a stochastic method," *Physical Review Letters*, vol. 45, no. 7, pp. 566–569, 1980.

[151] I. F. Silvera, "The solid molecular hydrogens in the condensed phase - fundamentals and static properties," *Reviews of Modern Physics*, vol. 52, no. 2, pp. 393–452, 1980.

[152] F. Goltl, C. Houriez, M. Guitou, G. Chambaud, and P. Sautet, "Importance of a nonlocal description of electron-electron interactions in modelling the dissociative adsorption of H_2 on Cu(100)," *Journal of Physical Chemistry C*, vol. 118, no. 10, pp. 5374–5382, 2014.

[153] M. Dion, H. Rydberg, E. Schroder, D. C. Langreth, and B. I. Lundqvist, "Van der Waals density functional for general geometries," *Physical Review Letters*, vol. 92, no. 24, p. 246401, 2004.

[154] K. Berland and P. Hyldgaard, "Analysis of van der Waals density functional components: Binding and corrugation of benzene and C_{60} on boron nitride and graphene," *Physical Review B*, vol. 87, no. 20, p. 205421, 2013.

[155] K. Lee, A. K. Kelkkanen, K. Berland, S. Andersson, D. C. Langreth, E. Schrder, B. I. Lundqvist, and P. Hyldgaard, "Evaluation of a density functional with account of van der Waals forces using experimental data of H_2 physisorption on Cu(111)," *Physical Review B*, vol. 84, no. 19, p. 193408, 2011.

[156] K. Lee, K. Berland, M. Yoon, S. Andersson, E. Schroder, P. Hyldgaard, and B. I. Lundqvist, "Benchmarking van der Waals density functionals with experimental data: potential-energy curves for H_2 molecules on Cu(111), (100) and (110) surfaces," *Journal of Physics-Condensed Matter*, vol. 24, no. 42, 2012.

[157] P. Elliott and K. Burke, "Non-empirical derivation of the parameter in the b88 exchange functional," *Canadian Journal of Chemistry*, vol. 87, no. 10, pp. 1485–1491, 2009.

[158] H. Rydberg, M. Dion, N. Jacobson, E. Schrder, P. Hyldgaard, S. I. Simak, D. C. Langreth, and B. I. Lundqvist, "Van der Waals density functional for layered structures," *Physical Review Letters*, vol. 91, no. 12, p. 126402, 2003.

[159] Y. Zhang and W. Yang, "Comment on generalized gradient approximation made simple," *Physical Review Letters*, vol. 80, no. 4, pp. 890–890, 1998.

[160] J. P. Perdew and W. Yue, "Accurate and simple density functional for the electronic exchange energy: Generalized gradient approximation," *Physical Review B*, vol. 33, no. 12, pp. 8800–8802, 1986.

[161] E. D. Murray, K. Lee, and D. C. Langreth, "Investigation of exchange energy density functional accuracy for interacting molecules," *Journal of Chemical Theory and Computation*, vol. 5, no. 10, pp. 2754–2762, 2009.

[162] F. Bloch, *Uber die Quantenmechanik der Elektronen in Kristallgittern*. Berlin: Springer, 1928.

[163] V. Heine, *The Pseudopotential Concept*, vol. Volume 24, pp. 1–36. Academic Press, 1970.

[164] P. E. Blochl, "Projector augmented-wave method," *Physical Review B*, vol. 50, no. 24, pp. 17953–17979, 1994.

[165] G. Kresse and D. Joubert, "From ultrasoft pseudopotentials to the projector augmented-wave method," *Physical Review B*, vol. 59, no. 3, pp. 1758–1775, 1999.

[166] N. A. W. Holzwarth, G. E. Matthews, R. B. Dunning, A. R. Tackett, and Y. Zeng, "Comparison of the projector augmented-wave, pseudopotential, and linearized augmented-plane-wave formalisms for density-functional calculations of solids," *Physical Review B*, vol. 55, no. 4, pp. 2005–2017, 1997.

[167] L. Verlet, "Computer "experiments" on classical fluids. I. thermodynamical properties of Lennard-Jones molecules," *Physical Review*, vol. 159, no. 1, pp. 98–103, 1967.

[168] P. Pulay, "Ab initio calculation of force constants and equilibrium geometries in polyatomic molecules .i. theory," *Molecular Physics*, vol. 17, no. 2, pp. 197–, 1969.

[169] S. Nosé, "A unified formulation of the constant temperature molecular-dynamics methods," *Journal of Chemical Physics*, vol. 81, no. 1, pp. 511–519, 1984.

[170] W. G. Hoover, "Canonical dynamics - equilibrium phase-space distributions," *Physical Review A*, vol. 31, no. 3, pp. 1695–1697, 1985.

[171] E. Hernandez, "Metric-tensor flexible-cell algorithm for isothermal-isobaric molecular dynamics simulations," *Journal of Chemical Physics*, vol. 115, no. 22, pp. 10282–10290, 2001.

[172] I. Souza and J. L. Martins, "Metric tensor as the dynamical variable for variable-cell-shape molecular dynamics," *Physical Review B*, vol. 55, no. 14, pp. 8733–8742, 1997.

[173] S. D. Bond, B. J. Leimkuhler, and B. B. Laird, "The Nosé-Poincare method for constant temperature molecular dynamics," *Journal of Computational Physics*, vol. 151, no. 1, pp. 114–134, 1999.

[174] H. J. Monkhorst and J. D. Pack, "Special points for Brillouin-zone integrations," *Physical Review B*, vol. 13, no. 12, pp. 5188–5192, 1976.

[175] H. G. P. H. Flyvbjery, "Error estimates on averages of correlated data," *J. Chem. Phys*, vol. 91, no. 1, pp. 461–1989, 1989.

[176] P. Allen and D. Tildesley, *Computer simulation of liquids*. Clarendon Press, 1987.

[177] D. McQuarrie, *Statistical Mechanics*. University Science Books, 2000.

[178] R. Kubo, "Statistical-mechanical theory of irreversible processes .1. General theory and simple applications to magnetic and conduction problems," *Journal of the physical society of Japan*, vol. 12, no. 6, pp. 570–586, 1957.

[179] D. A. Greenwood, "The Boltzmann equation in the theory of electrical conduction in metals," *Proceedings of the Physical Society of London*, vol. 71, no. 460, pp. 585–596, 1958.

[180] G. V. Chester and A. Thellung, "Law of Wiedemann and Franz," *Proceedings of the Physical Society of London*, vol. 77, no. 497, pp. 1005–1013, 1961.

[181] S. Mazevet, M. Torrent, V. Recoules, and F. Jollet, "Calculations of the transport properties within the PAW formalism," *High Energy Density Physics*, vol. 6, no. 1, pp. 84–88, 2010.

[182] R. Franz and G. Wiedemann, "Ueber die wrme-leitungsfhigkeit der metalle," *Annalen der Physik*, vol. 165, no. 8, pp. 497–531, 1853.

[183] N. Ashcroft and N. Mermin, *Solid State Physics*. Philadelphia: Saunders College, 1976.

[184] J. M. Ziman, "A theory of the electrical properties of liquid metals - the monovalent metals," *Philosophical Magazine*, vol. 6, no. 68, pp. 1013–1034, 1961.

[185] N. K. Mott, *Metal-Insulator Transitions*. Taylor & Francis, New York, 1990.

[186] N. Mott and E. Davis, *Electronic Processes in Non-Crystalline Materials*. Oxford University, Oxford, 1979.

[187] G. D. Dickenson, M. L. Niu, E. J. Salumbides, J. Komasa, K. S. E. Eikema, K. Pachucki, and W. Ubachs, "Fundamental vibration of molecular hydrogen," *Physical Review Letters*, vol. 110, no. 19, p. 193601, 2013.

[188] W. J. M. Rankine, "On the thermodynamic theory of waves of finite longitudinal disturbance," *Philosophical Transactions of the Royal Society of London*, vol. 160, pp. 277–288, 1870.

[189] P. H. Hugoniot, *Mémoire sur la propagation du movement dans les corps et plus spécialement dans les gaz parfaits, 1e Partie.*, vol. 57. J. Ecole Polytech. (Paris), 1887.

[190] P. H. Hugoniot, *Mémoire sur la propagation du movement dans les corps et plus spécialement dans les gaz parfaits, 2e Partie.*, vol. 58. J. Ecole Polytech. (Paris), 1889.

[191] J. N. C. R. Johnson, "Classic papers in shock compression science," 1998.

[192] G. Kresse and J. Hafner, "Ab-initio molecular-dynamics for liquid-metals," *Physical Review B*, vol. 47, no. 1, pp. 558–561, 1993.

[193] T. Thonhauser, V. R. Cooper, S. Li, A. Puzder, P. Hyldgaard, and D. C. Langreth, "Van der Waals density functional: Self-consistent potential and the nature of the van der Waals bond," *Physical Review B*, vol. 76, no. 12, p. 125112, 2007.

[194] J. Klimes, D. R. Bowler, and A. Michaelides, "Van der Waals density functionals applied to solids," *Physical Review B*, vol. 83, no. 19, p. 195131, 2011.

[195] J. P. Perdew and Y. Wang, "Accurate and simple analytic representation of the electron-gas correlation-energy," *Physical Review B*, vol. 45, no. 23, pp. 13244–13249, 1992.

[196] W. B. Hubbard, A. Burrows, and J. I. Lunine, "Theory of giant planets," *Annual Review of Astronomy and Astrophysics*, vol. 40, pp. 103–136, 2002.

[197] G. Kresse and J. Furthmuller, "Efficient iterative schemes for ab initio total-energy calculations using a plane-wave basis set," *Physical Review B*, vol. 54, no. 16, pp. 11169–11186, 1996.

[198] H. Juranek and R. Redmer, "Self-consistent fluid variational theory for pressure dissociation in dense hydrogen," *Journal of Chemical Physics*, vol. 112, no. 8, pp. 3780–3786, 2000.

[199] B. Holst, R. Redmer, and M. P. Desjarlais, "Thermophysical properties of warm dense hydrogen using quantum molecular dynamics simulations," *Physical Review B*, vol. 77, no. 18, p. 184201, 2008.

[200] L. Caillabet, S. Mazevet, and P. Loubeyre, "Multiphase equation of state of hydrogen from ab initio calculations in the range 0.2 to 5 g/cc up to 10 eV," *Physical Review B*, vol. 83, no. 9, p. 094101, 2011.

[201] M. P. Desjarlais, "Density-functional calculations of the liquid deuterium Hugoniot, reshock, and reverberation timing," *Physical Review B*, vol. 68, no. 6, p. 064204, 2003.

[202] B. Militzer and D. M. Ceperley, "Path integral Monte Carlo calculation of the deuterium Hugoniot," *Physical Review Letters*, vol. 85, no. 9, pp. 1890–1893, 2000.

[203] J. E. Bailey, M. D. Knudson, A. L. Carlson, G. S. Dunham, M. P. Desjarlais, D. L. Hanson, and J. R. Asay, "Time-resolved optical spectroscopy measurements of shocked liquid deuterium," *Physical Review B*, vol. 78, no. 14, p. 144107, 2008.

[204] I. Tamblyn and S. A. Bonev, "Structure and phase boundaries of compressed liquid hydrogen," *Physical Review Letters*, vol. 104, no. 6, p. 065702, 2010.

[205] M. French, A. Becker, W. Lorenzen, N. Nettelmann, M. Bethkenhagen, J. Wicht, and R. Redmer, "Ab initio simulations for material properties along the Jupiter adiabat," *Astrophysical Journal Supplement Series*, vol. 202, no. 1, 2012.

[206] N. Nettelmann, A. Becker, B. Holst, and R. Redmer, "Jupiter models with improved ab initio hydrogen equation of state (H-REOS.2)," *Astrophysical Journal*, vol. 750, no. 1, 2012.

[207] G. Mazzola, S. Yunoki, and S. Sorella, "Unexpectedly high pressure for molecular dissociation in liquid hydrogen by electronic simulation," *Nature Communications*, vol. 5, 2014.

[208] V. V. Brazhkin, Y. D. Fomin, A. G. Lyapin, V. N. Ryzhov, and E. N. Tsiok, "Widom line for the liquid-gas transition in Lennard-Jones system," *Journal of Physical Chemistry B*, vol. 115, no. 48, pp. 14112–14115, 2011.

[209] D. J. Stevenson and E. E. Salpeter, *in Jupiter*. University of Arizona Press, 1976.

[210] W. Lorenzen, B. Holst, and R. Redmer, "Metallization in hydrogen-helium mixtures," *Physical Review B*, vol. 84, no. 23, p. 235109, 2011.

[211] E. Kaxiras, J. Broughton, and R. J. Hemley, "Onset of metallization and related transitions in solid hydrogen," *Physical Review Letters*, vol. 67, no. 9, pp. 1138–1141, 1991.

[212] S. Korkmaz and S. D. Korkmaz, "Structure and electrical resistivities of liquid Al and Ga metals and their binary alloys," *International Journal of Thermophysics*, vol. 33, no. 5, pp. 831–842, 2012.

[213] S. D. Korkmaz and S. Korkmaz, "Electronic transport properties of liquid $Na_{1-x}K_x$ alloys," *Journal of Molecular Liquids*, vol. 186, pp. 85–89, 2013.

[214] S. D. Korkmaz and S. Korkmaz, "Structure and electrical resistivity of liquid In-Sn alloy," *Computational Materials Science*, vol. 48, no. 3, pp. 466–470, 2010.

[215] D. E. Hanson, L. A. Collins, J. D. Kress, and M. P. Desjarlais, "Calculations of the thermal conductivity of National Ignition Facility target materials at temperatures near 10 eV and densities near 10 g/cc using finite-temperature quantum molecular dynamics," *Physics of Plasmas*, vol. 18, no. 8, p. 082704, 2011.

[216] P. B. Thakor, J. J. Patel, Y. A. Sonvane, and A. R. Jani, "Electrical resistivity of Al-Cu liquid binary alloy," *Proceeding of International Conference on Recent Trends in Applied Physics and Material Science, RAM 2013*, vol. 1536, pp. 591–592, 2013.

[217] N. F. Mott, "Is there ever a minimum metallic conductivity," *Solid-State Electronics*, vol. 28, no. 1-2, pp. 57–59, 1985.

[218] P. M. Celliers, G. W. Collins, L. B. Da Silva, D. M. Gold, R. Cauble, R. J. Wallace, M. E. Foord, and B. A. Hammel, "Shock-induced transformation of liquid deuterium into a metallic fluid," *Physical Review Letters*, vol. 84, no. 24, pp. 5564–5567, 2000.

[219] R. Redmer, H. Juranek, N. Nettelmann, and B. Holst, *Warm dense hydrogen in the chemical picture*, vol. 845 of *AIP Conference Proceedings*, pp. 127–130. 2006.

[220] N. F. Mott, "Conduction in non-crystalline systems. 9. Minimum metallic conductivity," *Philosophical Magazine*, vol. 26, no. 4, p. 1015, 1972.

[221] T. Guillot, *The interiors of giant planets: Models and outstanding questions*, vol. 33 of *Annual Review of Earth and Planetary Sciences*, pp. 493–530. 2005.

[222] W. K. M. Rice and P. J. Armitage, "On the formation timescale and core masses of gas giant planets," *Astrophysical Journal*, vol. 598, no. 1, pp. L55–L58, 2003.

[223] E. E. Mamajek, *Initial Conditions of Planet Formation: Lifetimes of Primordial Disks*, vol. 1158 of *AIP Conference Proceedings*, pp. 3–10. 2009.

[224] N. M. Batalha, "Exploring exoplanet populations with NASA's Kepler mission," *Proceedings of the National Academy of Sciences of the United States of America*, vol. 111, no. 35, pp. 12647–12654, 2014.

[225] W. Lorenzen, B. Holst, and R. Redmer, "Demixing of hydrogen and helium at megabar pressures," *Physical Review Letters*, vol. 102, no. 11, p. 115701, 2009.

[226] G. F. Lindal, G. E. Wood, G. S. Levy, J. D. Anderson, D. N. Sweetnam, H. B. Hotz, B. J. Buckles, D. P. Holmes, P. E. Doms, V. R. Eshleman, G. L. Tyler, and T. A. Croft, "The atmosphere of Jupiter - an analysis of the Voyager radio occultation measurements," *Journal of Geophysical Research-Space Physics*, vol. 86, no. NA10, pp. 8721–8727, 1981.

[227] G. F. Lindal, D. N. Sweetnam, and V. R. Eshleman, "The atmosphere of Saturn - an analysis of the Voyager radio occultation measurements," *Astronomical Journal*, vol. 90, no. 6, pp. 1136–1146, 1985.

[228] J. J. Fortney and W. B. Hubbard, "Phase separation in giant planets: Inhomogeneous evolution of Saturn," *Icarus*, vol. 164, no. 1, pp. 228–243, 2003.

[229] A. Becker, N. Nettelmann, B. Holst, and R. Redmer, "Isentropic compression of hydrogen: Probing conditions deep in planetary interiors," *Physical Review B*, vol. 88, no. 4, p. 045122, 2013.

[230] F. Gonzalez-Cataldo, H. F. Wilson, and B. Militzer, "Ab initio free energy calculations of the solubility of silica in metallic hydrogen and application to giant planet cores," *Astrophysical Journal*, vol. 787, no. 1, p. 79, 2014.